Pattern formation at semiconductor interfaces and surfaces

vorgelegt von
Dipl.-Phys. Sumit Bose
aus Berlin

Dem Fachberich 4 - Physik
der Technischen Universität Berlin
zur Verleihung des akademischen Grades
Doktor der Naturwissenschaften
genehmigte Dissertation

Promotionsausschuss:
Vorsitzender: Prof. Dr. J. Willer
Berichter: Prof. Dr. E. Schöll, PhD
Berichter: Prof. Dr. W. Richter

Tag der wissenschaftlichen Aussprache:
19.12.2000

Berlin 2001
D 83

Abstract

In this work the pattern forming processes in three different semiconductor systems will be discussed. The first example is the current transport through a semiconductor heterostructure showing an s-shaped current voltage characteristic. The charge transport through the device is modelled by a hydrodynamic approach and the resulting partial differential equations fall into the class of reaction-diffusion systems. Depending on the structure of the contacts the equations may be globally or diffusively coupled. In the globally coupled equations three different types of stationary and a number of oscillating, spatially inhomogenous patterns can be found. In contrast to that the diffusively coupled equations only show three different types of stationary, spatially inhomogenous patterns and in a small regime of parameter space bistability between homogeneous oscillations and stationary stuctures.

The second example is the initial stage of growth of self-organised quantum dots which can be observed in hetero-epitaxy of materials with different lattice constants. The strain which is present in this type of systems plays an important role in the formation of quantum dots. To model the initial stage of growth strain effects are included into a standard kinetic Monte Carlo scheme leading to a suppression of Ostwald ripening and to a cooperative growth mode. This growth mode is necessary for a sharp size distribution of quantum dots. It will be shown under what conditions not only good ordering in size but also regular spatial arangement of the quntum dots can be acchieved. The influence of growth temperature, growth rate, coverage and growth interruption on the surface structure and the quality of the quantum dots will be discussed.

The third example is the atomic surface structure of InP(001)-(2×4). For different proposed structural models of the surface the reflectance anisotropy spectrum is calculated. The necessary electronic eigenvalues and eigenstates are calculated within a tight-binding scheme. By comparison to experimental data and other theoretical approaches it will be possible to find out about the atomic surface structure of InP(001)-(2×4) one can see in experiments. It will also be discussed which optical transitions are responsible for the structures which can be found in experimental reflectance anisotropy spectra of InP(001)-(2×4).

Finally the patterns found in charge tranport and during the formation of quantum dots will be compared. The influence of the underlying atomic structure, e.g., the results of the third example, on pattern forming processes in the first two examples will be discussed.

I would like to thank

- Prof. E. Schöll for the possibility to work on the exciting field of pattern formation in semiconductors and for numerous advices and disscussions by which he guided this work,
- Prof. W. Richter for making the second report and for giving me the possibility to work two months in Rome,
- my international friends and co-workers Pavel Rodin, Scott Zoldi and Anne DeWit for fruitful cooperation,
- Prof. Rodolfo Del Sole, Anatoli Shkrebtii, Giovani Onida and Olivia Pulci for all their support and hospitality in Rome,
- Thomas Trepk, Patrick Vogt, Martin Zorn, and all the other people from W. Richter's group for the never-ending supply of tea and conversations,
- Thomas Zettler for asking me if I would like to work with Rodolfo Del Sole,
- Norbert Esser for proofreading parts of this work,
- Matthias Meixner for proofreading this works and for being such a good friend,
- Andreas Amann, Nilüfer Baba, Jochen Damzog, Rainer Döttling, Giorgio Franceschini, Bernhard Kehrer, Gerold Kießlich, Roland Kunert, Kazuaki Kunihiro, Ralph E. Kunz, Detlef Merbach, Holger Naundorf, Frank Prengel, Axel Reimann, Georg Schwarz, Andreas Wacker, Reinhard Wetzler and all other members of E. Schöll's group for nice and inspiring working atmosphere,
- my wife Miriam.

Contents

I: Introduction

The study of self-organised patterns and the process of pattern formation is often connected to special chemical or physical systems like, e.g., the Belousov-Zhabotinsky [1] or the Rayleigh-Benard convection [2]. For these systems model equations were developed which can describe the behaviour of the system for a wide range of parameters. Often these equations are dimensionless, i.e. the dependencies on material constants are eliminated by scaling the involved quantities. Typical examples for this type of models are the Brusselator [3] and Oregonator [4] for the Belousov-Zhabotinsky reaction and the Swift-Hohenberg equation [5] for the Rayleigh-Benard convection. The equations were even generalised further with the help of amplitude-equations [6] which describe the system near a bifurcation point [7]. The idea behind this generalization is to find a common description for pattern formation processes in different systems [8] and there is a large number of systems from very different fields of science which show pattern formation.

A very striking ”real world” example are the patterns on animal fur, sea-shells or butterfly wings [9]. Each species has its own, distinct pattern. Zebras for example have stripes while leopards have spots and giraffes have a net like pattern. But also each individual animal has its own pattern, the stripes of a zebra are like fingerprints they look similar on different animals but they are not completely equal. Although the patterns are very different a suggestion was made in [10] that a single mechanism is responsible for them which again demonstrate the advantage of a general description of the studied system. Pattern formation can also be observed in other fields of biology like epidemic models [9], evolution and the differentiation of the zygote [11] and the spread of the trigger impulse of the heartbeat over the surface of the heart [12, 13]. The last example is also an example for the connection of temporal processes [14] with spatial patterns.

The label ”self-organised’ is generally used for systems far from the thermodynamic equilibrium. This implies that these systems have to be open and driven and they are often called *dissipative* systems. But also closed systems, which will return to a thermodynamic equilibrium state after a perturbation, can show interesting and complex patterns.

In this work we concentrate on self-organised pattern formation in semiconductor

systems but also examples of systems near equilibrium or evolving to equilibrium will be discussed. We consider two different examples which are distinguished by the different physical nature of the system and different methods applied to model them, but which are similar in that both exhibit self-organised pattern formation in two spatial dimensions. The third example is a system in thermodynamic equilibrium which is tightly connected to the pattern formation processes in the other two examples, as will be explained later.

One of our examples is the non-linear charge transport in semiconductor devices, namely heterostructure diodes. For an overview of non-linear effects in charge transport in semiconductor see, e.g., [15, 16, 17]. A typical phenomenon of non-linear charge transport are the so called "current filaments" which are areas of high current density surrounded by a field of low current density. Besides the general dynamics of the current filaments which may lead to interesting new applications and devices the examination of the current filaments might help to improve existing devices, because they are often unwanted. In the studied devices a specific current can flow through the device either in a homogeneous fashion, i.e. the current density is constant over the cross-section of the device, or in a filamentary way. But if one or more current filaments cover only a fraction of the cross-section of the device the current density in the filaments has to be much higher than in the homogeneous case. This will often lead to stronger heating of the device and a reduced life-time. Therefore it is often desired to operate the devices in the homogeneous mode, which on the other hand might not always be possible because, e.g., only certain voltage levels might be allowed in the circuit. Now it is useful to know more about the filaments, e.g., if they stay at a fixed position or if they will move under certain conditions (rocking and travelling filaments [18, 19, 20]), which may lead to a homogeneous transport in the time average. Some of the results and the underlying model are also applicable to other systems like large scale, high power devices like thyristors [21, 22]. The charge transport in the semiconductor device will be modelled by a hydrodynamic approach. As a result the system will be described by a set of coupled partial differential equation with a quite simple structure. This method has three major advantages. First the model is valid for a whole class of devices. Although not every detail of a specific device is covered the general transport properties are included. Second the simple structure of the partial differential equations makes an intensive numerical investigation with standard techniques possible. And third, the model equations can be compared with model equations of other spatially extended dynamical systems on an analytic level.

Our second example is the pattern formation during epitaxial semiconductor growth [23, 24, 25]. Here we will concentrate on the so called Stranski-Krastanov [26] growth-mode and study the formation of small islands called quantum-dots. When growing a material on a substrate with a different lattice constant epitaxially, i.e. without any vacancies or defects, these dislocation-free quantum-dots can emerge spontaneously under specific growth conditions. This would not be of much interest, were there not some special properties which are quite unique. It is possible to grow these quantum-

dots with a sharp size distribution, i.e. they have nearly the same size, and with a common shape. It is also possible to find them in regular arrangements on the surface, often in long rows or even in regular arrays. For these reasons they are often called self-assembled or self-organised quantum-dots. An example of nicely ordered quantum-dots is shown in figure I.1.

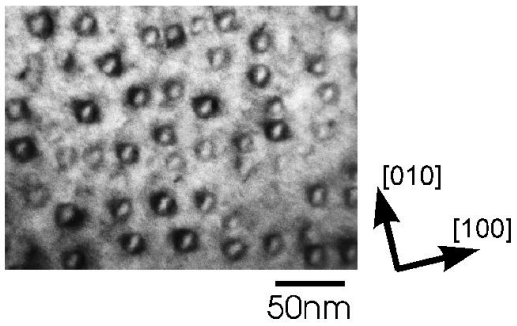

Figure I.1: Plan-view TEM (transmission electron microscopy) image of an ensemble of InAs quantum-dots grown on GaAs(100). Taken from [27] with kind permission of the authors.

This may lead to a number of applications in new semiconductor devices. First of all and already realized are quantum-dot semiconductor lasers. Due to the different electronic properties, namely the different band gap, of the two involved materials, quantum-dots can trap electrons or holes. With a typical size of about $10nm$ they have only a very small number of bound states. The variation of the energies of corresponding bound states in different quantum-dots is small because of the sharp size distribution. The number of quantum-dots can be increased by growing more than one layer of quantum-dots. Interesting new phenomena can be found here, too. For examples the so-called stacked quantum-dots [28], i.e. a quantum-dot in a higher layer will grow precisely above a quantum-dot in the layer below. The second field of applications is connected to charge transport and micro-electronic devices. The structural sizes of conventional field-effect transistors (FET) produced by CMOS (complementary metal-oxide-semiconductor) processes become smaller every year following Moore's Law[1]. At the time being the most modern processors in mass-production have a structure size of about 180 nm. In about 10 years time the structural size will be below $50nm$ where quantum effects will start to dominate the behaviour of micro-(nano)-electrical devices. Then new devices which use the quantum effects will replace the old field-effect transistors. Self-assembled quantum-dots used as single electron transistors [29, 30] wired by self-assembled nano-tubes [31, 32] may be one of these new devices.

The spontaneous formation of ordered small islands cannot be observed in different kinds of semiconductor materials alone, see, e.g., [33, 34]. Also in metallic materials, e.g., when growing silver (Ag) on platinum (Pt) [35] a similar behaviour was found. In addition to the self-assembled production quantum-dots can be created by etching techniques or on pre-patterned surfaces. The advantage of etched quantum-dots for

[1]Named after Gordon Moore founder of the Intel Corporation; says that every three years the DRAM (dynamic random access memory) storage capacity is quadrupled

example is the much higher control of the spatial arrangement, but the fabrication is much more complicated. Another interesting quantum-dot system is presented in [36] where gold (Au) clusters with a charged acid coating are arranged on a charged polymer surface.

In this work we will focus on the initial stage of growth of self-assembled quantum-dots. During this stage the fundaments for most properties of the final system are set. Especially the fundaments of the quantum-dots, i.e. the first layer of material, are created. The sizes and the positions of these fundaments determine the size-distribution and the spatial arrangement of the final quantum-dots ensemble. To study the important processes during this stage and the influence of external parameters like temperature and growth rate we use a kinetic Monte-Carlo simulation. We add an energy term to the standard kinetic Monte-Carlo model to include the effects of strain which is present in the Stranski-Krastanov growth mode. The strain will be modelled by a simple phenomenological approach. To work out the basic effects which are present in all the different material systems we restrict the rest of the Monte-Carlo approach to a very basic system. We use a solid-on-solid approach with one type of atoms, next neighbour hopping and no desorption.

As we have said earlier our third example is tightly connected to the other two examples, in some sense it is the basis of the other examples, namely we will have a closer look at the structure and the properties of the underlying atomic lattice. This should be done by trying to answer the question of how the surface of Indium-Phosphide (InP) in the [001] direction with a 2×4 reconstruction looks like. To do this we will compare experimental reflectance anisotropy spectroscopy data with calculated spectra for different proposed structures. Although this is a very specific material system it is possible to see how important a deep knowledge of the precise atomic structure is for realistic calculations. And even if the previous two examples try to be quite material independent there are certain properties which are tightly connected to the specific atomic structure of a material system. For example the question if the diffusion of ad-atoms on a specific semiconductor surface is isotropic or not can only be answered if the structure of the surface reconstruction is known [37, 38]. Or the answer to the question if an interface between two different semiconductor materials can be assumed as perfectly flat or if there is a high probability for defects and impurities and how large they are needs detailed studies of the atomic structure at the interface.

Now we have three different examples of pattern formation in semiconductor systems. In the following the differences, but also the common properties of the systems with respect to pattern formation will be discussed. We will see that in the first example pattern formation far from thermodynamic equilibrium can be found, while the third example is near equilibrium. The second example is a mixture of both, it will start far from equilibrium but after some time it can evolve to the thermodynamic equilibrium.

This thesis is organised as follows. In chapter II, III and IV the current-density patterns at a semiconductor interface, the self-organised growth of quantum-dots and the

surface structure of InP[001] will be discussed on their own, respectively. Finally a general conclusion and a discussion of the similarities and dissimilarities of the three examples will be given in chapter V.

II: Pattern Formation at Interfaces

In this chapter we want to study pattern formation at semiconductor interfaces with the help of reaction-diffusion equations. Our topic are current filaments, i.e. channels of higher current density [15]. Although the dynamics of the charge carriers is determined by Maxwell's equations coupled with appropriate transport equations we use simpler equations to describe the dynamics at an interface. Firstly because it is easier to obtain some analytical results. And secondly to study generic equations which are independent of special material properties, and are representative of a larger class of different systems. And finally it has to be noted much larger computer power is necessary to integrate Maxwell's equations. However, there are new and fast algorithms which can handle the formation of a single current filament in a semiconductor film in a reasonable amount of time [39] and it is most likely that in the near future also structures with interfaces will be in the range.

We use the following two sets of reaction-diffusion equations which were derived and employed in former studies in one spatial dimension [40, 41, 42, 43, 44, 45, 46]. Here we want to present studies on two dimensional spatial domains.

$$\begin{aligned} \dot{u}(t) &= \alpha(j_0 - (u - \langle a(x,y,t)\rangle)) \\ \dot{a}(x,y,t) &= \frac{u-a}{(u-a)^2+1} - Ta + \Delta a \end{aligned} \tag{II.1}$$

$$\begin{aligned} \dot{u}(x,y,t) &= \alpha(j_0 - (u-a) + D\Delta u) \\ \dot{a}(x,y,t) &= \frac{u-a}{(u-a)^2+1} - Ta + \Delta a \end{aligned} \tag{II.2}$$

u is the normalised voltage across the interface and a stands for an internal variable, like charge density or electron temperature [47] at the interface. α is the ratio of the time-scales of u and a and D the ratio of their diffusions constants. The spatial average is denoted by $\langle\cdot\rangle$ and Δ is the two-dimensional Laplacian $\partial^2/\partial x^2 + \partial^2/\partial y^2$. T is an internal parameter which controls the bistable regime, and j_0 is the external current density which is the bifurcation parameter. The spatial variables x and y denote the two

coordinates perpendicular to the current flow. The spatial dependence in the direction of the current flow, the z-coordinate, has been eliminated from the transport equations [48].

We will apply Neumann boundary conditions which are often also called zero-flux boundaries, since they correspond to vanishing transverse current densities.

$$\frac{\partial u}{\partial x}|_{0,L} = \frac{\partial u}{\partial y}|_{0,L} = \frac{\partial a}{\partial x}|_{0,L} = \frac{\partial a}{\partial y}|_{0,L} = 0, \tag{II.3}$$

where L is the size of the system. In (II.1) the system size appears also in the spatial average, but in (II.2) the system size only enters the boundary conditions. It is possible to scale the equations in a way that they are always defined on the same domain [49], e.g. $[0,1] \times [0,1]$, and that the size of the system is a parameter in the equation, but since earlier studies used the above type of scaling we will keep it here.

We do not impose a strong physical meaning on the dynamic variable a, since we think the two sets of equations (II.1) and (II.2) can describe qualitatively a whole range of semiconductor systems, i.e. devices, with an S-shaped current-voltage characteristic. (II.1) was originally derived for a Heterostructure Hot Electron Diode [50, 40] where it compares quite well with experiments [51], but it can also explain the behaviour found in $pnpn$-Diodes [52]. (II.2) is in some sense an extension of (II.1) for samples with linear contact regions [53] and spatio-temporal patterns which can be found in (II.2) compare quite well to structures found in pin-Diodes [54].

The homogeneous solution for these equations form an S-shaped current- voltage characteristic which can be seen in figure II.1.

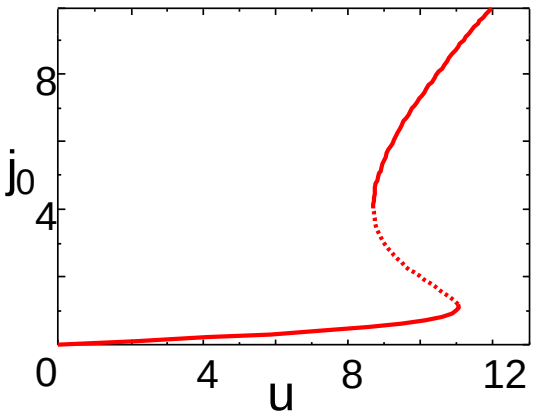

Figure II.1: A typical S-shaped current-voltage characteristic for the homogeneous steady states. ($T = 0.05$)

This S-shaped characteristic is common to all the experiments mentioned above and the model equations (II.1) and (II.2). Hence we believe that the two sets of equations can describe the current transport behaviour of a large number of semiconductor systems showing an S-shaped current-voltage characteristic.

II.1 The Model

In this section we briefly discuss the physical phenomena which are reflected in the systems (II.1) and (II.2). For a detailed introduction to the physics of semiconductors and semiconductor heterostructures see, e.g., [55, 56]. For a specific discussion of the systems see [40]. The physical system we want to study is the charge transport through a semiconductor interface between two contacts. We are interested in the case where the interface is an obstacle to the current transport. The obstacle should have a nonlinear character, i. e., the current beyond the interface should depend on the incoming current in a nonlinear way. Here we consider a potential barrier in a semiconductor heterostructure. The potential barrier is a result of the different band gaps of the different materials forming the interface. According to the Shockley-Anderson model [57] the Fermi energy has to be constant at the junction and consequently there is a jump in the conduction band [1] which prevents charge carriers from getting through the interface. This is illustrated in the following figure II.2a).

If a voltage drop is applied to the interface the conduction band is bent as shown in figure II.2b). Now the barrier has a finite width and also a finite height and a particle in front of the barrier has a certain probability for tunnelling through the barrier. For more than one particle approaching the barrier we can introduce a tunnelling rate T_a. If the voltage drop before the interface is higher than the barrier height the charge carriers can gain enough energy to pass over the barrier. Even now not all particles will pass the barrier, because due to scattering and other effects only a fraction f will have enough energy. Here we assume a special function

$$f = \frac{1}{1 + \epsilon^2(u)} \tag{II.4}$$

where ϵ is the ration between the height of the potential barrier and the maximum energy gain caused by the voltage drop in front of the barrier which is a function of the total applied voltage u. The charge carriers which pass the interface will have quite a high energy and the resulting current in the second layer is called thermionic current.

Now we have two different transport mechanisms through the interface [58]. One primarily for low currents, the tunnelling current, and an other one for high currents, the thermionic current. For simplicity we neglect any functional dependencies of the tunnelling rate T, especially we neglect the dependence of T on the applied voltage, and only assume the thermionic current to be a function of the applied voltage. To close the system we have to model the voltage drop over the interface.

If the interface is embedded between two perfect metallic contacts any inhomogeneity of charge carriers in the contacts will decay immediately, i.e. much faster than the carriers at the interface. The charge carriers which accumulate at the interface are much slower because of the larger dielectric relaxation time at semiconductor interfaces and

[1] and also in the valence band, but here we want to discuss only the transport of electrons

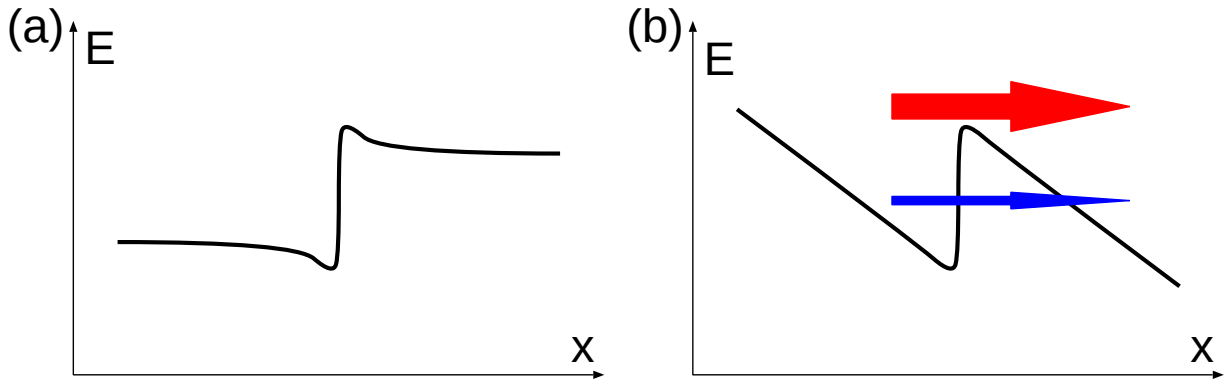

Figure II.2: Conduction band at the interface with (b) and without (a) applied voltage. The blue arrow symbolises the small tunnelling current, while the red arrow stands for the thermionic current.

of disturbances always present at interfaces. These disturbances may be due to diffusive intermixing of the two different materials at the interface. Another source for inhomogeneities may be interface roughness. When the device is grown one has to switch from one material supply to another. At this point the surface is not perfectly flat but will have mono-atomic steps and islands. These structures are then buried by the next material and a rough interface is formed. Because of the different velocities of the charge carriers the voltage drop at the contacts and the electric field at the interface can be assumed as homogeneous. This is the situation when the model (II.1) applies and is illustrated in figure II.3 a).

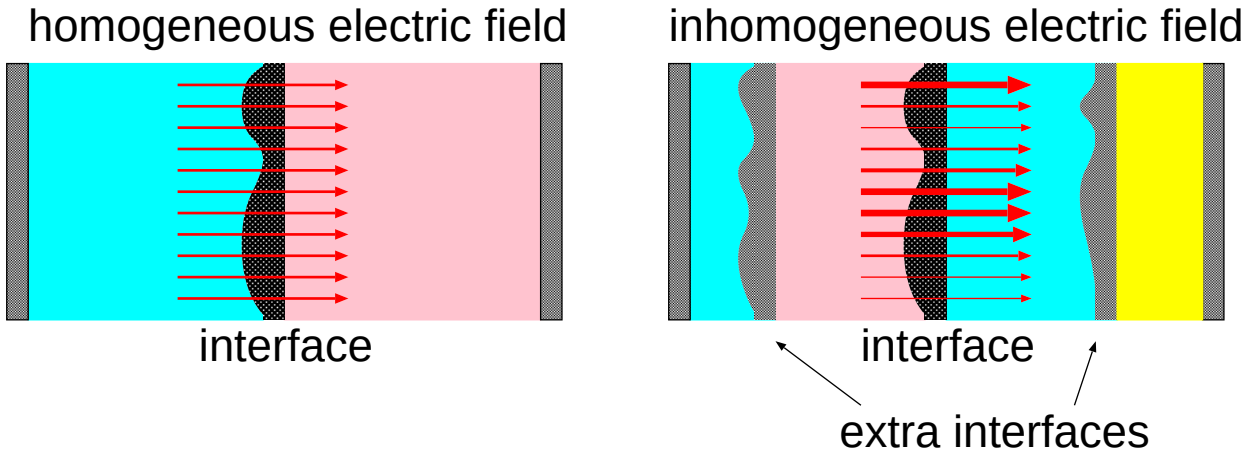

Figure II.3: The two different types of field distributions at the interface. In (a) the interface lays between two metallic contacts and the field distribution is homogeneous. In (b) the interface is embedded between other semiconductor interfaces and the distribution becomes inhomogeneous.

In contrast to the previous paragraph let us now assume that the interface we are

interested in is located between other semiconductor interfaces. This is quite often the case in real devices because of manufactural reasons. For example it might be necessary to protect the materials forming the interface against the atmosphere or it might not be possible to grow metallic contacts epitaxially on the materials forming the interface. If we now apply a voltage to the device the voltage drop at the interface is influenced by the surrounding interfaces. Especially if at these interfaces charge carriers can accumulate they will diffuse with a velocity comparable to the velocity at the interface under consideration. As a result the voltage drop at the interface $u(x, y)$ may be inhomogeneous and the time-scales of charge carrier diffusion at the interface of interest and voltage diffusion are of similar size. The inhomogeneity of the voltage drop at the interface is illustrated in figure II.3 b). This is a situation when model (II.2) applies.

With a circuit like the one shown in figure II.4 with a capacitor parallel to the heterostructure device and a load resistor equations (II.1) and (II.2) can be derived for the two discussed cases, respectively. One has to keep in mind that (II.1) and (II.2) are dimensionless equations and all physical quantities have been rescaled to be dimensionless.

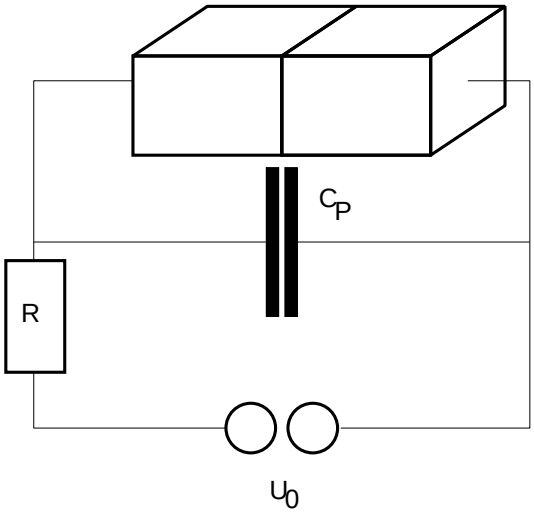

Figure II.4: The circuit in which the heterostructure device is operated.

From the point of view of nonlinear dynamics the difference between these two sets of equations is that (II.1) has a global coupling while in (II.2) a local or diffusive coupling is present. Due to the integral constraint in (II.1) every point in the system is immediately influenced by a change at any other point in the system, while in (II.2) the information of changes is spread only by the diffusion terms and a distant point will experience this change only after a finite time. This will have an effect on the spatial structure of the patterns as we will see later. Structurally the equations fall in the class of reaction-diffusion systems. A generic reaction-diffusion system has the form

$$\tau_u \dot{u}(x,t) = f(x,t) + D\Delta u(x,t) \tag{II.5}$$

with Neumann boundary conditions, where f is called the reaction term, τ_u gives a timescale and D is a diffusion constant, see ,e.g., [49]. Another classification of our

systems comes from the role the variables a and u play in the system. As we will see later in a certain regime in the parameter space an increase of a will lead to an increase of u and a further increase of a. At the same time an increase of u will diminish a. Because of this behaviour a is called an activator and u an inhibitor and we can call (II.1) and (II.2) activator-inhibitor systems [59, 60, 19, 61].

In both sets of equations we can observe two different kinds of instabilities of the homogeneous solution [7]. At the first instability the system stays homogeneous and we will observe periodic homogeneous oscillations, this is called a Hopf instability. The second is the so called Turing instability [62] in the case of (II.2) where the homogeneous steady state will develop into a stationary but inhomogeneous pattern with a fixed wavenumber k or filamentary instability in the case of (II.1) where a single filament emerges. Besides these pure instabilities we will find some interactions between the Turing patterns and the homogeneous oscillations. We will also find cases where the homogeneous oscillations or Turing patterns become unstable, but these instabilities are much harder to discuss analytically in a given model, because it is necessary to know the path of the periodic orbit in phase space, or the shape of the Turing pattern for which in general no analytical description is available.

But now let us have a closer look at the Hopf and Turing instabilities.

II.1.1 Oscillatory/Hopf Instability

In this section we want to study the properties of the homogeneous system. In contrast to chemical systems where the homogeneity can be achieved quite well by stirring the system [49] in our semiconductor system a perfect homogeneity can never be reached, because of imperfections which will appear at the boundaries of different materials. Nevertheless the study of the homogeneous system is useful, because as we will see later on there are conditions where the system only reacts to homogeneous perturbations or will only show a homogeneous answer to any perturbation.

We present only a summary of the linear stability analysis, a detailed discussion can be found in e.g. [63] or in [64]. For a general introduction see [65, 48].

First we will have to find the spatially homogeneous steady states. There are two conditions, namely $\partial u/\partial x = \partial u/\partial y = \partial a/\partial x = \partial a/\partial y = 0$ for the homogeneity. From this requirement we can derive $\Delta u, a = 0$ and $\langle u, a(x)\rangle = u, a(x) = const$ for $x \in [0, L]$. Using this result we see that the two sets of equations (II.1) and (II.2) both contain the same set of equations when restricted to homogeneous states:

$$\begin{aligned} \dot{u} &= \alpha(j_0 - (u - a)) = f(u, a) \\ \dot{a} &= \frac{u - a}{(u - a)^2 + 1} - Ta = g(u, a) \end{aligned} \tag{II.6}$$

The second condition is $\partial u, a/\partial t = 0$ for the stationarity. With these two conditions the

homogeneous steady states are given by

$$0 = \alpha(j_0 - (u - a)) \tag{II.7}$$
$$0 = \frac{u - a}{(u - a)^2 + 1} - Ta \tag{II.8}$$

From (II.7) we get $j_0 = u - a$ and with (II.8) this leads to

$$u = \frac{1}{T}\frac{j_0}{j_0^2 + 1} + j_0 \tag{II.9}$$

The inverse of the $u(j_0)$ relation in (II.9) defines the current-voltage characteristic $j_0(u)$ of the homogeneous fixed points. For $T < 1/8$ this characteristic has an S-like shape as shown in figure II.1.

Another way to find the current-voltage characteristic is to look at the crossing points of the null-clines $f(u, a) = 0$ and $g(u, a) = 0$. This will also give a characterization of the system, namely if it is bistable, excitable or oscillatory [59]. In figure II.5 we can see that our system is oscillatory or excitable depending on the choice of j_0. If we would assume a finite load resistor even a bistable system would be possible [66]. But here we will discuss the oscillatory case, exclusively.

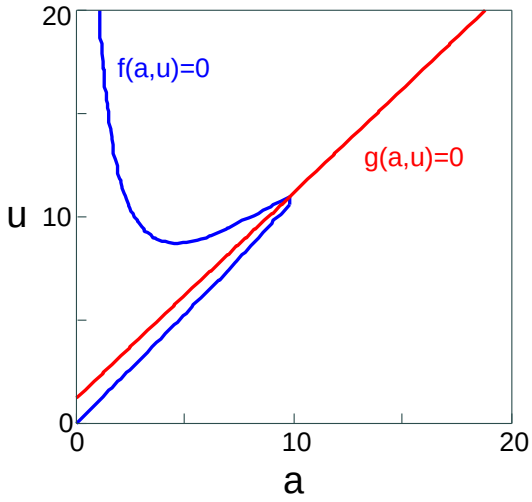

Figure II.5: Null clines of a single oscillator given by the zero of the reaction terms of equations (II.1) and (II.2).

Now that all the homogeneous steady states are known the question arises if all of them are stable against homogeneous perturbations. The homogeneous fixed points will be denoted by an asterisk ("$\star$"), e.g. $u^\star$ and $a^\star$. We will add a small perturbation to the fixed points and want to see if it will grow or decay in time

$$u(t) = u^\star + \delta u(t) \tag{II.10}$$
$$a(t) = a^\star + \delta a(t) \tag{II.11}$$

Because the perturbations are small we do not use the whole nonlinear system, but only the Taylor expansion up to the first order around the fixed point, i.e we only consider the linear part of the system (II.6)

$$\begin{aligned} \dot{u}(t) &= \frac{\partial f}{\partial u}|_{(u^\star,a^\star)}\delta u + \frac{\partial f}{\partial a}|_{(u^\star,a^\star)}\delta a \\ \dot{a}(t) &= \frac{\partial g}{\partial u}|_{(u^\star,a^\star)}\delta u + \frac{\partial g}{\partial a}|_{(u^\star,a^\star)}\delta a \end{aligned} \tag{II.12}$$

If we now specify the perturbations δu and δa as

$$\delta u(t), \delta a(t) \sim \mathrm{e}^{\lambda t} \tag{II.13}$$

equation (II.12) can be written in matrix notation:

$$\lambda \begin{pmatrix} \delta u \\ \delta a \end{pmatrix} = \begin{pmatrix} \frac{\partial f}{\partial u} & \frac{\partial f}{\partial a} \\ \frac{\partial g}{\partial u} & \frac{\partial g}{\partial a} \end{pmatrix}\Bigg|_{(u^\star,a^\star)} \begin{pmatrix} \delta u \\ \delta a \end{pmatrix} = \mathcal{M} \cdot \begin{pmatrix} \delta u \\ \delta a \end{pmatrix} \tag{II.14}$$

In equation (II.14) λ can be seen as the eigenvalue of the matrix $\mathcal{M}$. Since λ enters in the exponent of the perturbation in equation (II.13) the following is now obvious. If $\Re(\lambda) < 0$ a small perturbation decays in time and the systems stays stable. On the other hand if $\Re(\lambda) > 0$ a small perturbation grows exponentially and the homogeneous stationary state is unstable.

The partial derivatives are given by:

$$\left.\frac{\partial f}{\partial u}\right|_{(u^\star,a^\star)} = -\alpha \qquad \left.\frac{\partial f}{\partial a}\right|_{(u^\star,a^\star)} = \alpha \tag{II.15}$$

$$\left.\frac{\partial g}{\partial u}\right|_{(u^\star,a^\star)} = \frac{1-j_0^2}{(j_0^2+1)^2} = -\gamma \qquad \left.\frac{\partial g}{\partial a}\right|_{(u^\star,a^\star)} = \frac{j_0^2-1}{(j_0^2+1)^2} - T = \gamma - T \tag{II.16}$$

and

$$\mathcal{M} = \begin{pmatrix} -\alpha & \alpha \\ -\gamma & \gamma - T \end{pmatrix} \tag{II.17}$$

where we used

$$\gamma = \frac{j_0^2-1}{(j_0^2+1)^2} \tag{II.18}$$

to simplify the expressions. If we now calculate the eigenvalues λ of $\mathcal{M}$ we get only negative real parts of the eigenvalues under the condition:

$$\gamma - T < \alpha \tag{II.19}$$

and the homogeneous fixpoint is stable. If

$$\gamma - T > \alpha \tag{II.20}$$

one eigenvalue has a positive real part and the homogeneous state is unstable. At the point

$$\gamma - T = \alpha \tag{II.21}$$

the two eigenvalues are purely imaginary, but this indicates a Hopf-Bifurcation, i.e. a bifurcation where a pair of complex-conjugate eigenvalues cross the imaginary axis [7].

Now that we know how the system will respond to homogeneous perturbations we will look at what will happen under inhomogeneous conditions.

II.1.2 Turing Instability

In the previous section we have studied the stability of the homogeneous fixed point against homogeneous perturbations, i.e. every point of the system is disturbed in the same way. But in general perturbations in extended systems are not homogeneous. To include spatially inhomogeneous perturbations in our study we extend the deviation from the fixed point δu and δa given by (II.13) into the spatial dimensions

$$\begin{aligned} \delta a(\vec{x},t) &\sim \sum_i \beta_i \Psi_i(\vec{x}) \mathrm{e}^{\nu_i t}, \\ \delta u(\vec{x},t) &\sim \sum_i \gamma_i \Psi_i(\vec{x}) \mathrm{e}^{\nu_i t}, \end{aligned} \tag{II.22}$$

where $\vec{x}$ defines a point in the given n-dimensional domain and $\Psi_i(\vec{x})$ are the eigenfunctions of the Laplacian in the given domain with the eigenvalues ν_i.

Now we have to consider the two sets of equations (II.1) and (II.2) separately, because the spatial part of the equations differ. If we substitute δu from (II.13), because in (II.1) u is still homogeneous, and δa from (II.22) in (II.1) we can see that we get the same description of the homogeneous state, as in section II.1.1, if we set the ground mode $\Psi_0 = const = 1$. The average $\langle \Psi_i \rangle$ for all other modes with $i > 0$ is always zero for Neumann boundary conditions. The stability of the i-th inhomogeneous mode is determined by

$$\lambda = \frac{\partial g}{\partial a} + \nu_i \tag{II.23}$$

Inhomogeneous modes can grow if $\lambda > 0$. All eigenvalues ν_i of the Laplacian are negative, except ν_0 which is 0, and their absolute value increases with the number of nodes of the eigenfunctions. As a consequence the fastest growing mode is the one with the

fewest nodes as long as $\partial g/\partial a$ is positive and larger than the norm of the corresponding eigenvalue. If $\partial g/\partial a$ is smaller for a given domain it is in general possible to reduce the norm of the eigenvalue by increasing the size of the domain.

As a summary we can say that a linear stability analysis indicates that in the globally coupled system (II.1) the strongest growing inhomogeneous mode is the eigenfunction of the Laplacian with the fewest number of nodes, in general this means one node. The mode can grow if the norm of the corresponding eigenvalue $|\nu_c| < \partial g/\partial a$, i.e. the system has to be large enough and $\partial g/\partial a$ has to be positive.

The same procedure for the locally coupled system (II.2) leads to the matrix $\mathcal{M}^l$ for the i-th mode:

$$\mathcal{M}^l = \begin{pmatrix} \frac{\partial f}{\partial u} + \nu_i & \frac{\partial f}{\partial a} \\ \frac{\partial g}{\partial u} & \frac{\partial g}{\partial a} + D\nu_i \end{pmatrix} = \mathcal{M} + \begin{pmatrix} \nu_i & 0 \\ 0 & D\nu_i \end{pmatrix} \tag{II.24}$$

Here one can see that for the 0-th mode, i.e. the homogeneous mode where $\nu_0 = 0$ we get the same $\mathcal{M}$ as defined in (II.14).

Performing the same analysis as in the previous section we get the stability criterion of a stationary fixed point against inhomogeneous perturbations:

$$\gamma_T < \left(\sqrt{T} + \sqrt{\frac{\alpha}{D}}\right)^2 . \tag{II.25}$$

At the threshold the first unstable wave vector is given by

$$|\vec{k_c}| = \sqrt[4]{\frac{\alpha T}{D}} \tag{II.26}$$

II.1.3 Numerical Integration of partial differential equations

We want to study the properties of the systems (II.1) and (II.2) on a two dimensional domain. We will restrict the investigations to square and rectangular domains. Because of this restriction we use a finite-difference scheme to discretise the domain. For the temporal integration mainly a forward-Euler scheme is used, but all important results are also checked with a fifth order Runge-Kutta and a variable order Adams-Bashford scheme from the SLATEC Common Mathematical Library [67].

II.2 Global Coupling

II.2.1 1-dimensional properties

Before we investigate the properties of the 2 dimensional system we will summarise the features in one spatial dimension. Detailed discussions can be found in [42, 63].

In agreement with the linear stability analysis we find homogeneous oscillations and a stationary filamentary structure. Additionally a mode where a filament on one side of the domain appears and disappears in a short time can be found. We call this behaviour spiking. In this mode the filaments can appear in a periodic or in a chaotic cycle. With increasing j_0 the chaotic state is reached by period doubling, with decreasing j_0 in a periodic window type-1 intermittency can be found. Depending on the initial conditions in a certain area in the parameter space bistability between an stationary filament and the spiking mode can be found. This is a hint for a subcritical bifurcation, where an unstable solution is connecting the two stable states. This unstable mode was identified to be a breathing mode, i.e. the amplitude and the size of the filament oscillates periodically. The amplitude of this oscillation is small when near the stationary filament and increases when moving along the unstable branch connecting filament and spiking mode away from the filament.

The chaotic spiking mode was found to show only low dimensional chaos. This was shown by the calculation of the Lyapunov-exponents and the Kaplan-Yorke [68] fractal dimension, which , e.g., has a maximum value of 2.094 at $j_0 = 1.313$ for $\alpha = 0.05$ and $T = 0.035$, and by analysing periodic and chaotic modes with the help of the Karhunen-Loéve decomposition [45]. The spatial structure is completely dominated by the temporal evolution which can also be shown by plotting the amplitude of the spike over the temporal distance to the previous one which shows a simple linear dependence. Chaos control has also been successfully applied to this system by using a time delayed feedback [69].

II.2.2 Stationary structures

If we use a square domain where the length of the edges is $L_x = L_y = 30$ we can find three different types of stationary structures, namely a (hot)-corner filament, a edge current layer and a cold corner filament as show in figure II.6. It is easy to see that the hot filament is connected with a smaller current through the device, while the cold corner filament can hold a larger current and the edge current layer lays in between. To illustrate this we have plotted the current-voltage characteristics of the three different filaments in figure II.7.

If we start with a value of j_0 which is slightly above the critical value where inhomogeneous modes start to grow and perturb the homogeneous system we will end up with a hot filament. We will stay on the branch of the current-voltage-characteristics with increasing j_0, until we reach a value of about 3. Here the hot filament loses stability and the system switches to the edge current layer where it stays until the edge current layer becomes unstable at about $j_0 = 4.5$. The homogeneous branch is already stable against small fluctuations in this area so that the system can get homogeneous or switch to the cold corner filament. When we decrease j_0 starting with large values the sequence of modes is reversed.

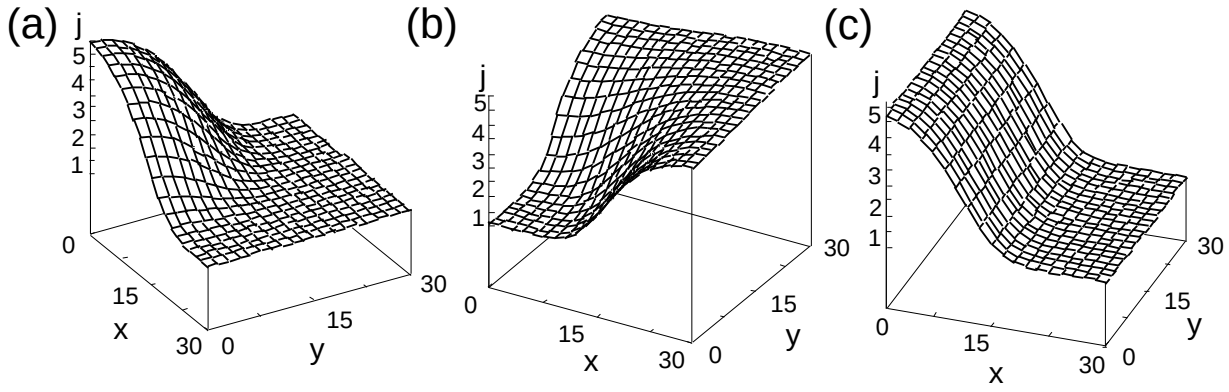

Figure II.6: The three different stable structures in the global coupled system. a) hot-corner filament, b) edge current layer and c) cold filament.

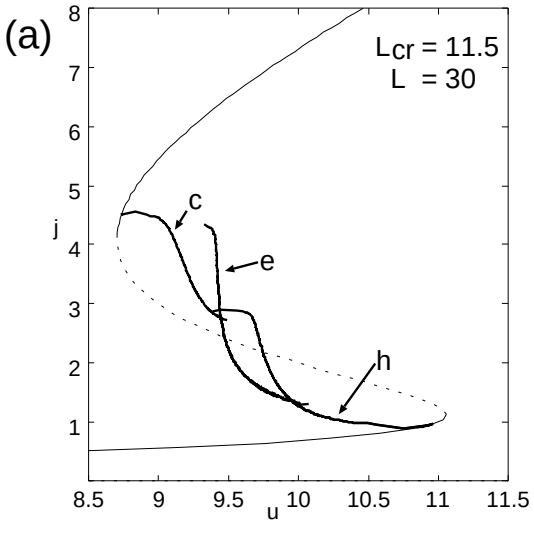

Figure II.7: Current-voltage characteristics of a system with size L=30. The homogeneous steady state can be found on the light grey line while hot and cold filament and the edge current layer are denoted by h, c and e, respectively.

For a given j_0 it is possible that there are more than one stable solution, this is called bistability, if there are two solutions, or multi-stability if there are even more stable states. In figure II.7 we have a large regime of bistability between hot filament and edge current layer and another regime where the cold corner filament and the edge current layer are stable. If we keep the voltage fixed we can find a well defined voltage range with bistability between hot filament and edge current layer. This makes it possible to switch the device between two states with different currents. If, e.g., the device is operated at $u \approx 9.8$ a short and small pulse of $|\delta u| \approx 0.5$ can switch to the high current state (hot filament) if δu is positive and to the low current state (edge current layer) if δu is negative. Similar studies were performed in semiconductor superlattices [70], where the number of branches in the current-voltage characteristics corresponds to the number of periods in the superlattice [71].

The branches of the hot filament and the cold filament are not open ended as figure

II.7 might suggest, they are connected by an unstable branch with positive differential conductivity, but we were not able to follow this branch, because the system moves very fast to the edge current layer in this regime of parameter space.

The difference between the edge current layer and the hot or cold filament respectively should decrease with increasing system size. The curvature of the hot and cold filament becomes smaller and observed from a point in the system somewhere at the boundary between the areas of high and low current density it becomes harder and harder to distinguish between a corner filament and a edge current layer. This can also be seen in the current-voltage-characteristic of a large system shown in figure II.8.

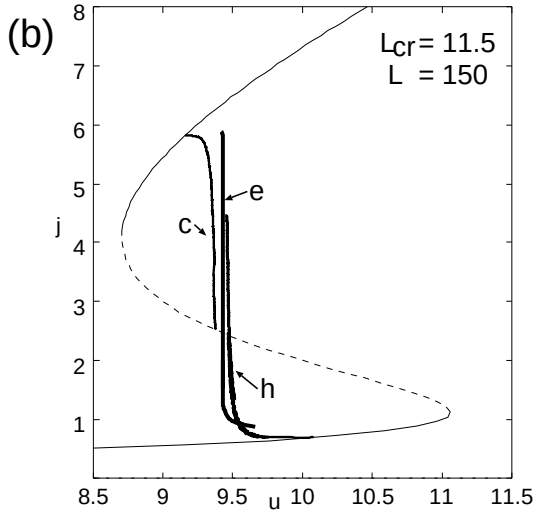

Figure II.8: Current-voltage characteristics of a system with size L=150. The homogeneous steady state can be found on the light grey line while hot and cold filament and the edge current layer are denoted by h, c and p, respectively.

Here the system is 5 times larger and we can see that the three branches lie in parallel for $1.5 < j_0 < 5.5$. In this area the branches are also nearly vertical, i.e. the current through the device j_0 can be changed significantly with only a small change in the applied voltage u.

The three modes we discussed above are the only stable stationary modes. Other modes can be prepared, but they are unstable as we will see in the following.

If we perturb the homogeneous steady state in the very centre of the domain a stationary filament in the centre of the domain will grow. This is not in contrast to the previous results, because the systems is trapped in a symmetric sub-space. It has to be noted that in a discretized system, e.g., when integrating the system numerically, the symmetry of the initial perturbation has to be the same as the symmetry of the discretization lattice. If this is not the case, some parts of the system already lie outside of the symmetric sub-space and this parts will dominate the temporal evolution. Now we take the prepared centre filament and apply some small, but symmetry-breaking noise. The result is show in figure II.9

Because of the noise, some part of the system has left the symmetric sub-space and starts to move away from it, forcing the rest of the system to follow. Finally, one of the

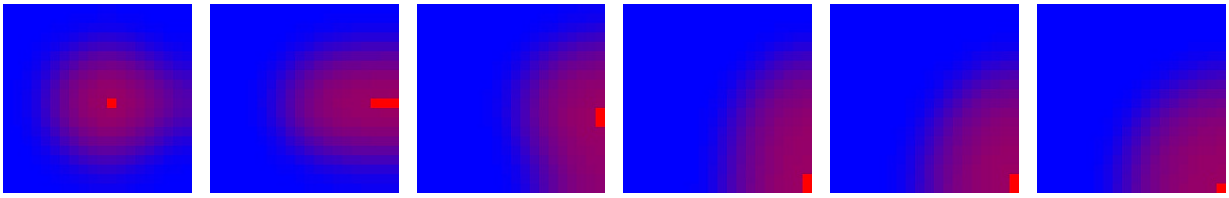

Figure II.9: A filament moving from the core of the domain into a corner. $j_0 = 1.24$, $\alpha = 0.035$, $L = 40$

three stable stationary structures is reached; in figure II.9 it is the hot corner filament. In this sequence of figures it looks as if the boundary attracts the filament.

We will use this specially tuned system to measure the influence of the boundary by measuring the time the perturbed central filament needs to reach a corner of the domain. This transition time τ as a function of the system-size L is plotted in figure II.10. A similar plot we will see later (figure II.11) when we look at the influence of disorder along the interface. It can be see from the exponential increase of the transient time $\tau \sim \mathrm{e}^L$ that in an infinitely large system a central filament is stable because $\tau \to \infty$. One could also say that the positive eigenvalue $\lambda_1 \sim 1/\tau$ connected with the translation mode goes to 0 if $L \to \infty$ [72].

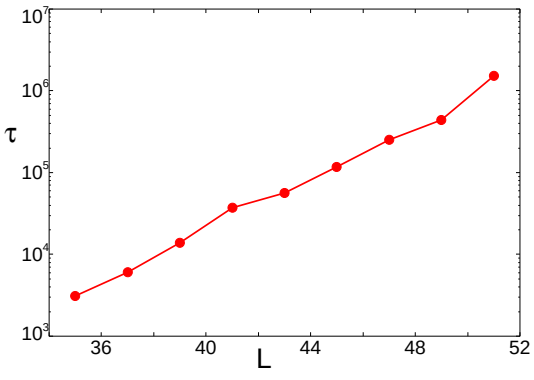

Figure II.10: Transition time τ of a central filament moving to a corner of the domain as a function of the system-size L. Parameters: $j_0 = 1.31$, $\alpha = 0.05$

II.2.3 Boundary Conditions

As we have seen from the linear stability analysis and also from the numerical integration of (II.1) the filamentary structure always moves to the boundary of the system. All other configurations are only stable in a subspace with the same symmetry. This is an effect of the applied Neumann boundary conditions. With, e.g., periodic boundary conditions somewhere in the domain a circular filament will grow. The position will depend on the initial conditions. The fact that Neumann boundaries attracts filament can be proven analytically for a general system with an S-shaped current voltage characteristic and global coupling on a convex domain as discussed in [73]. This is in

agreement with other numerical studies of reaction-diffusion systems in two dimensions like [74, 61]. Here also a single filament in a model for a p^+-n^+-p-n^--diode moves to the boundary of the domain.

II.2.4 Influence of Localised Perturbations

As already mentioned there are always spatial perturbations of different kind in a real semiconductor system. For this reason spatial modes should always be included in the linear stability analysis. However the linear stability analysis is only valid for small perturbations. If for some reason the defects are larger, the systems response may change considerably and will show some totally new behaviour. Also disturbances from, e.g. some lattice defects at the interface, which will be constant in time are not covered by the linear stability analysis. In the above considerations the perturbation is present only at a single point in time t_0. In this section we want to see how the behaviour of (II.1) is changed by certain perturbations, namely how defects can influence the filaments.

We have mentioned earlier that the parameters T and D describe some internal properties of the device. Although D is not defined in (II.1) there is still a diffusion constant of size 1 in front of the Laplacian in (II.1). Because defects are localised perturbations we will consider T and the diffusion coefficient as functions of the position on the interface. Both parameters can be connected to certain defects of the boundary by the following phenomenological arguments. Assuming that D varies on the interface implies that electrons will move faster or slower at certain regions along the interface. This can be explained by a higher concentration of impurities which will trap or scatter electrons, or a larger number of defects in the periodicity of the lattice. In the model of the HHED T is the tunnelling rate through the potential barrier which is formed by the interface. If the barrier is lowered T becomes larger. This can be due to some stronger intermixing of the different types of material on the two sides of the interface.

To study the effects of those perturbations we will apply them separately and restrict ourselves to strongly localised perturbations. In a real system the defects will be randomly distributed along the interface but to see the influence of the perturbations more clearly we will apply a single one in the centre of the interface only.

Because of their physical meaning only certain ranges for T and the diffusion coefficient are sensible. Therefore T should be always larger than the value for the ideal, homogeneous case, since intermixing will only lower the barrier and not increase it. The diffusion constant should be smaller than 1 because the mobility of electrons can not be increased by defects.

II.2.5 Perturbations in T

We will now apply a perturbation to the parameter T in a way that only at a certain area $T(x, y)$ will have a different value from $T_0 = 1/20$

$$T(x,y) = T_0 + \delta T(x,y)$$
$$\delta T(x,y) = \begin{cases} 0 & (x,y) \in [0,L] \times [0,L] \not\subset \mathcal{C} \\ \delta T & (x,y) \in \mathcal{C} \end{cases}$$
$$\mathcal{C} \subset [0,L] \times [0,L] \quad \text{(II.27)}$$

We use the value $\delta T/T_0$ to characterise the strength of the perturbation.

If we increase δT step by step from $T_0 = 1/20$ with all other parameters fixed the final position of the centre of the filament will move from the boundary to the centre of the interface at δT_c. It is obvious that δT_c is dependent on all system parameters, but we will only study the influence of one single parameter, namely the system-size L. This will illustrate how the influence of the boundary decays when the system grows. With random initial conditions we try to find δT_c. The result is shown in the following figure II.11.

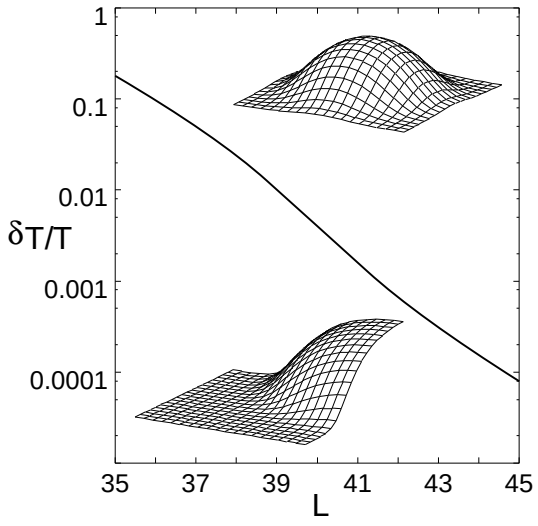

Figure II.11: Influence of a local perturbation $\delta T/T_0$ on the position of the filament as a function of the system size L.

The critical value for δT for large system sizes is given by the fact that the perturbation to the system due to the random initial conditions must not be larger than the localised perturbation. For these system-sizes the critical transmission coefficient δT_c is so small that the perturbation is not ″seen″ by the system. For small systems the central filament nearly touches the boundary and it makes no sense to distinguish between a central filament and a boundary state.

II.2.6 Oscillating structures

If we take smaller system-sizes like, e.g., $L_x = L_y = 20$ oscillating filaments can be found for similar parameter values as for spiking in one spatial dimension for $L = 40$. These structures can be found in an area of the parameter space where homogeneous oscillations and the stationary filament are both unstable [72]. This is illustrated by the following diagram of the α-j_0 parameter space II.12 for a system with $L_x = L_y = 20$.

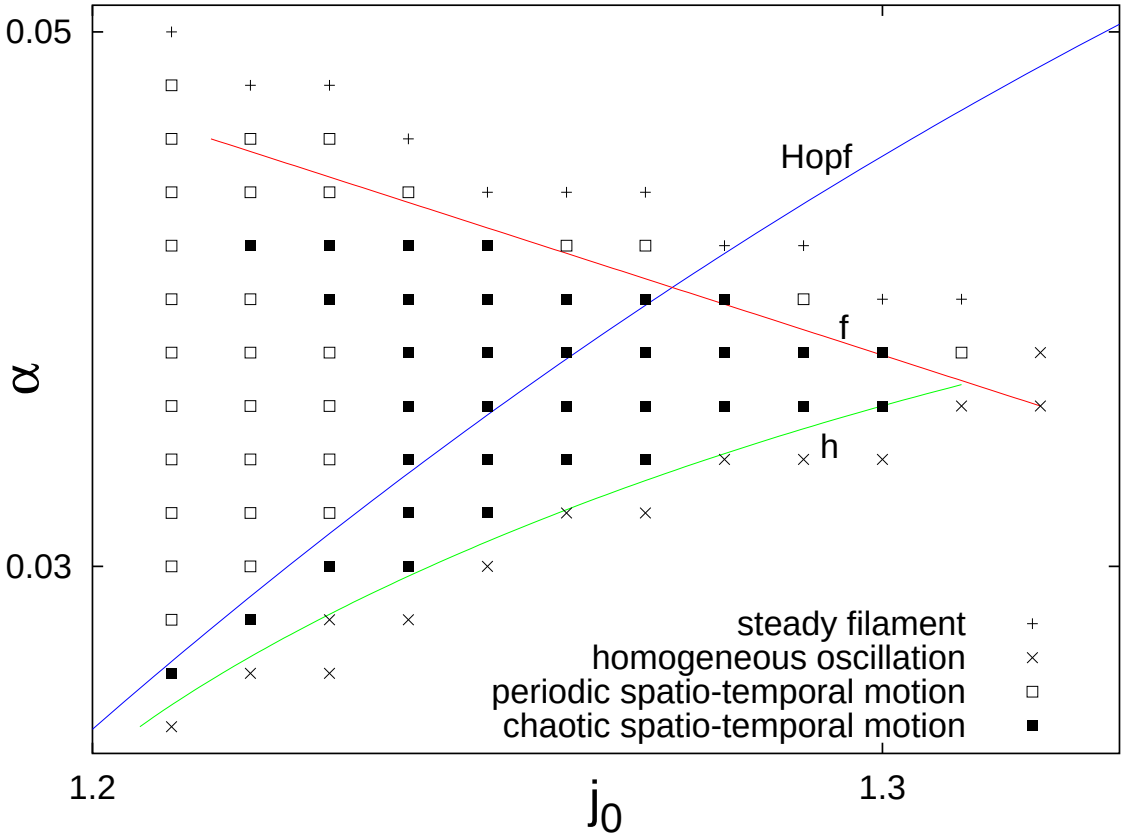

Figure II.12: Map of the α-j_0 parameter space for a system with $L_x = L_y = 20$. The symbols denote the patterns which can be found with an initial condition near the homogeneous state. The solid lines mark the Hopf-Bifurcation of the homogeneous steady state (Hopf, blue) and the points where the homogeneous oscillation (h, green) and the stationary hot corner filament (f, red) looses stability.

The solid green line labelled by "h" indicates the boundary where homogeneous oscillations become unstable. Below the line oscillations are stable, above they are unstable against inhomogeneous fluctuations. The solid red line labelled by "f" marks the points where the stationary filament undergoes a Hopf-Bifurcation and loses stability. Here filaments are stable above the line and unstable below. The symbols in the map roughly specify what structures can be found with initial conditions near the homogeneous steady state (random initial conditions). In the following we will discuss the

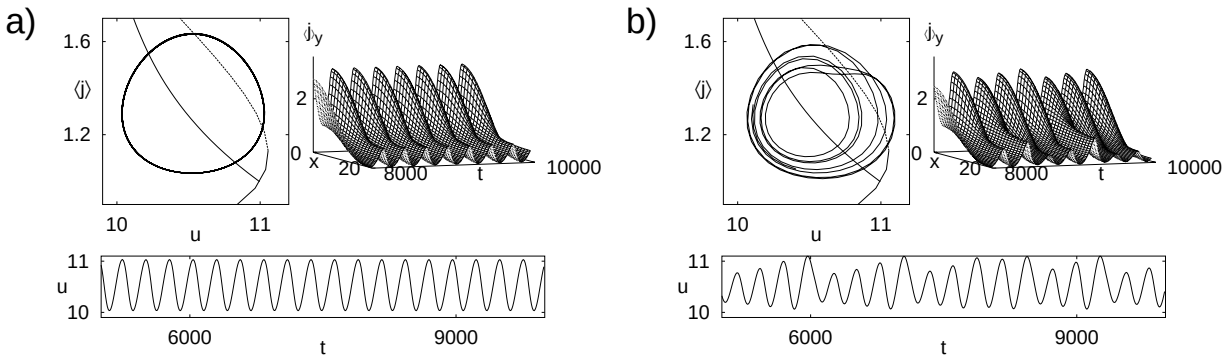

Figure II.13: Periodic and chaotic breathing shown in the temporal evolution of u, in a $\langle j \rangle$-u phase portrait and the temporal evolution of the spatial average over the y component of j.

different classes of structures.

Breathing filaments

The breathing mode can be reached from stationary filaments by the reduction of α and/or j_0 via a Hopf bifurcation which can be sub- or supercritical. Near the stability boundary the oscillation is periodic but it may undergo a period doubling bifurcation which eventually leads to chaos. In figure II.13 the temporal oscillation of u and the corresponding $\langle j \rangle$-u plot are shown for periodic (a) and chaotic breathing (b). Additionally the spatial structure is indicated by the temporal evolution of $\langle j \rangle_y$, which denotes the spatial average over the y component of $j(x, y)$.

It can clearly be seen that the breathing mode and the spiking mode, which we will discuss in the following section are two different modes. For breathing filaments the oscillation of u is still very harmonic and the phase-portrait is nearly circular. Also the amplitude of the filament is always considerably larger as compared to the spiking mode, where it nearly vanishes.

Spiking filaments

Spiking is characterised by the appearance and the consecutive disappearance of a filament out of a nearly homogeneous state. It appears when the homogeneous steady state is unstable but experiences no oscillatory instability. The stationary filament may be unstable or stable. In the first case the spiking mode is the only attractor in the second we can have bistability between spiking and the steady filament. Spiking can become chaotic via a period doubling cascade with increasing j_0 or via intermittency when the homogeneous oscillations become spatially unstable. Periodic and chaotic spiking is shown in (a) and (b) of figure II.14, in (c) chaotic spiking due to the spatial instability of homogeneous oscillations is shown.

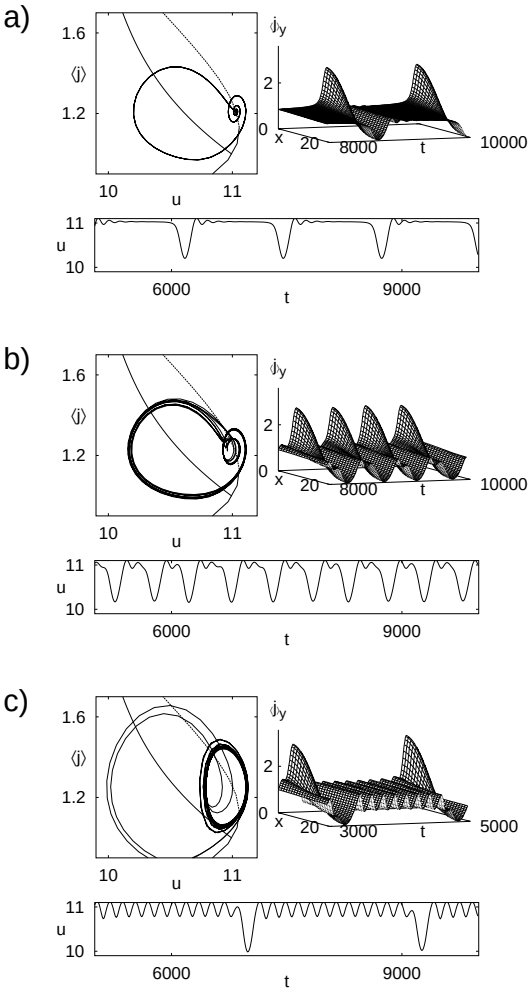

Figure II.14: Periodic (a) and chaotic (b) spiking and chaotic spiking due to the spatial instability of the homogeneous oscillations (c). All three modes are presented by the temporal evolution of u, the $\langle j \rangle$-u phase portrait and the temporal evolution of the spatial average over the y component of j. Parameters: $L_x = L_y = 20$, (a) $\alpha = 0.04$, $j_0 = 1.21$, (b) $\alpha = 0.04$, $j_0 = 1.23$, (c) $\alpha = 0.032$, $j_0 = 1.25$.

The difference to the corresponding plots of the breathing modes is clearly visible. Firstly we realize a burst like structure in the phase portrait and the time dependence of u. Secondly we observe long time intervals the system stays near the homogeneous state which can be seen in the $\langle j \rangle_y$ plot.

Saddle-type instabilities

So far we have seen a temporal instability of the steady filament and a spatial instability of the homogeneous state. In the following we will discuss what happens if both instabilities occur simultaneously.

If figure II.15a) the following scenario can be observed. The stationary filament is unstable against homogeneous fluctuations and exhibits an oscillatory instability. The instability is connected with a positive eigenvalue which drives the system away from the filamentary state. This can be seen in a breathing mode with growing amplitude.

After some time the amplitude of the breathing becomes comparable to the amplitude of the stationary filament and the system becomes nearly homogeneous. Since the homogeneous state is unstable too the small inhomogeneity which is left grows quite fast and leads the system back close to the filamentary state and the cycle starts again. This is the typical behaviour of Shil'nikov chaos [7].

In the previous example only the saddle motion near the filament was visible. In a more general example shown in figure II.15b) the saddle motion near the homogeneous state is also visible. The scenario is more or less the same as in the previous case only the system now is not pushed away from the homogeneous state immediately but stays near that state for some time until the unstable mode grows again and leads the system near to the filament.

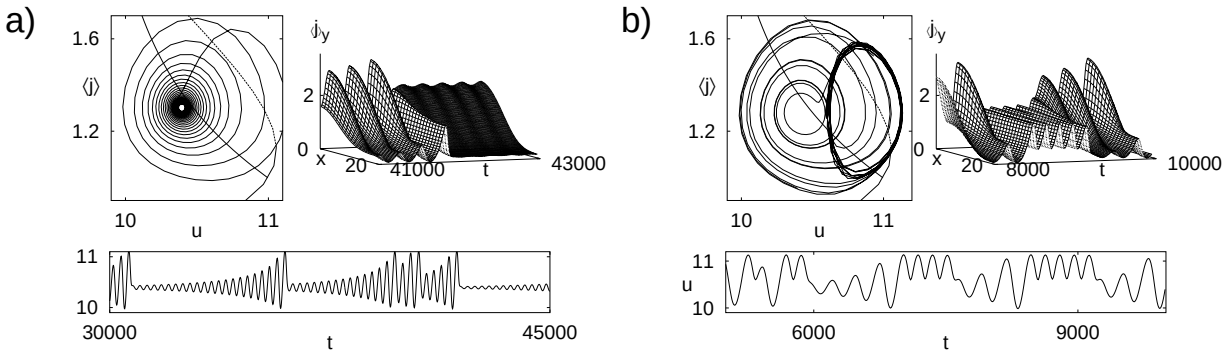

Figure II.15: Chaotic spatio-temporal dynamics of a current filament on a square domain. Due to a saddle type instability breathing oscillations with growing amplitude drive the system near the unstable homogeneous state from where it is pushed back to the filamentary state immediately (a) or after a couple of nearly homogeneous oscillations (b). Parameters: $L_x = L_y = 20$, (a) $\alpha = 0.0368$, $j_0 = 1.302$, (b) $\alpha = 0.035$, $j_0 = 1.28$.

So far we have only looked at small systems, i.e. systems whose size is only slightly larger than the critical size, which here is about $L_{min} \approx 11.5$. For system sizes close to L_{min} breathing is the only spatio-temporal mode which can be observed. At an intermediate size the saddle type motion dominates. In large system only the spiking mode can be found in a small area of the parameter space which becomes smaller with increasing system size. Furthermore the spatial structure of the spiking mode is different in large systems and leads to limit-cycle oscillations of a current density front.

Periodic limit-cycle oscillations of a current density front

For large system the spatio-temporal evolution of the spiking mode cannot be described by the simple picture of growing or shrinking of the amplitude of a single mode. Rather it is a cycle of four different stages which are illustrated by several snapshots of the spatial structure of the filament in figure II.16. At the beginning the homogeneous state

looses stability with respect to inhomogeneous perturbations and a small filament with a characteristic size of L_{min} is formed.

In the second stage the filament or high conducting state propagates into the low conducting area. During this motion the current through the device $\langle j \rangle$ increases while the applied voltage u decreases. This motion continues until the voltage u drops below a critical value u_c which is correlated to with the radius of the stationary corner filament. In [75] and [76] this is discussed for a similar case in a drift-diffusion system. For planar fronts an analogous scenario exists where u_c corresponds to the voltage u_{co} where on- and off-states coexist with a planar boundary. u_{co} is given by the equal area rule

$$\int_{a_{\text{off}}}^{a_{\text{on}}} f(a, u_{co}) da = 0. \tag{II.28}$$

The integral is taken from a_{off} to a_{on} which are the values of the variable a which corresponds to the turning points of the current-voltage characteristic.

When u becomes smaller than u_c the front moves backwards and shrinks until it finally disappears. During the last stage the system is nearly homogeneous and moves along the lower stable branch of the current-voltage characteristic until it reaches the initial point again. During the final stage the inhomogeneity becomes very small and as a result the instability which leads to the initial filament in the first stage grows very slowly and the period of the oscillation becomes very large.

In a realistic system noise should be included. If in such a system the amplitude of the inhomogeneity drops below the noise level the period is no longer determined by the internal dynamics but by the noise alone. Another problem that is connected with a very small amplitude of the inhomogeneity arises during the numerical integration of the system. Because of the finite accuracy of the numbers stored in the computer's memory the amplitude may eventually drop below this accuracy and the system is, from a numerical point of view perfectly homogeneous. As a result it will stay homogeneous forever. To avoid this effect it might be necessary to include some artificial noise to the numerical integration. This technique is not intended for triggering spikes but to prevent the amplitude of the inhomogeneity from becoming smaller than the used numerical accuracy.

II.3 Local Coupling

The behaviour of the system changes drastically when we drop the global coupling and consider diffusive coupling. As already mentioned this means that we now will have a look on semiconductor devices with a linear contact region or multilayer devices where the important interface can be found between several other semiconductor-semiconductor interfaces. Here only next neighbours are coupled with each other and

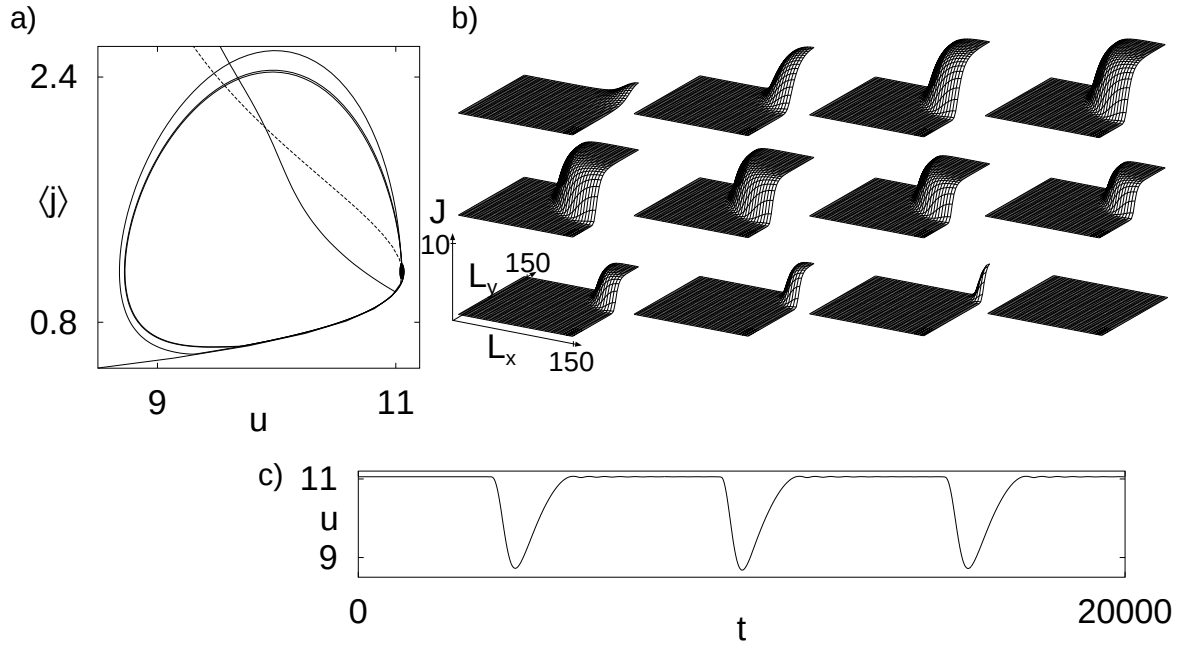

Figure II.16: Periodic limit-cycle oscillation of a current density front. In (a) the u-$\langle j \rangle$ phase-portrait is shown, the spatial distribution of the current density for different times is shown in (b) and the time evolution of u can be seen in (c). Parameters: $L_x = L_y = 150$, $\alpha = 0.005$, $j_0 = 1.13$. Spatially random persistent noise with an amplitude of $\delta a = 0.0001$ every $\delta t = 1000$ time steps is added to trigger the instability of the uniform state.

a perturbation will need a certain time to spread across the system. As shown in section II.1.1 the homogeneous system is the same as for the globally coupled system. This means all homogeneous properties are the same as well. On the other hand the linear stability analysis for inhomogeneous perturbations in section II.1.2 has shown that the two systems react differently to this kind of perturbation. While in the globally coupled system the mode with the smallest k compatible with the boundary conditions dominates the system, the system with local coupling favours a mode with $k = k_c$, where k_c is a function of all other system parameters. In the following we will discuss (II.2) in a similar fashion as (II.1) in the previous section. First a summary of the 1D system is given and the stationary and oscillatory modes are studied.

II.3.1 1-dimensional properties

The integration of the one dimensional system leads to a variety of different forms of behaviour [45, 44]. Besides homogeneous oscillations and stationary filaments which were predicted by the linear stability analysis and can also be observed in the locally coupled system, a remarkable new feature is the existence of a long transient time τ of the system. This means a periodic attractor is reached only when the system is integrated for a

sufficiently long time. One can look a little more carefully on τ by integrating the system with a large number of different initial conditions and determining the transient time τ. If we now plot the number of systems still in the transient phase after a certain time t we get an exponentially decaying function shown in figure II.17. This is a first hint for a transient chaotic phase [77, 43]. Transient chaos is determined by the existence of a chaotic or strange repeller. Repellers are in a certain sense the opposite of an attractor. Where an attractor "attracts" a trajectory which comes close a repeller "repels" nearly every trajectory in its vicinity. Because of its complex topology a trajectory can stay for a long time near a chaotic repeller before it can find an attracting object in phase space. We say "nearly every trajectory", since in general a repeller is a saddle with stable and unstable directions. If the system is on its stable manifold, then for $t \to \infty$ we reach the repeller, but if there is only a small component in the unstable manifold, which is always the case, if some noise is involved, then this component will grow and take the system eventually away from the repeller.

Transient chaos

To characterise the repeller a bit more closely and also to be sure that we really have a chaotic object, we have calculated the largest Lyapunov-exponents. We have used an algorithm which is independently described in [78] and [79]. In principal one can calculate the whole Lyapunov-spectrum using this method, but we calculated only the largest few Lyapunov-exponents as were necessary to calculate the Kaplan-Yorke dimension. Because of the transient nature of the unordered phase we modified the Lyapunov algorithm a little. In principle Lyapunov-exponents are defined in the limit for $t \to \infty$. In the numerical algorithm this condition was translated into a limit over a very long time to achieve good convergence. Some test have shown that the convergence in the transient phase is quite good when extending the limit over 5000 time steps. With this prerequisite we define a time-dependent Lyapunov-exponent at a time t by taking the limit over the last 5000 time steps. The result is shown in figure II.18. We can see, that not only the largest but a couple of Lyapunov-exponents are positive although with quite a small positive value. However it is now necessary to make sure that these exponents are the result of the chaotic nature of the repeller and not a consequence of its repelling character only. To do this we have to evaluate the escape rate r_e, which is given by a statistic over different initial conditions and fixed parameters. If we define $A(t)$ as the number of systems with a transient time $\tau \geq t$ the following relation is true

$$A_L(t) \sim \exp(-t r_e(L)). \tag{II.29}$$

Now we can easily estimate the escape rate r_e with an semi-logarithmic plot as shown in figure II.17. For this figure we used a system of size $L = 600$ and we find $r_e(L = 600) = 4.2 \cdot 10^{-5}$. A typical evolution of the two largest time-dependent Lyapunov exponents for the same system is shown in the following figure II.18. The largest

Lyapunov exponent is of the order of $2.5 \cdot 10^{-3}$ which is considerably larger than the escape rate r_e and this confirms that we really have a chaotic transient.

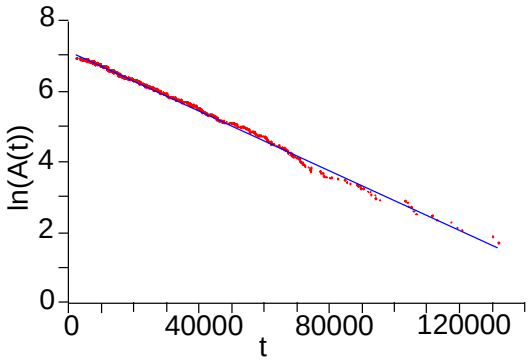

Figure II.17: The number $A(t)$ of systems with a transient time $\tau \geq t$ in a semi-logarithmic plot. The escape rate r_e is give by the slope.

The spectrum of the largest Lyapunov exponents of larger systems is shown in figure II.19. It is evident that the number of positive Lyapunov exponents increases with the system size. This is typical for extensive systems. While the number of positive Lyapunov exponents increases the absolute value of the largest one does not change much. If we increase the system size even further more and more Lyapunov exponents have to fit into a fixed interval and in the limit of an infinite system size we get a band like distribution of positive Lyapunov exponents. This is qualitatively illustrated in figure II.20.

As we now know the Lyapunov spectrum we can calculate the Kaplan-Yorke dimension D_{KY}

$$D_{KY} = j + \frac{1}{|\lambda_{j+1}|} \sum_{i=1}^{j} \lambda_i, \tag{II.30}$$

where λ_i is the ordered Lyapunov spectrum and the number j is given by

$$\sum_{i=1}^{j} \lambda_i > 0 \qquad \text{and} \qquad \sum_{i=1}^{j+1} \lambda_i < 0. \tag{II.31}$$

This dimension increases linearly with the system size L and we can define a size independent dimension- or Lyapunov-density d_{ky}

$$d_{ky} = D_{ky}/L \tag{II.32}$$

which does not change with the system-size. Another interesting is the so called Karhunen-Loève dimension D_{KLD} [80]. A discussion of D_{KLD} for our system can be found in [46].

Codimension-two Turing-Hopf Point

This system does on the other hand not only have an interesting transient behaviour, it also shows quite complex periodic patterns. A typical example and also one of the

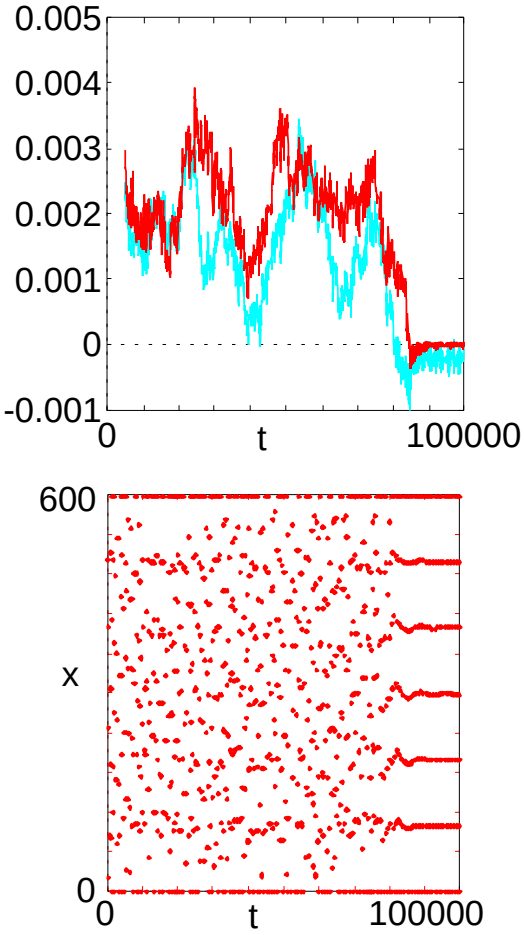

Figure II.18: The temporal evolution of the two largest Lyapunov exponents for a system of size $L = 600$ (a) together with the positions of the maxima of the spikes in the same time interval.

first found for this system [40] is shown in the next figure II.21. By performing a 2D Fourier transformation or, as we are presenting here, a Karhunen-Loéve decomposition [81, 82, 45] the fundamental components of this pattern become visible. In the spatial part of the pattern not only a single wave vector is present, but also one with half the wavelength can be found (see figure II.21c)). The same holds true for the temporal part, here a frequency and its sub-harmonic can be found (see figure II.21d)). Putting all these four components together we get the pattern shown in figure II.21a).

The reason for this behaviour is the interaction of the Hopf and the Turing instability. If we look at the eigenvalue spectrum corresponding to the pattern in figure II.22 we can see two bands of positive real parts of the eigenvalues. The band containing the smaller k-values consists of pairs of complex conjugated eigenvalues, while in the band for higher k-values the eigenvalues are purely real. The wavenumber of the Turing instability k_c is given by the maximum of the upper band. The wavenumber $k_c/2$ can be found in the lower band and is connected to a frequency $\omega_c/2$ which can be in resonance with the Hopf-frequency ω_c. It is obvious that this can only happen when both instabilities are present and have a similar strength. This is most probable at a point in phase

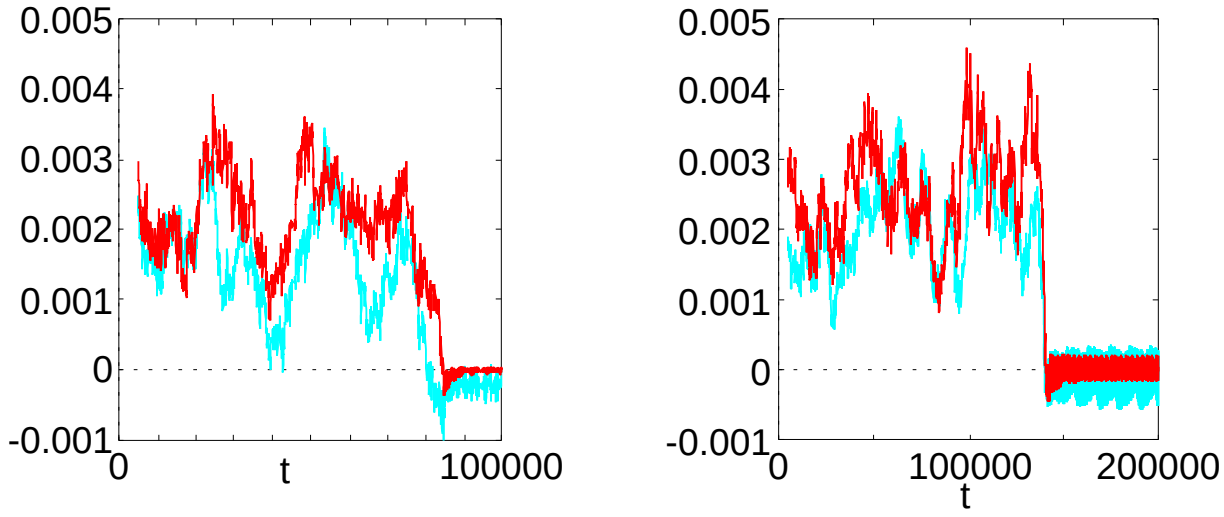

Figure II.19: The temporal evolution of the largest Lyapunov exponents for systems with size $L = 600$ and $L = 1200$.

space where the two instabilities arise simultaneously. This point is called codimension-two Turing-Hopf point. In general a point in phase space is called a codimension-two bifurcation when it is necessary to keep two parameters fixed to define this point.

One can ask now, if it is also possible to find patterns with only three or two of these components. A general answer to this question was given by Anne DeWit. In [83] she developed amplitude equations for the Brusselator model of the Belousov-Zhabotinskii reaction for a hierarchy of patters, starting from pure Hopf-oscillations and a pure Turing pattern. Not all possible patterns were found in the Brusselator equations which is similar to the model studied here. Besides the pattern described above we found interactions of one wave-vector and one frequency and a variety of bistable patterns. In the bistable patterns a Turing structure can be seen in one part of the domain and oscillations in another part of the domain. The oscillating part can be homogeneous or show some spiking behaviour. It is also possible to find more than two domains, e.g., a Turing pattern between two oscillating areas. If there are more than one spatially separated oscillating domains the frequencies need not to be the same.

To compare the different models a diagram where the characteristic timescale is plotted against the characteristic length scale was found to be useful. If we define a critical diffusion constant

$$D_c = \left[\sqrt{1+\frac{T}{\alpha}} - \sqrt{\frac{T}{\alpha}}\right]^{-2} \tag{II.33}$$

the codimension-two point can be found on the line $D/D_c = 1$.

The main differences between the semiconductor model studied above and the chemical one are on one hand the existence of two codimension-two points and on the other

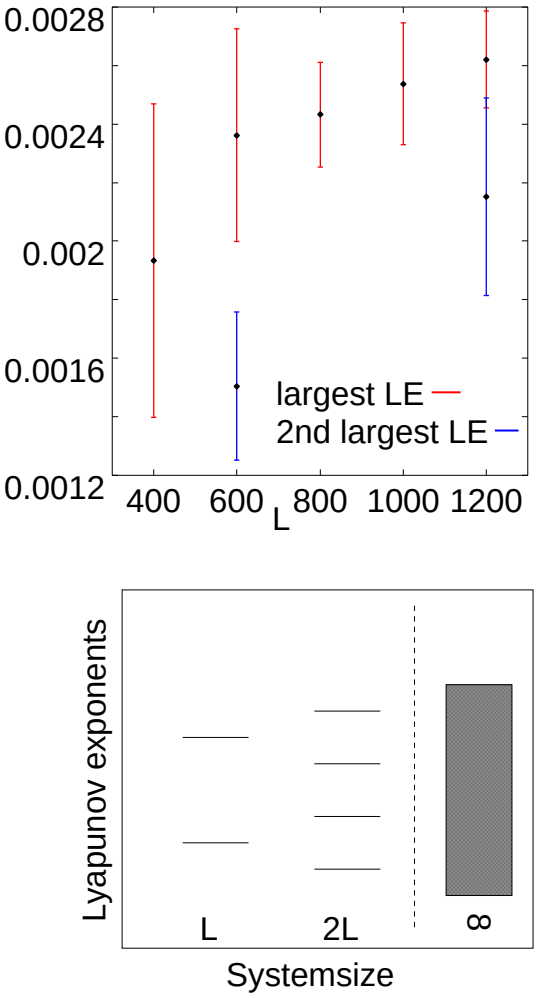

Figure II.20: Illustration of the increase of the number of positive Lyapunov exponents with the system size.

hand the very large discrepancy between the predicted critical values by the linear stability analysis and the actual values found in the non-linear system. Responsible for both is the special local kinetic function in the semiconductor model and the large amplitude patterns and oscillations which both cannot be described well by linear approximations.

Another model for the Belousov-Zhabotinskii reaction is the Oregonator model. This model has a codimension-two Turing-Hopf point, too, and shows similar patterns [84].

Now we want to extend our studies to the two dimensional case. Like in the case with global coupling the interface is now completely taken into account. It would be interesting to see if the catalogue of different patterns found in the 1-dimensional simulations have their corresponding structures in two dimensions.

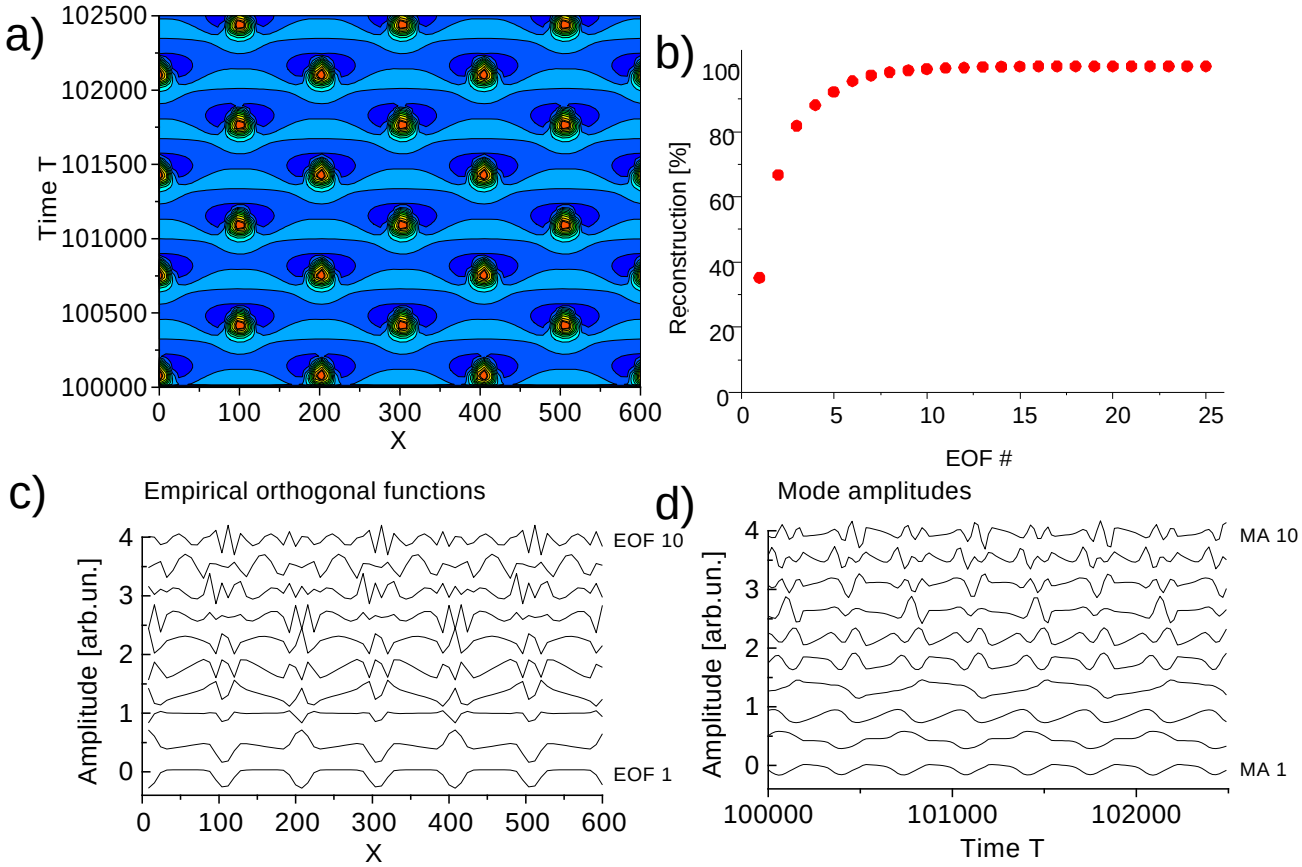

Figure II.21: A typical spiking pattern (a) of the system with local coupling with a Karhunen-Loéve decomposition. The relative importance of the different mode can be found in (b), (c) and (d) show the spatial structure of the mode and the temporal evolution, respectively.

II.3.2 The 2-dimensional system

For the 2-dimensional integration of the system we use the same numerics as for the 1-dimensional system.

II.3.3 Stationary patterns

The locally coupled system can show stationary patterns which we call (hot) current filaments, stripes and cold current filaments. Typical examples are shown in figure II.23

These three patterns can be seen as the analogues of the stationary patterns of (II.1) which will be illustrated in the following. If we take a value of j_0 slightly above the lower threshold, i.e. sending a small but over-critical current through the device, we can observe current filaments similar to the ones shown in figure II.23a). The diameter of these filaments will grow with increasing j_0. The amplitude of the filaments is more

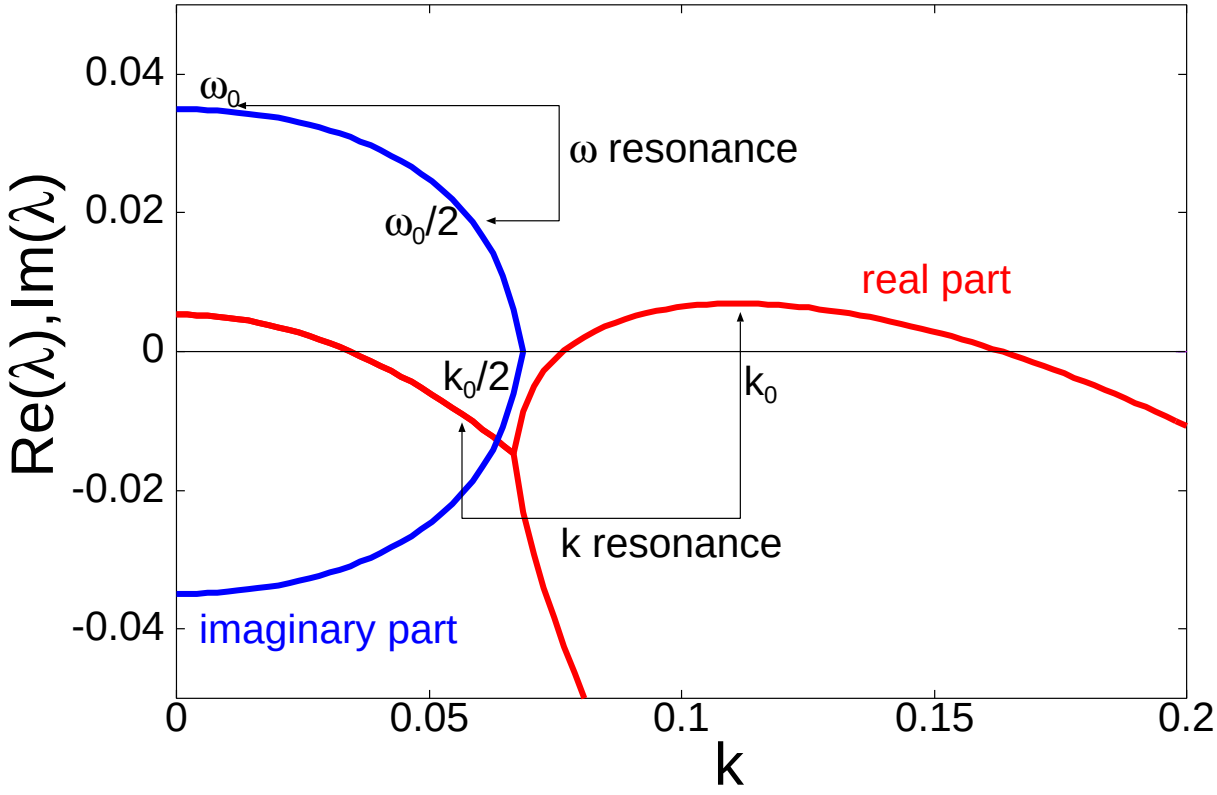

Figure II.22: A typical eigenvalue spectrum of a point in the parameter space where sub-harmonic resonances are possible. The k-value of the maximum in the Turing-band is marked with k_0 and also the resonant $k_0/2$ value which lies in the Hopf-band. Starting from this point the resonance of the frequencies ω_0 and $\omega_0/2$ is shown.

or less fixed due to the structure of the current-voltage characteristic and so the only way to put more current through the device (increasing j_0) is by enlarging the area of the filaments. At some point two filaments will touch each other and then start to form a stripe like structure. After further increasing of j_0 all circular filaments have vanished and a striped pattern can be found. This pattern is often also called "roll" pattern being reminiscent of, e.g. the roll patterns observed in the Raleigh-Bernard convection [6]. An increase of j_0 leads to an increase of the width of the stripes, because their amplitude is fixed for the same reason as the amplitude of the circular filaments. Eventually the stripes become so thick that they form a net like structure. Now we have areas of low current density embedded into a background of high current density, for this reason we call them cold current filaments. The whole process from current filaments to stripes to cold filaments is illustrated in figure II.24 where a sequence of images is shown each one with a different value of j_0. Figure II.25 shows the current voltage characteristic of the three filamentary structures, similar to figure II.7 and figure II.8 where the corresponding characteristic for the system with global coupling (II.1) is shown.

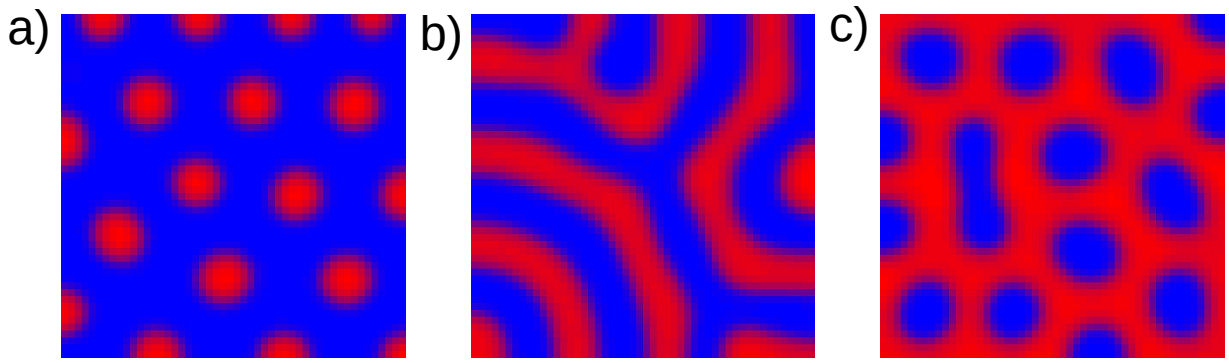

Figure II.23: Typical stationary patterns of the system with local coupling in 2 spatial dimensions. Hot current filaments are shown in a), stripes can be found in b) and in c) cold current filaments are shown. Parameters: $\alpha = 0.033$, $D = 8$, $L_x = L_y = 200$, a) $j_0 = 1.5$, b) $j_0 = 2.3$, c) $j_0 = 2.8$.

As in (II.1) three branches, corresponding to spots, stripes and cold spots are visible. A hysteresis between an increase and a decrease of the current can be found between spots and stripes and between stripes and cold spots. But here only bistability was found. Also the branches are very close to each other and a change from one pattern to the other is not as easily detectable as in small globally coupled systems.

All these analogies now lead to the following identifications. The hot corner filament in (II.1) corresponds to the (hot) spot structure in (II.2), the edge current layer corresponds to the stripe pattern and the cold corner filament is the equivalent to the cold spots.

II.3.4 Oscillatory pattern

So far we have found, apart from homogeneous oscillations and the homogeneous steady state, stationary Turing structures as discussed in the previous section. In the following section we try to find spatio-temporal structures corresponding to the ones found in two spatial dimensions for the globally coupled system (II.1).

Bistability between homogeneous oscillations and Turing structures

Near the boundary separating the area of homogeneous oscillations and stationary Turing structures in parameter space bistability between these two modes can be found. This boundary area is very small which can be seen in figure II.26 and usually it is easier to reach a bistable pattern with a certain symmetric initial condition than with random initial conditions. Similar to the bistable structures in one dimension there is no sharp boundary between the Turing and the Hopf area. If we look at a single spot in the system near the area of homogeneous oscillations a small oscillation of its amplitude can

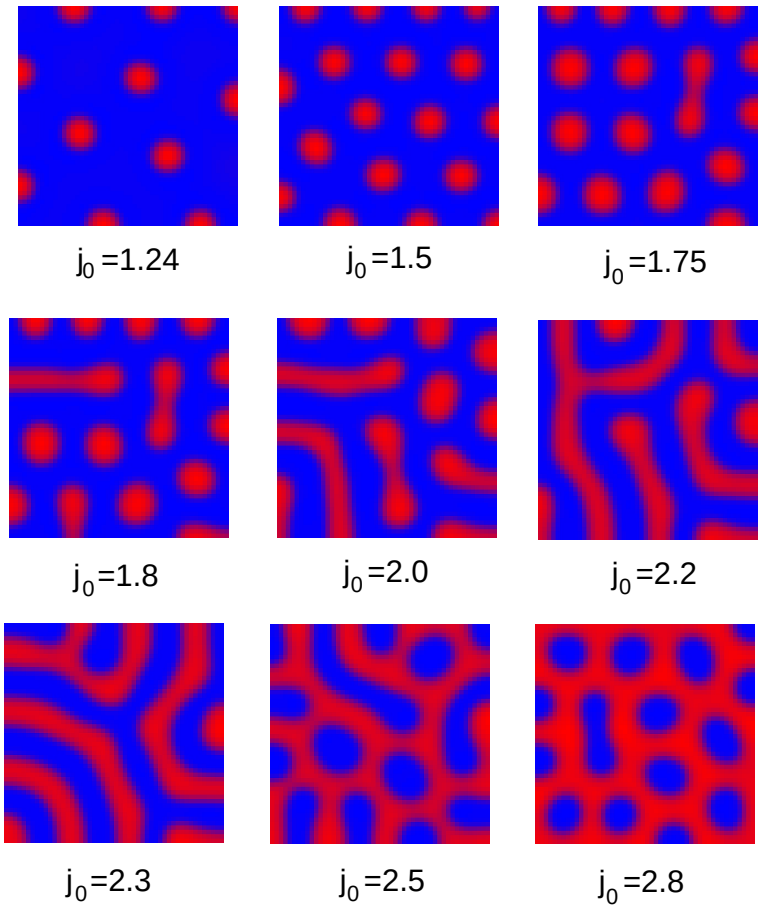

Figure II.24: The evolution of stationary patterns in the locally coupled system. Starting with current filaments for small values of j_0, stripes are formed for intermediate values of j_0 and for high values cold current filaments can be found.

be seen. On the other hand, near the area of Turing patterns the oscillations are not perfectly homogeneous, but have a small amplitude modulation of the corresponding Turing wave-length which decays fast with increasing distance from the Turing area. However this must not be mistaken for an interaction of the Turing and the Hopf mode which can be found in one dimension.

So far no oscillating patterns as a consequence of a Turing-Hopf interaction have been found, neither pure nor sub-harmonic. But the study presented here was a purely numerical study and as we have seen the area where bistability patterns can be found is already very small. Nevertheless it might be possible that in a tiny area in parameter space these interactions can be found. To answer the question whether such an area exists or not a first attempt with an amplitude-equation formalism similar to the one presented in [83] was made by W. Just, but so far there are no hints for stable oscillating patterns.

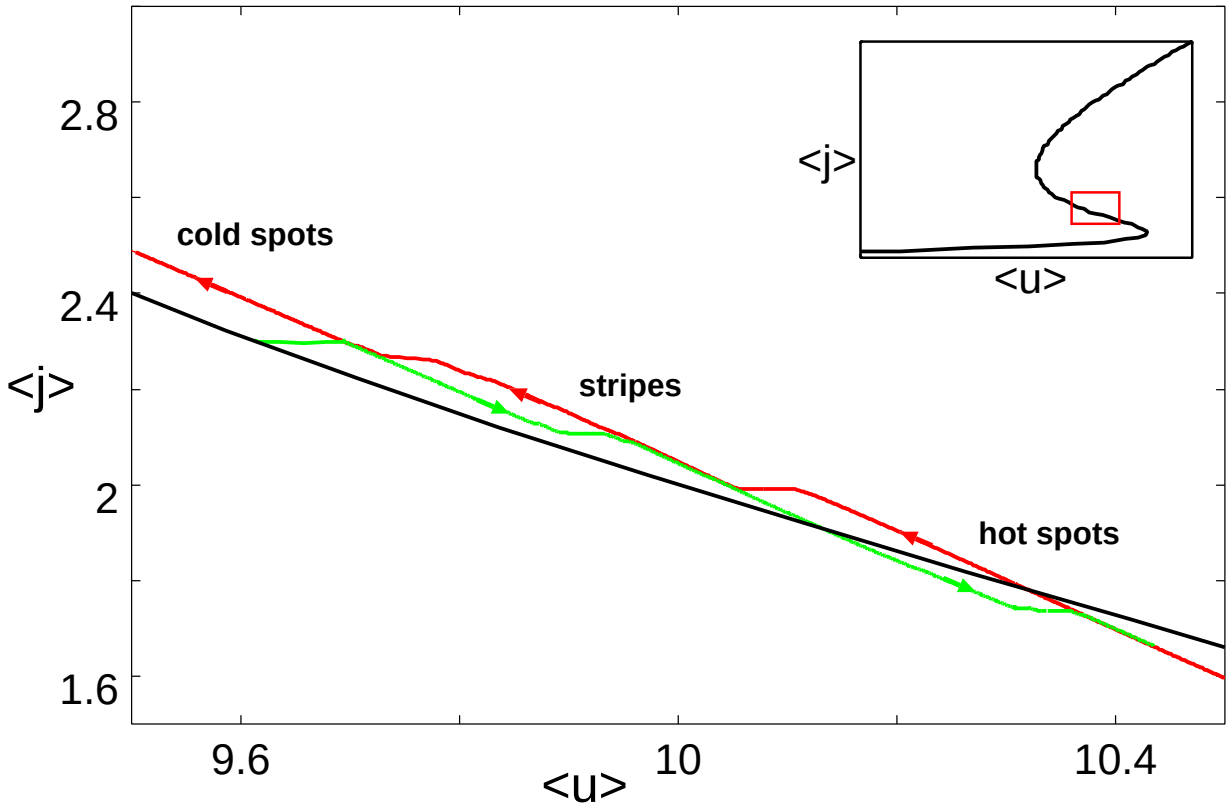

Figure II.25: The current voltage characteristic of hot current filaments, stripes and cold current filaments, respectively.

Spiral Waves

Until now we have mainly varied two parameters, namely α which represents the applied parallel capacitance and the control current density j_0. Or, in terms of nonlinear dynamics, the time scale (α) and the bifurcation (control) parameter (j_0). But, even if it is not obvious, we have also varied the ratio of the diffusion constants D. As we explained earlier the difference between the locally and the globally coupled system from a physical point of view is the degree of diffusion of the charge carriers in the contacts which are responsible for the voltage drop at the studied interface. The charge carriers can diffuse very much faster along the contacts than the carriers at the interface in the case of global coupling. In the model with local coupling a comparable diffusivity is assumed. This means that we have changed D a lot by going from a globally coupled system to a locally coupled one. We can go even further. If we assume that the contacts, i.e. the surrounding interfaces, are very badly prepared with respect to charge carrier diffusion and the modelled interface was prepared with great care it might be possible that the ratio of diffusion constants D becomes smaller than 1. This means that now the activator is faster than the inhibitor and this generally leads to spiral waves [85]. Figure

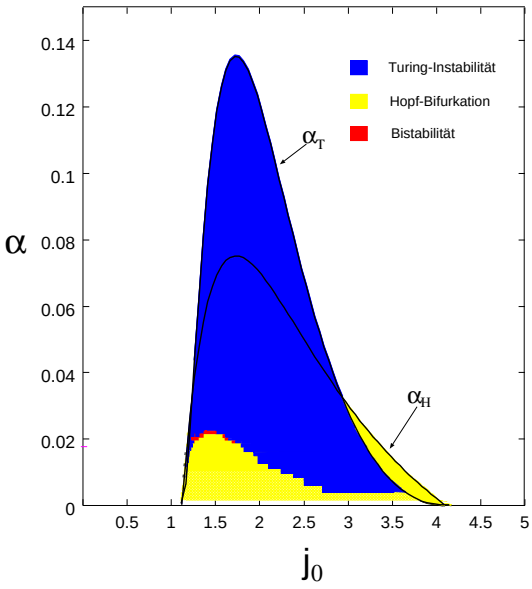

Figure II.26: Final states obtained by integrating the locally coupled system with random initial conditions in the j_0-α parameter plane.

II.27 shows a typical examples of a single spiral wave.

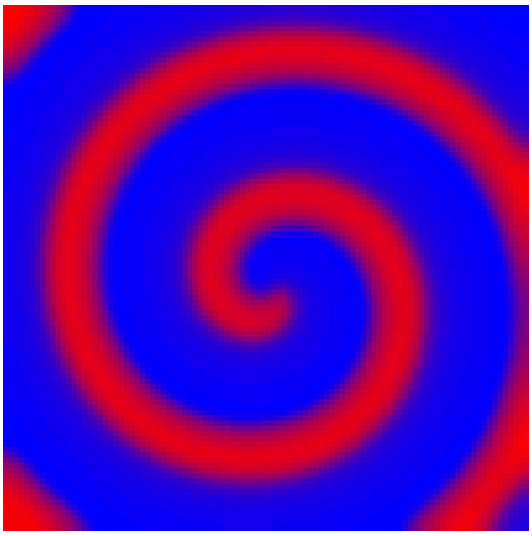

Figure II.27: A typical example of a single spiral wave. Parameters: $\alpha = 0.02$, $j_0 = 2.0$, $D = 0.2$, $L_x = L_y = 400$.

In larger systems with random initial conditions typically more than one spiral core arises, but after a transient time either a single spiral wave survives or two or more spiral cores are rotating in a way that all the cores can exist in the same domain. Both resulting states are periodic. No process was found which can generate new spiral cores like, e.g., spiral breakup [86, 87] and so it was not possible to find some chaotic motion like spiral defect chaos [88, 89, 90].

II.4 Summary

In this chapter we have discussed the spatio-temporal pattern formation in two reaction-diffusion models with two components. One is locally coupled and the other is the limit case where the diffusion of one species is infinitely fast. This is also called global coupling. Oscillations of a simple spatial structure can be found in the globally coupled system in one and two dimensions. The oscillations can be periodic or chaotic and the chaotic stage is reached via period-doubling or intermittency. The area where the oscillating modes can be found decreases with increasing system size.

The system with local coupling shows complex spatio-temporal patterns in one dimension but so far only bistability of an inhomogeneous stationary and a homogeneous oscillating mode have been found in a tiny area in parameter space. In the case of slow inhibition spiral waves can be found.

Both systems show three different kinds of stationary patterns which can be connected to different intervals of current density. The oscillating structures are always connected to the pattern with the lowest current density. Very similar patterns to the ones which we have called hot spots, stripes and cold spots, or hot corner filament, edge current layer and cold filament for the globally coupled case, have been found in a variety of other dynamical systems. For example in gas-discharge system current density filaments can be found [91, 92]. These filaments can form hexagonal patterns (hot spots) and stripes which were observed in experiments [93, 94] and in simulations [94]. A pattern corresponding to the cold spots has not been found so far, but this may be due experimental limitations. A similar transition from hexagons to stripes was found in the complex Ginzburg-Landau equation [89]. An analytic study of the three patterns based on normal forms can be found in [95]. Two-dimensional studies of the generalised Swift-Hohenberg model [96] which is an often used model for the CIMA reaction (Chlorite-Iodide-Malonic acid) where all three patterns were found are presented in [97, 98]. Also in the Brusselator model all three type of patterns can be found [99]. They found bistability between stripes and either hot or cold spots but no bistability between the different spot patterns or multistability between all three patterns which compares quite well with our findings. An important difference of the three previously mentioned studies and the one presented here are the amplitudes of the patterns. In these works low amplitude (super critical) patterns where studied with generalised equations which are valid near a bifurcation point, but in our work large amplitude patterns were studied, which is typical for semiconductor models [100, 101, 102, 48]. Also the nonpolynomial local kinetic function is typical for this kind of semiconductor models [101, 100] in contrast to the cubic polynomial used in [94].

Dynamical systems like chemical reactions and gas-discharge tubes have the advantage that the evolving patterns can easily be seen and measured. Semiconductor interfaces are generally embedded between a number of other semiconductor layers and metal contacts so that in general it is not possible to get spatially resolved experimental

data of the whole interface. Another obstacle is the small size of semiconductor devices, e.g., a couple of μm in the case of the HHED [51]. But in special cases it is possible to measure, e.g., the spatial structure of the surface potential [54] which is connected to the local current density or to record recombination radiation with a high-sensitivity near infrared video camera [52]. But these experiments so far have only produced one dimensional data, which are in good agreement to the one dimensional results of our simulations but can give no further insight to the current density distribution over the whole interface. However it might not always be necessary to really measure the spatially resolved current density distribution, because the simulation show that many patterns have a specific fingerprint in a current-voltage diagram or in the time evolution of the applied voltage. If we compare, e.g., figure II.13 and figure II.14 we can see that the spiking mode, the breathing mode and homogeneous oscillation have a different temporal behaviour which makes it possible to distinguish between these three modes. The three types of stationary patterns can be identified with the help of the current-voltage characteristic. As shown in figure II.7, II.8 and II.25 each of the patterns has its own branch in the current-voltage characteristic and by looking for a hysteresis these branches can be found. If we compare figure II.7 and II.8 we can see that it might be easier to identify the different branches in small systems, because in large systems they are lying very close to each other.

This system is another good example to show that it is very desirable to have both good experiments and a good theory to obtain a detailed picture of a physical system. Because it is not always possible to measure every single quantity of a physical system a theoretical model which is in agreement with the experimental data is necessary to obtain more information of the internal processes and the connection of the relevant quantities.

III: Pattern formation in epitaxial growth of quantum dots

In this section we would like to present another system showing pattern formation. While in the previous chapter we considered electronic transport through an interface we will now study atoms deposited on a semiconductor surface. In both cases particles will accumulate at the obstacle and may then be able to form some patterns. The study of the epitaxial growth on semiconductor surfaces is of great technological importance, because of the strong needs in the computer industry for semiconductor materials with very well defined structural and chemical properties.

In general a simple picture of semiconductor growth looks like the following. Atoms will ”rain” onto the surface and can then move over the surface under the influence of the periodic surface potential and of the other atoms on this surface. The ad-atoms can stick to each other and form clusters (islands) on the surface. There are three main growth modes on semiconductor surfaces which we will explain in the next section, but only in one we will find pattern formation processes which can be compared to the system of the previous chapter, because only in this growth mode we will find an inhibiting mechanism which will influence the clustering of atoms.

III.1 Growth Modes

The growth on semiconductor surfaces is classified by three main growth modes, namely the layer-by-layer or *Frank – van der Merwe* growth [103], the island or *Volmer – Weber* growth [104] and a mode for highly strained systems called *Stranski-Krastanov* growth mode [26]. In figure III.1 all three modes are illustrated.

The layer-by-layer mode (figure III.1a)) is characterised by the fact that during growth the surface is quite flat and occurring steps are very low. Ad-atoms will only start to form larger clusters on a layer when this is almost completed.

This is in contrast to the processes being observed in the island growth mode (Volmer-Weber) (figure III.1b)) where ad-atoms will already cluster on layers which are far from

complete and thereby forming three dimensional island structures. These two modes can be observed in the same material system with different external parameters. Under high temperature and only a small ad-atom flux to the surface the ad-atoms can diffuse fast and far to find an edge of the growing layer where they will be bound to two or more atoms reducing their own energy. On the other hand with low temperatures and a high flux ad-atoms will only find smaller clusters and stay there.

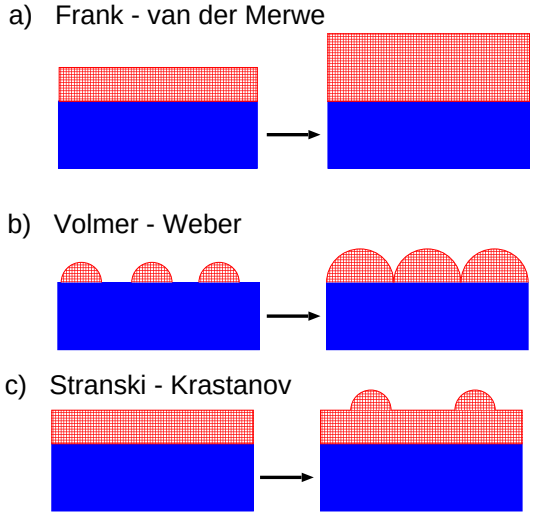

Figure III.1: The three different growth modes in epitaxial growth. a) the layer-by-layer or Frank – van der Merwe growth mode, b) the island or Volmer – Weber growth mode and c) the Stranski – Krastanov growth mode.

For the third growth mode (Stranski – Krastanov) (figure III.1c)) we have to take a closer look at the surface. When impinging onto a surface an ad-atom will find the already existing lattice of the substrate with a fixed lattice constant. In homo-epitaxy where substrate and ad-atoms are of the same material, there will be no problem. New clusters will just have the same lattice constant and will therefore fit perfectly to the substrate. The problem arises with hetero-epitaxy, where substrate and ad-atoms are of different material. Both materials will have their own lattice constant and when growing one onto the other they have to adjust in some way. Independently of how this happens we will have a strained system, since at the beginning the ad-atom clusters will form in a way ensuring that they have the same lattice constant as the substrate. But not only the ad-atoms will feel the strain, the substrate atoms also will be shifted from their equilibrium positions. The displacement will not be as strong as in the ad-atom cluster but the larger the cluster becomes the stronger the influence on the substrate will be. One way to relax the accumulated strain energy is by forming dislocations. Here the ad-atoms will not form a regular periodic lattice, but the lattice will have vacancies or other defects. The consequences are poorer material properties of the ad-atom layer. For this reason one wishes to avoid dislocations. One possible way to do this is by using the Stranski-Krastanov growth mode.

During the Stranski-Krastanov mode two stages are observable. First a few monolayers grow epitactically on the substrate and are, as explained above, heavily strained. These layers are called wetting-layers. To relax the strain small, dislocation free islands

can form on top of the wetting layer. Under certain growth condition these islands show a surprising behaviour. They have a sharp size distribution, i.e. they all have about the same size. Furthermore a spatial ordering of the islands on a square lattice is observable (see [33, 105] for experiments showing these results). On account of their size, which is so small that they have only a few, or even only one localised eigenstate for electrons or holes, they are called quantum dots. They are often also labelled self-organised quantum dots to separate them from the quantum dots fabricated by photo-lithography or on pre-patterned surfaces.

The self-organised growth of quantum dots in strained semiconductor systems has recently become the focus of extensive research because of its great potential of application to nanoelectronic devices. It might help to simplify the fabrication of novel semiconductor devices based on quantum dots, for instance, quantum dot lasers with better gain and lower threshold than conventional quantum well lasers [106, 107, 108]. It is widely accepted that the key to the understanding of this growth lies in the strain fields which are present in the Stranski-Krastanov growth mode. The strain induced by the quantum dots in the substrate is of great importance for the ordering. For a recent review on experimental and theoretical results see [109].

There is another effect of self ordering processes, namely the shape of the quantum dots. This will not be under consideration here because of the different nature of this problem. There are theoretical studies of the thermodynamic equilibrium shape of InAs quantum dots on a GaAs(100) substrate using density functional total energy calculations which show that there exist different possible volume dependent shapes for quantum dots which are not overgrown [110, 111]. In devices the quantum dots will be overgrown by substrate material and it is highly possible that their shape will be different then. For example in [112] cross-sectional scanning-tunnelling microscopy (STM) images stacked InAs quantum dots are shown which are quite flat, i.e. their height is small compared to their diameter. The actual shape will also depend sensitively on the material, while here we will focus on methods to describe the positional and size ordering effects independently of the specific material parameters. This will imply that our calculations are only valid for the formation of the first few monolayers of the islands. However, this is in agreement with the view that the most important processes for positional and size ordering effects will happen during this early stage of growth. As explained in [113], platelets of one monolayer will form the fundaments for the quantum dots.

In the following we shall develop a kinetic Monte Carlo model to describe the positional and size ordering of self-organised quantum dots.

III.2 Kinetic Monte Carlo Formalism

The idea behind the kinetic Monte Carlo simulation is to describe the diffusive motion of atoms on a surface considering the periodic atomic potential of the surface and other atoms adsorbed on the surface. Each atom can move from its actual position to another lattice site, hereby influencing other atoms on the surface. Here we restrict ourselves to nearest neighbour hopping and nearest-neighbour interactions. Additionally no vacancies are allowed and an atom can move only on top of another atom. This is called solid-on-solid or SOS model. Hence each atom has a certain probability p per unit time to move from its position to a specific neighbouring site. This probability is proportional to an Arrhenius factor

$$p = \nu \exp(-\frac{E_s + nE_n}{k_B T}) \tag{III.1}$$

where E_s is the atomic binding energy to the surface and E_n is the binding energy to a single nearest-neighbour atom, n gives the number of nearest-neighbours, T is the temperature and k_B Boltzmann's constant. The proportionality constant is a vibration or attempt frequency ν which we take as $10^{13} s^{-1}$ [114]. To choose the target nearest-neighbour position we have to consider several cases. For a free atom with no neighbours and not near a step edge we assign the same probability to all nearest-neighbour sites. If the atom is at the top of a step we have to take into account the Schwöbel barrier, which we will discuss in more detail in section III.3.4, for going down the step. At the bottom of a step apart from the Schwöbel barrier we have to take into account that atoms may prefer to move along the step rather than separating from the step. This process is responsible for a straight island boundary. There may also be much more complicated processes, for example, the diffusion on a flat surface may be anisotropic or as shown in [37] for the diffusion on GaAs(001) complicated long range diffusion steps have to be included. But here we stick to this simple model in order to be independent of a specific material. For a free atom on a flat surface, i.e. where the hopping probability only depends on E_s, the diffusion constant D is given by

$$D = \frac{a_0^2}{4} p \tag{III.2}$$

where a_0 is the length of a nearest neighbour hop [115].

So far equation (III.1) does not include any strain effects. In strained systems the equilibrium position and also the equilibrium binding energy of the atoms will be modified. The binding energy in strained systems will in general be lower than in the unstrained case. This can easily be seen in the interaction potential of a system with two atoms as shown in figure III.2. This potential has a minimum which defines the equilibrium distance of the atoms. The energy which is gained compared to the state where the atoms are infinitely far apart is called binding energy. Moving the atoms closer together or further apart will reduce the binding energy. In section III.3 we will discuss a strained semiconductor layer in more detail.

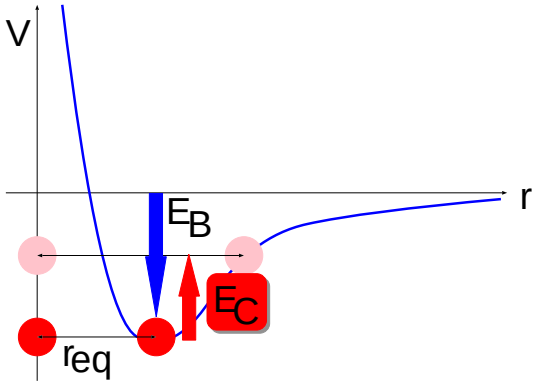

Figure III.2: Interaction potential of two atoms. The minimum of the potential defines the equilibrium distance and the equilibrium binding energy.

To include this effect we introduce a correction term $E_c(x, y)$ for the binding energies E_s and E_n. $E_c(x, y)$ may be different at each atomic position (x, y) on the substrate surface, because of the non-homogeneous strain field. The resulting hopping probability is

$$p = \nu \exp(-\frac{E_s + nE_n + E_c(x, y)}{k_B T}). \tag{III.3}$$

In this context $E_c(x, y)$ is always negative to reduce the binding energy and to increase the hopping probability. The higher the strain the more negative is $E_c(x, y)$. As a result atoms will move faster in areas with higher strain and slower in areas with lower strain and this will lead to a flux of atoms from high-strain to low-strain regions. In section III.3 we will describe how we calculate $E_c(x, y)$.

With this we now have all the ingredients for the single atom hopping probability. We would like to stress that the modelling of $E_c(x, y)$ at this stage is purely phenomenological. While the values of the parameters E_s and E_n were also used in other theoretical studies, as mentioned above, which included quantitative comparisons with experiments, the strain field is introduced here for the first time, and no direct comparison with experiments is available for the values of $E_c(x, y)$. For a microscopically founded, quantitative expression extensive detailed ab-initio calculations would be necessary in order to investigate how the strain affects the binding energies. Such microscopic calculations can, however, not be performed for the large systems considered here, which are required for pattern formation. But there is another obstacle for the estimation of the energy values. In the Monte Carlo scheme on the mesoscopic level described here, we use only a single species of atoms. In III-V compound systems, which are the most widely used material systems in experiments, two species, namely the cations and the anions, diffuse. To include these systems a single step in the Monte Carlo scheme must not be seen as a jump of a single atom to a neighbouring position, but as a mean or effective process which represents the motion of more than one atom in the experimental system. Accordingly the energy values used in the Monte Carlo simulation are effective ones and cannot easily be compared to single values found by ab-initio calculations. A Monte Carlo scheme for III-V compounds with two different types of atoms is, e.g.

presented in [116].

Now we can describe the Monte Carlo algorithm step by step. In the first step the hopping probabilities p for all atoms on the surface are calculated. For the binding energies we use $E_s = 1.3$ eV and $E_n = 0.3$ eV which corresponds to values employed in Monte Carlo simulations for Si on Si(001) surfaces [114]. The number of neighbours of each atom n has to be determined. Atoms with four nearest neighbours are considered as immobile. Now we have to find all islands on the surface and calculate $E_c(x, y)$ as described in III.3. The hopping probability is then given by (III.3).

In the next step of the Monte Carlo simulation we group the possible hopping events of all atoms into classes with equal probability, or more precisely, within a certain probability interval $[p_i, p_i + \Delta p]$ as illustrated in the upper part of figure III.3. This is necessary, because of the continuous contribution of the strain field $E_c(x, y)$. We collect all hopping events which fall into a specific class i and weight the probability p_i with the number of events N_i in that class. Besides the surface diffusion, the deposition of an atom (due to molecular beam epitaxy or metal-organic chemical vapour deposition) also represents a possible event, and is also assigned a probability per unit time according to the deposition rate. Then we randomly choose one of those probability intervals according to its weighted probability $p_i \cdot N_i$, such that intervals i with a higher weight are preferred. This is shown in the middle part of figure III.3. An event is selected randomly out of the chosen interval (see lower part of figure III.3) and the selected atom moves to the selected nearest-neighbour position.

The probabilities for the atoms around the moving atom's initial and final position are re-calculated and then a new probability interval is selected. The strain field corrections $e_c(x, y)$ are not updated at every single Monte Carlo step, because the islands change on a much slower time scale. For this reason we re-calculate the corrections only after every 1000 hopping events. Small-scale tests with an update after every 100 events have shown no qualitative change and we assume that the update rate might be taken even less than $1/1000$.

With this event-based scheme the time interval associated with a single event may differ from event to event, depending on the other possible events. If the rates per second of all possible events are summed up the inverse of the sum is the time step which has to be associated with the chosen event.

III.3 A strained semiconductor surface

In this section we want to discuss how it is possible to incorporate strain effects into the Monte Carlo formalism. In the previous section a correction term $E_c(x, y)$ to the local binding energies was introduced. Now the question arises how this term is connected to the strain field. To outline the answer to this question we take the following steps. First we discuss two ways to calculate the strain field. Second we review some

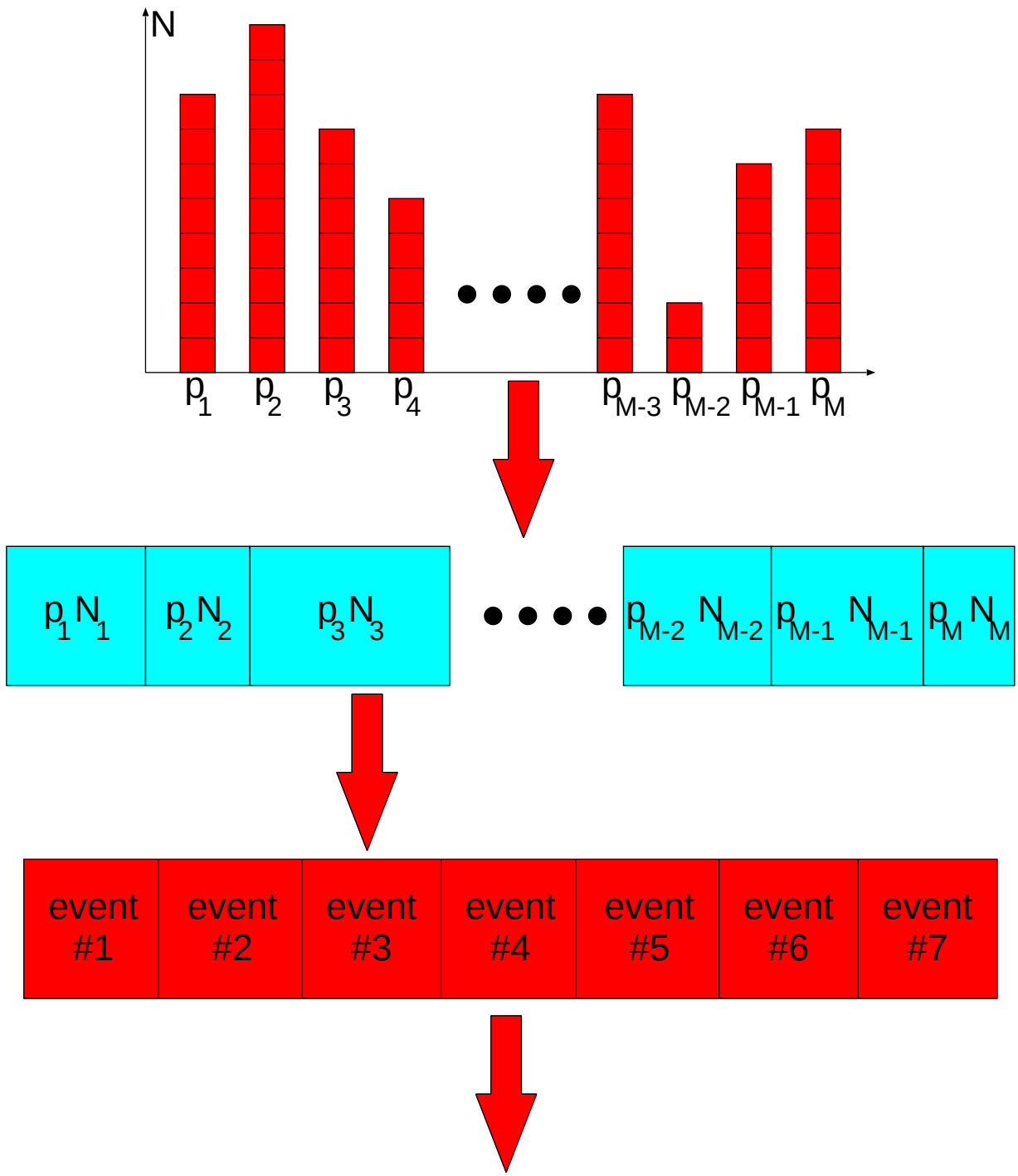

Figure III.3: Illustration of the Monte Carlo process. The probability of all events are calculated and are then grouped into several intervals. The probability of the intervals are weighted with the number of elements inside the interval and out of the total interval a part is chosen randomly. A single event of the chosen interval is selected randomly.

ways to calculate the effects of strain on binding energies. Finally we present a simple phenomenological approach which is used in the Monte Carlo simulations presented here.

III.3.1 Calculation of the strain field

There are two ways to calculate the strain around an island on a strained wetting layer. The first is the theory of elasticity [117] which was used by Shchukin et al. [118] to determine the free energy of quantum dots. The elastic energy was also used in [119, 120]. In [121] a method based on a Green's function formalism is presented to calculate the components of the stress tensor for an isotropic medium. Shchukin has developed an extension for anisotropic media and Meixner has substituted the phenomenological correction term E_c by this approach in the Monte Carlo scheme [122, 123] to start more realistic calculations. With the help of finite-element calculations the strain field for specific quantum dot geometries was calculated in [111, 124]. The second method to calculate the strain field is the valence force field method [125] and its simplified version introduced by Keating [126]. Although this method would describe the quantum dot system microscopically in more detail than the theory of elasticity, because it takes into account that quantum dots and the surrounding substrate are formed by atoms in a fixed lattice, it is rarely used [127] in the theory of quantum dots.

III.3.2 The influence of the strain field on the binding energies

Schroeder et al. [128, 129] studied the effects of strain on binding energies with the help of molecular dynamic calculations. They discussed the (001) surfaces of the three standard lattices, namely the simple cubic, the face centred cubic and the body centred cubic.

An approach similar to ours was done by Ratsch et al. [130, 131]. They used the Frenkel-Kontorova model [132] to calculate the average strain energy per atom. This energy is then used as a correction to the hopping barrier for an atom in a kinetic Monte Carlo scheme.

III.3.3 Phenomenological correction term $E_c(x, y)$

To obtain the effects of a strain field in general one has to use a number of sophisticated techniques as shown in the previous sections [122, 133], but here for simplicity and generality we will employ some phenomenological functions to mimic the strain fields and $E_c(x, y)$. Close to existing islands (quantum dots) the strain is very high and it decays fast with increasing distance from the island. Therefore we model the strain of a single island by a function centred around the centre of mass of the island which decays

to zero at some distance from the island. The amplitude of this function and the domain where it is non-zero increases with the size of the island. In the core of the island this function is of no interest, because we assume that the atoms there cannot move.

To incorporate the correction $E_c(x, y)$ due to the strain field we take all islands with a minimum size (in the simulations we use, e.g., islands with a least $N = 10$ atoms), and set the range of the strain field around those islands equal to twice their radius. In this range $|E_c(x, y)|$ (note that $E_c(x, y)$ is negative) is assumed to decrease linearly from its maximum value at the centre of mass of the island down to zero at the edge of the range of the strain field. The maximum value $|E_c^{max}| = \alpha N$ is assumed to scale linearly with the number of atoms N in the dot where $\alpha = 0.01eV$. To take account of the cubic lattice symmetry we use the maximum norm $||\mathbf{r}||_\infty = \max\{|x|, |y|\}$ for surface vectors $\mathbf{r}$ to calculate distances. When the ranges of two islands overlap we add up the different contributions to the strain field. Having calculated the contributions of all islands we make sure that $|E_c(x, y)|$ is not larger than a cut-off value which we choose as 0.3 eV.

III.3.4 Why do we need a Schwöbel Barrier?

Besides the simple approach where only the binding energies of the nearest neighbour atoms are taken into account we also want to include an effect called "Schwöbel Barrier" [134, 135]. This barrier is characterised by an extra energy which an atom has to surmount when crossing a step of atoms, i.e. when moving on top of another atom or falling down from an atom.

The reason for this extra energy is the asymmetry at the step edge. When, for example, an atom from an upper terrace comes to a step edge the binding energies from the atom layer below is not equal in all directions, because there are no atoms beyond the step edge. As a result the atoms of the higher terrace prevent the ad atom from falling down the step. Including this energy the probability for staying on the terrace is higher than for falling down. On the other hand it is also more probable for an atom to stay on a lower terrace than jumping up a step. This is illustrated in the following figure III.4

To incorporate the Schwöbel barrier into the Monte Carlo scheme it is now necessary to consider every possible move of an atom as a single event with an own probability. The strain will reduce the binding energy of all atoms at the boundary of an island. This means that these atoms will have a higher probability to move, but no direction is distinguished. An atom can move away from the island and up to the next level of the island with the same probability which is not realistic. To control this upward flow we introduce an extra energy of 0.1 eV for a move one level up. With an extra energy for moves one level down it would be possible to control the formation of higher layers of the island. The higher the barrier for moves down the earlier a new layer will nucleate on another. Here we always use a Schwöbel barrier for downward flows of 0.1 eV.

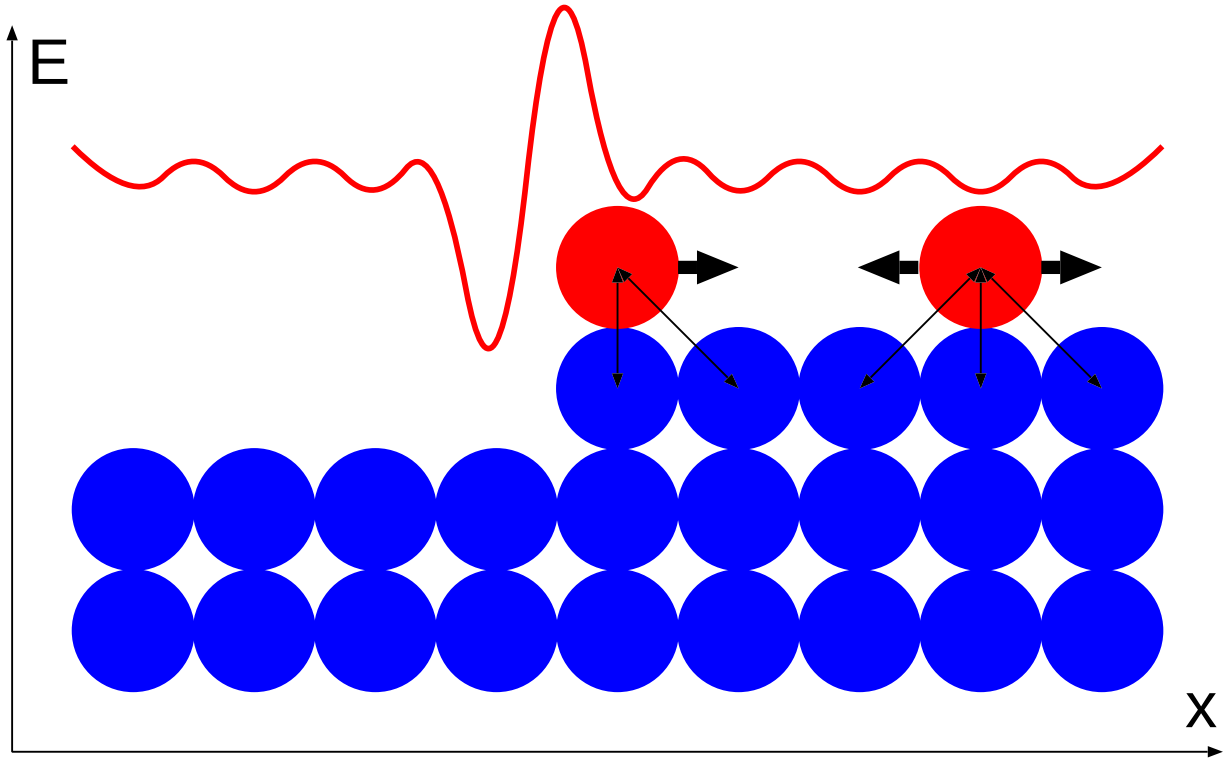

Figure III.4: Illustration of the Schwöbel Barrier. An atom at a step edge will experience an extra force because of the asymmetry of the surrounding.

III.4 Results of the Monte Carlo simulations

III.4.1 Co-operative growth versus Ostwald ripening

When comparing the effects of equation (III.1) and (III.3) an important new effect is visible. Fig. III.5 shows a simple test where we have put a large and a small island onto the surface as initial conditions. For the fixed number of atoms, their surface diffusion is now modelled by a kinetic Monte Carlo simulation. Equation (III.1), which does not include strain effects, leads to Ostwald ripening, i.e., a winner-takes-all dynamics where the smaller island decays and only the large one grows and finally survives (Fig. III.5a). This can be explained by means of the following. The larger island has a larger boundary where free atoms can connect and hence there is a higher probability for a free atom to connect to the larger island than to the smaller. On the other hand also more atoms will desorb from the larger island, but this occurs much more rarely than the inverse process because of the binding energies to the other atoms of the islands which reduce the desorption probability drastically. All this results in a net flux of atoms to the larger

island.

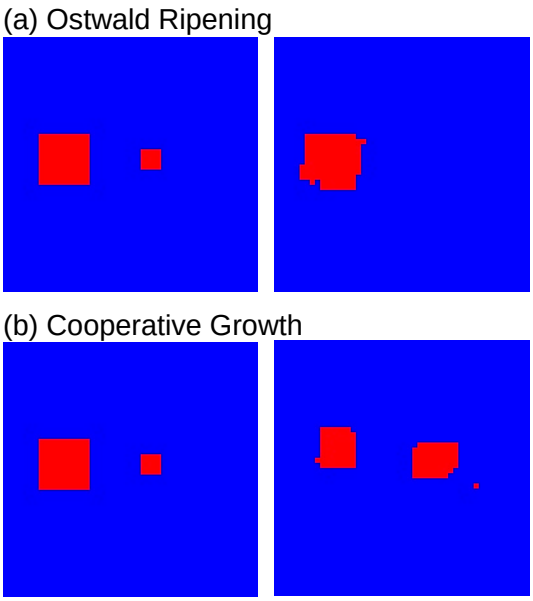

Figure III.5: Cooperative growth and Ostwald ripening. For figure a) only the standard Monte Carlo model (III.1) was used while for b) equation (III.3) which include strain effects was used. The initial configuration (left) and the pattern after 10s (right) are shown.

In contrast, using equation (III.3), which includes the effects of strain, we obtain a kind of co-operative growth where larger islands lose some atoms to smaller ones (Fig. III.5b). Because of the higher strain at its boundary, hopping away from the larger island is favoured compared to the smaller one until both have about the same size. This is necessary for the formation of a large number of equally sized quantum dots and gives a first hint that we can expect size ordering [136].

III.4.2 Continuous deposition

In contrast to section III.4.1 we will now study a system where a continuous flux of atoms onto the surface is present.

With this feature one can observe the formation of single quantum dots which is shown in figure III.6. At the first stage a single quantum dot starts to grow in the first monolayer (shown in red) until the increasing strain at its boundary makes it more favourable for the free atoms to form a second quantum dot, and so forth. When the density of the quantum dots is so large that the strain fields of different quantum dots start to overlap a slight motion of the quantum dots' centres of mass is visible. After a while the islands do not grow any more in the first monolayer but new atoms move to the second layer (green) to form three-dimensional quantum dots. If we put even more atoms onto the surface the single islands start to collide and form larger islands. At this point the development of a sharp size distribution and the regular arrangement is spoiled. We can see here that we have to stop the flux of atoms at a certain coverage to achieve an optimal array of quantum dots which we will discuss in more detail in

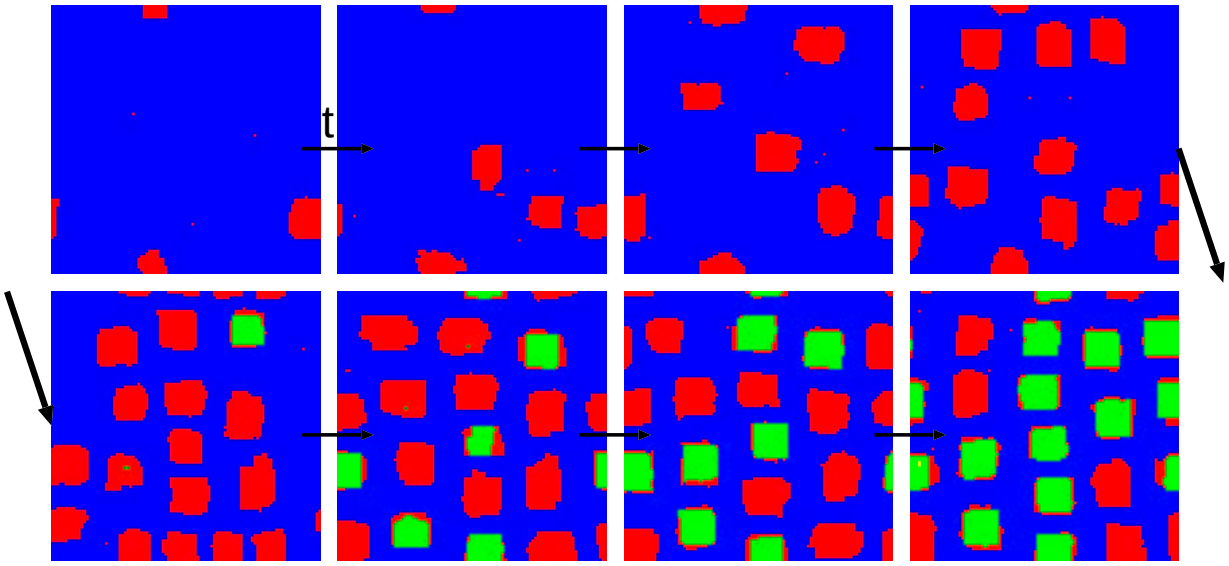

Figure III.6: The formation of quantum dots on a flat surface. The blue shaded area represents the substrate. Ad-atoms in the first and second layer are red and green, respectively. The simulation was performed on a 200×200 grid at 750 K.

section III.4.4. The reason why we ought to stop the simulation here is, that so far we did neither model the strain on top of the islands themselves nor the transition of atoms across island edges in an appropriate way. So the simulation is only valid for the first monolayer and starts to fail when atoms populate the higher layers in larger numbers.

Next we want to compare the dot patterns which can be found for different growth conditions and discuss the optimization of self-assembled quantum dot structures. For that we need some tools for quantitative comparison which will be presented in the following section.

III.4.3 Analysis of the quantum dot patterns

It is necessary to have a quantitative means to analyse and compare patterns formed by quantum dots. Quite obviously the size distribution can be plotted by a distribution function. The size (area) of an island is proportional to the number of atoms forming this island, but here a problem arises. During the simulation atoms will attach and detach constantly from the islands and at a specific time step it might be possible that all islands have about the same size, but no two islands will have exactly the same size. This leads to the question how to group the islands in a sensible way. The natural shape, due to the symmetry of the lattice and the strain field, for an island is a square. Therefore we count every island which has about as many atoms as the nearest perfect square island in the same group. The easiest way to do this is by taking the square-root of the number of atoms, rounding it up or down to the nearest integer and plotting the distribution as

a function of this "effective" diameter d.

To see how regular a single pattern is, it is often the best way just to look at it. But on the other hand the eye can be tricked or misled so that we also need a more quantitative way to analyse a single pattern and even more so to compare two different patterns. Because our aim is to find very regular patterns a spatial Fourier transform, which can detect dominant wave vectors, is a good tool for this analysis. A subroutine based on the "Fast Fourier Transform" (FFT) algorithm [137] is used here. For the FFT it is necessary that the number of rows and columns is a power of 2. To fulfil this requirement we expand the input data periodically until the next power of 2 is reached. This may lead to some artifacts, because although the original pattern is periodic the expanded is not periodic. But with a system which is large enough to hold a couple of islands in one direction this is negligible.

To demonstrate what results we should expect the Fourier transformation of two test patterns is shown in the following figure III.7. Figure III.7(a) shows a pattern with square symmetry generated by

$$f(x,y) = \mathrm{sgn}(\sin(x) + \sin(y) - 1.0), \tag{III.4}$$

where x and y label the two spatial dimensions, and the corresponding Fourier transformation. The four-fold symmetry of wavevectors $k_x = \pm 1$, $k_y = \pm 1$ is clearly visible in the transform. A pattern with hexagonal symmetry generated by

$$f(x,y) = \mathrm{sgn}(\cos(\sqrt{3}y - x) + \cos(\sqrt{3}y + x) + \cos(2 * x)) \tag{III.5}$$

and its Fourier transform is shown in figure III.7(b). Here a six-fold symmetry of wavevectors $k_x = \pm 1$ and $(k_x, k_y) = (\pm 1, \pm 1)$ can be found.

The symmetry of the patterns is clearly visible in the density plot, but it is still difficult to compare the Fourier transformation of two different patterns or two peaks in one Fourier transformation quantitatively. To do this, we use one dimensional cuts across the two dimensional domain of the Fourier data as shown in figure III.8.

Besides the characterization of the patterns the Fourier transform also gives the possibility to compare the Monte Carlo results to x-ray scattering images [138], because the resulting images are more or less a Fourier transform of the surface.

We will use the size distribution and the Fourier spectrum only to analyse the surface structure at given times. To get an impression about the temporal evolution of the surface structure we will plot the total number of islands on the surface and the surface roughness r over time. The number of islands is proportional to the island density, because we will use always the same domain. The surface roughness r, the standard deviation of the height h, is given by

$$r = \frac{1}{N}\sqrt{\sum_{x,y}(h(x,y) - \overline{h})^2}, \tag{III.6}$$

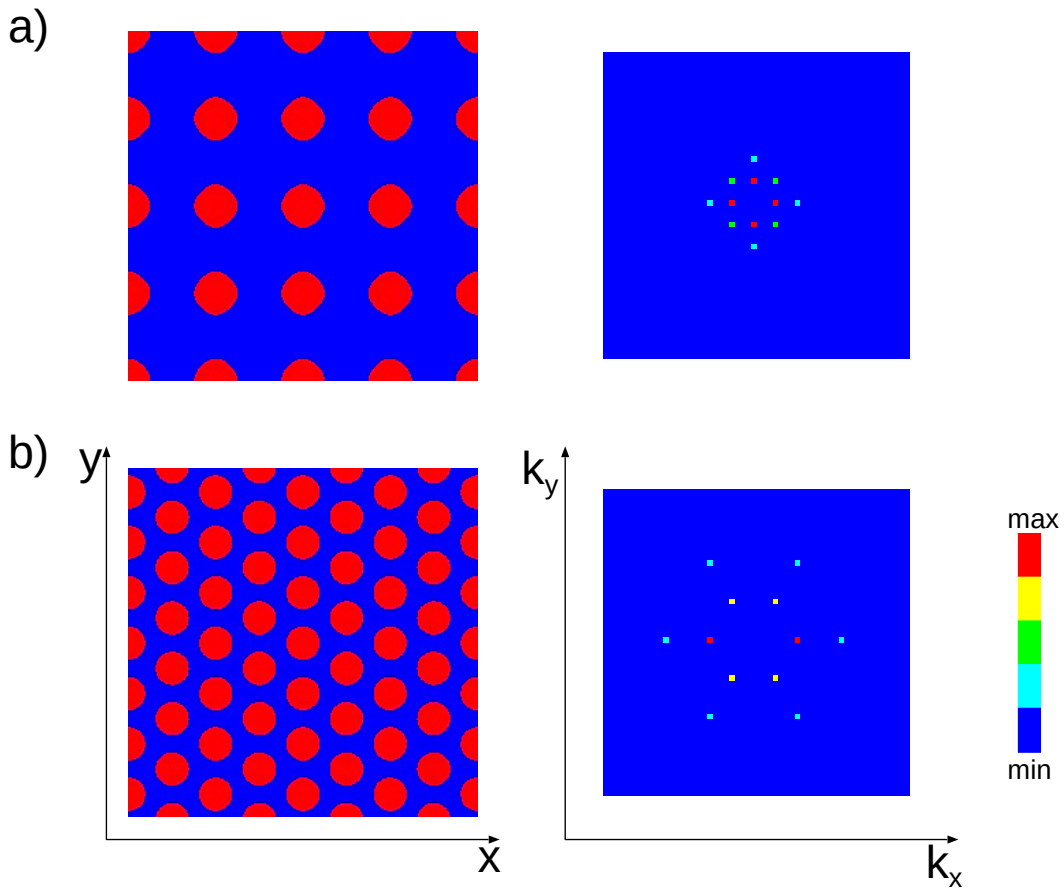

Figure III.7: Demonstration of the spatial Fourier transform. In (a) a square pattern and its Fourier transform is shown in (b) a hexagonal pattern with its corresponding transform can be found. In the left column the spatial structure in real space (x and y coordinates) is show while the corresponding Fourier transform in k-space (k_x and k_y coordinates) can be found in the right column.

where x and y are labelling the grid points of the simulation lattice, N is the total number of grid points, $h(x, y)$ is the height at the grid point(x, y) and $\overline{h}$ mean value of the height given by

$$\overline{h} = \frac{1}{N} \sum_{x,y} h(x, y). \tag{III.7}$$

The temporal evolution of the surface roughness r is a good quantity to detect the transition from the 2-dimensional to the 3-dimensional growth mode.

Now we have all the necessary tools for the quantitative comparison of the dot patterns.

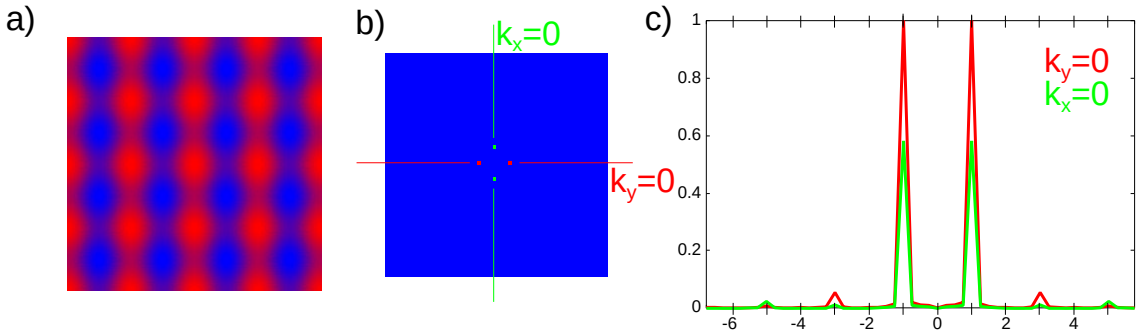

Figure III.8: The density plot of the spatial structure a) and of the Fourier transform b) of the pattern generated by $f(x, y) = 2\cos(x) + \cos(y)$ and two one-dimensional cuts c) as indicated by the lines in the density plot.

III.4.4 Variation of Coverage

Now we want to study the influence of parameter changes on the resulting patterns. Like in chapter II we will focus on growth parameters which are easy to access in experiments and keep internal parameters constant. The activation energies are the internal parameters kept fixed and the growth temperature and the flux rate are the parameters we will change. But there are two other parameters which we consider important, namely the coverage, i.e. the total number of atoms deposited onto the surface divided by the number of atoms in one monolayer and the growth interruption time we wait after the deposition has stopped.

The influence of the temperature T and the deposition rate F on the surface structures is widely discussed in the literature [25]. The temperature determines the diffusion constant D on the surface and the ratio F/D is often used to characterise surface structures. For high values of F/D in general the system is in the island growth mode and the structures tend to be rough hence they are often called fractal. For low values of F/D edges and boundaries are getting smoother and layer by layer growth can be observed. But this is only true for systems without strain. What happens if we include strain effects will be discussed in the next sections.

In the following we will perform simulations with $F = 1.0, 0.1$ and 0.01 monolayers per second (Ml/s) and with temperatures $T = 700, 750$ and 800 K. One series of images in the following figures is taken at those times when a certain coverage is reached, e.g., after 1s if we choose a coverage of $c = 0.1$ at a of flux $F = 0.1$ Ml/s or after 10 s if $F = 0.01$ Ml/s. The other series is taken 50s after the flux started. This means the systems has different growth interruption times and hence different times to relax towards equilibrium. Our intention is to optimise the total growth process, i.e. to find the conditions for best ordered and equally sized quantum dots, after a fixed total time. The figures of the surface structures are supplemented by graphs of the size distribution of the quantum dots and 2D-Fourier spectra of the surface structures. For the Fourier

spectra we treat all islands as if they have a constant height of 1, because we are only interested in the spatial arrangement of the islands.

We will discuss the influence of the parameters T , F and c in a sequence of increasing coverage c and study the role of T and F for a given coverage.

10% coverage

We start with a coverage of 10% or $c = 0.1$. The configuration of the surface, the size distribution and the 2D-Fourier spectrum of the surface at the time where the deposition is switched off, and $50s$ after the deposition started are shown in figure III.9 and figure III.10, respectively. For low temperatures ($T = 700K$) and high fluxes ($F = 1.0Ml/s$) a large number of very small islands can be found when the deposition ends after $0.1s$. After $50s$ many of theses small islands have decayed and have build up larger islands (see also figure III.11a)). The total number of islands has decreased because the coverage, i.e. the number of atoms on the surface, has remained constant. But we can see in the corresponding histogram of the islands sizes in figure III.10 that the size distribution is quite broad with a strong tail towards small islands. This can be explained by the different significance of Ostwald-ripening and strain effects for islands with different sizes. If the islands are all very small the strain and the corresponding change in the binding energy is small, too. This means that at the beginning of the growth process Ostwald-ripening dominates and an island with a larger boundary can collect more atoms consequently small islands will loose atoms to the larger islands. But the larger the islands grow the stronger is the strain and it becomes more and more unfavourable for an atom to attach to a large island. The large islands will not stop to grow, because the strain is still not strong enough, but will grow much slower than smaller islands. This explains the sharp drop in the size distribution for large islands and the soft decrease on the lower edge of the maximum.

If we lower the flux to $F = 0.1Ml/s$ the situation remains pretty much the same. Only if we reach a flux of $F = 0.01Ml/s$ the dynamics changes. Now the time between the deposition of two new atoms on the surface is so long that the first atom can diffuse over a large distance before the second arrives on the surface. If the first atom can reach an island during this time the possibility of forming new island seeds is strongly reduced. As a result the dynamics is now no longer dominated by a large number of small islands which try to grow at the cost of other islands but by a small number of islands (see figure III.11a)) which grow one after the other until a size is reached where the strain will slow down or even stop the growth. If we compare the histogram for this case at the end of the deposition, which here is at $t = 10s$, with the corresponding one after $50s$ we can see that the maximum has not moved. This confirms the assumption that the islands at the maximum $d = 9$ have reached the point where the strain stops the growth; the phenomenological correction term E_c at the boundary of an island is here about 0.25 eV. The histograms also show that the size distribution has sharpened during

the growth interruption time. The islands which had not reached a diameter of $d = 9$ at the time when the deposition was stopped have grown due to Ostwald-ripening.

The changes in the dynamics are even more visible when the temperature is increased. Now even for a high flux of $F = 1.0Ml/s$ a sharp size distribution can be reached after $50s$. The final states for $T = 750K$ and $T = 800K$ are very similar and independent of the flux. As mentioned before the critical diameter where the strain stops the growth of the island is about $d = 9$. Only for a low flux of $F = 0.01Ml/s$ a considerable number of islands have a diameter of $d = 10$. The reason is the different evolution of the islands. As mentioned before for low fluxes the islands grow one by one up to the size where the strain stops the growth. As a result large islands can be found very early on the surface and eventually atoms will attach to one of these large island and the island grows. This can lead to a couple of large islands which are slightly larger than the critical size. The different evolution can also be seen in the histograms. If, e.g., we compare the histograms for $F = 0.1Ml/s$ and $F = 0.01Ml/s$ at $T = 750K$ at the end of the deposition we can see a distribution with a maximum below the critical value with tails to larger and smaller diameters for $F = 0.1Ml/s$, but a maximum at the critical value and only a tail to lower diameter for $F = 0.01Ml/s$. One might object that the snapshots of the size distribution are taken at different times, $t = 1.0s$ for $F = 0.1Ml/s$ and $t = 10.0s$ for $F = 0.01Ml/s$, and that the size distribution might look similar, if they were taken at the same time, like the ones taken at $t = 50s$. This might be true for times when in both systems most of the islands have reached the critical size, but during the early stages of the growth the evolution of the size-distributions is indeed different. For high fluxes in the beginning there is a large number of small islands leading to a strong peak in the size-distribution at small diameters. This peak will move to larger values with the passing time until the critical diameter is reached. For low fluxes only a few but large islands will be on the surface at early stages. Here the size-distribution always has a peak near the critical diameter which will grow with time.

Common to all systems with a coverage of 10% is the missing ordering of the islands on the surface. None of the Fourier-spectra in figure III.9 and figure III.10 show any distinct peaks or structures. The low coverage leads first to small islands which produce a strain field which is small in range and amplitude. Secondly it implies a large mean distance between two islands and as a result the influence on other islands due to the strain field is very small. Consequently no interaction between the islands is possible and no ordered structure can arise. Also all systems are still in the 2-dimensional growth mode which can be seen by the flat lines in figure III.11b) after the deposition has ended.

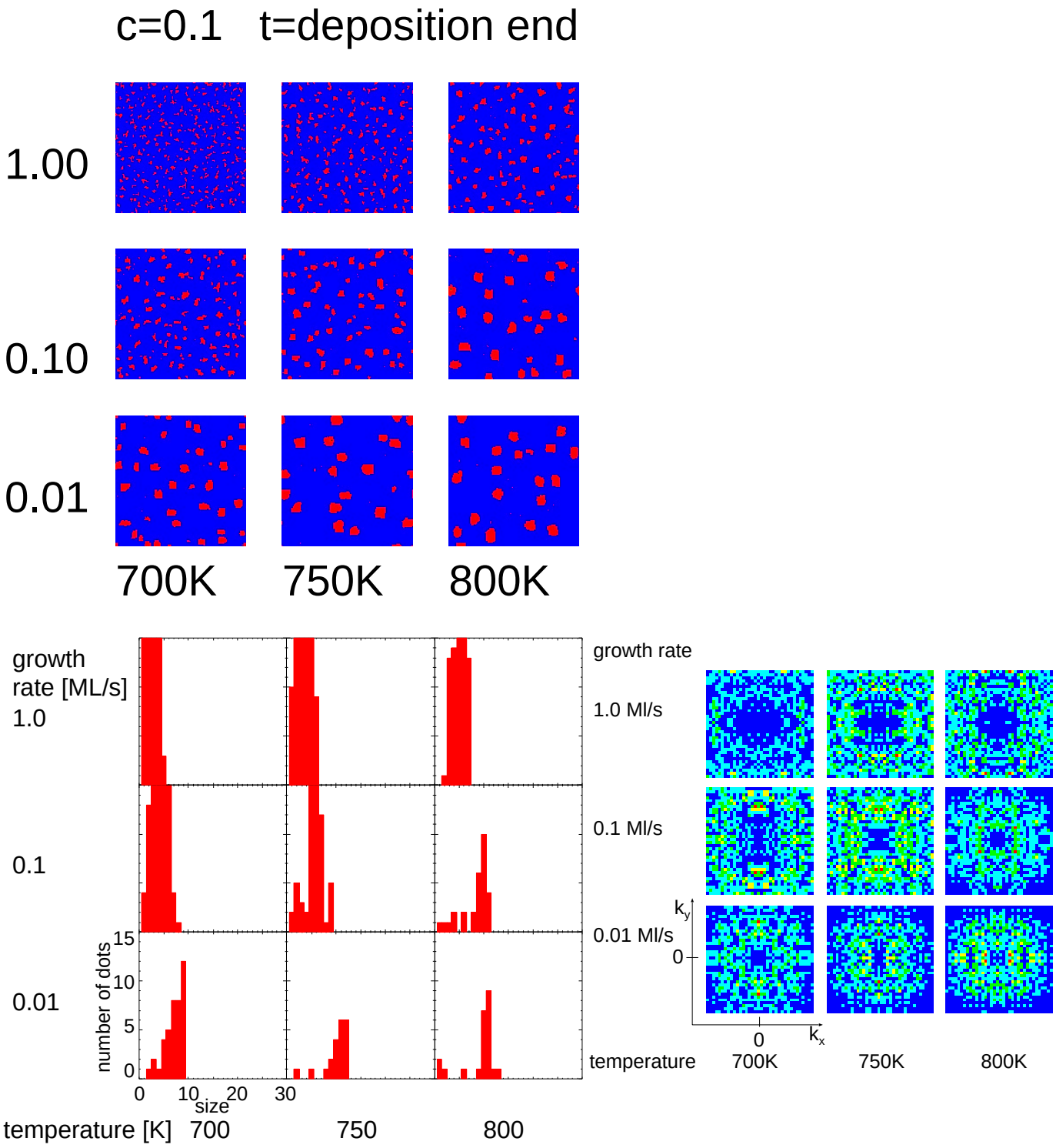

Figure III.9: In the upper plots of the surface structure the results of Monte Carlo simulation with different temperatures ($T = 700K$, $T = 750K$ and $T = 800K$) and different fluxes ($F = 1.0Ml/s$, $F = 0.1Ml/s$ and $F = 0.01Ml/s$) and a coverage of $c = 0.1$ at the end of the deposition ($t = de$) can be found. In the lower left diagram the corresponding islands-size distributions are shown while the corresponding Fourier spectra can be found in the lower right diagram.

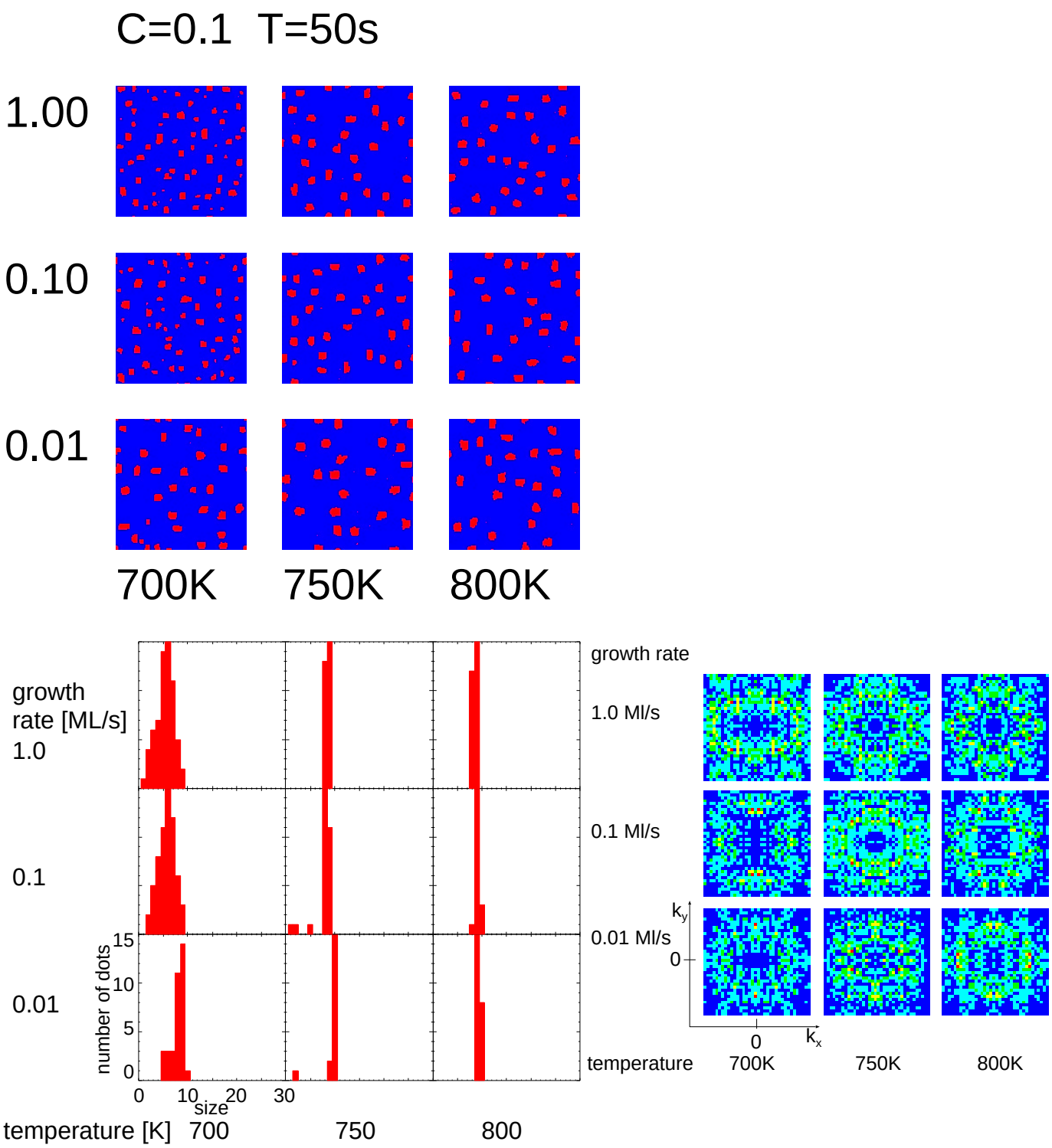

Figure III.10: Same as figure III.9 but at $t = 50s$.

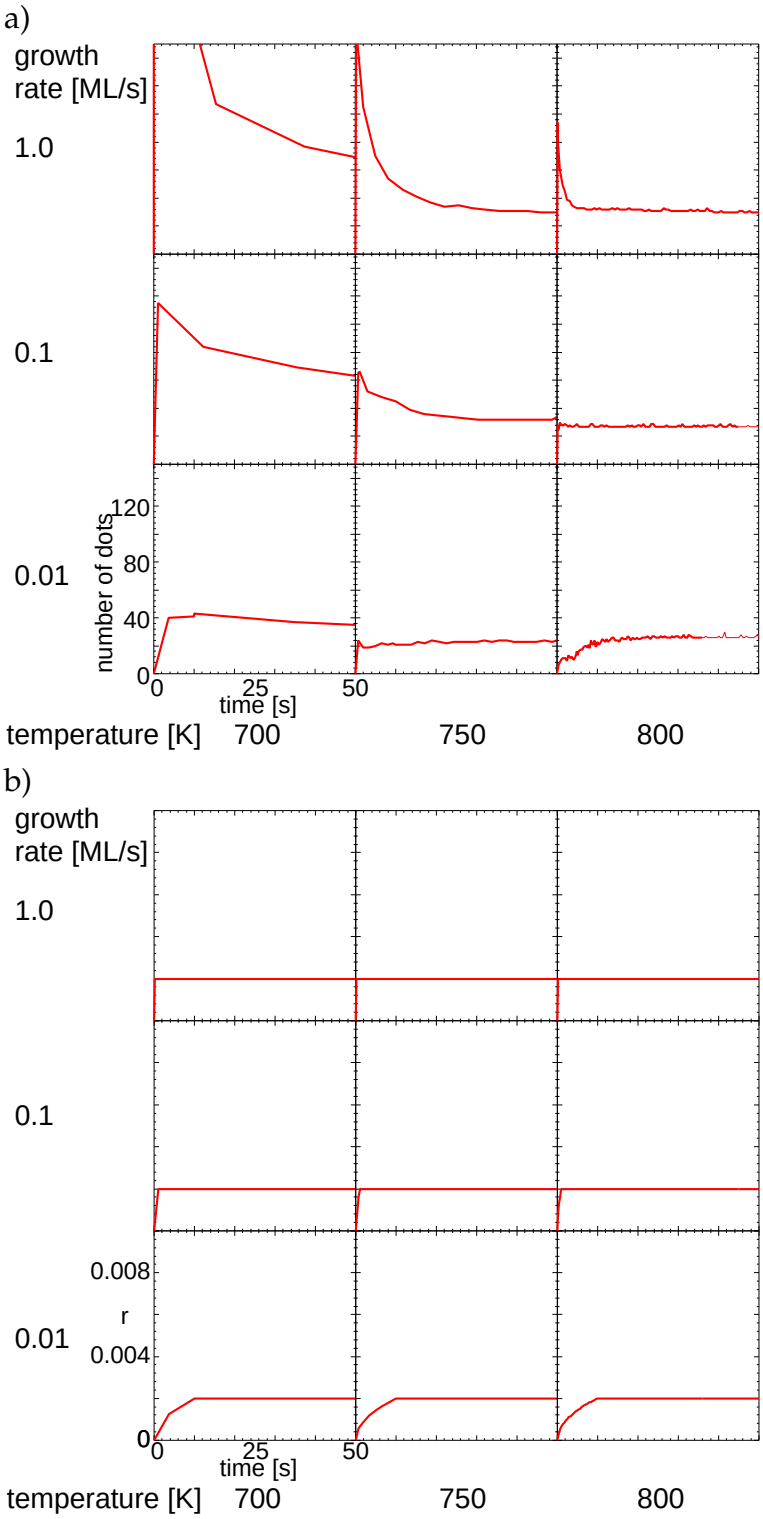

Figure III.11: Temporal evolution of the number of islands (a) and the surface roughness r (b) for the simulations of figure III.9 and III.10.

20% coverage

Now we increase the coverage to $c = 0.2$, the corresponding results are shown in figure III.12 and figure III.13. For $T = 700K$ there is not much change with respect to the size distribution compared to the results for $c = 0.1$. The total number of islands has increased (see figure III.14a)) but the critical size is still about $d = 9$. At a flux of $F = 0.01Ml/s$ most of the islands are larger than the critical size after the end of deposition, which is after $20s$ in this case. This leads to a broad size distribution above the critical size. The reason why for low fluxes many islands are larger than the critical size was already discussed in the last paragraph but here we can see additionally that islands larger than the critical size will not shrink easily. At the end of the deposition a couple of islands which are smaller than the critical size can be found. In the size-distribution after $50s$ they have vanished. They have in fact grown up to the critical size by taking some atoms of larger islands. Most of the islands were already larger than the critical size at $t = 20s$ and so most of them remain so after $50s$. The only way to get a sharp size distribution around the critical size under these conditions is by the formation of new islands which can take away atoms from the islands which are too large. But this is a very rare process and it would take a long time to improve the size distribution. The same can be observed for $T = 750K$ and $T = 800K$ for the same flux.

The size distributions of the other systems have not changed much compared to the corresponding systems with $c = 0.1$. But because of the larger number of islands on the surface the interaction of the islands has increased and an early stage of ordering on the surface can be found. This can be seen at two points in the Fourier-spectra. First the systems ($T = 750K$, $F = 0.01Ml/s$), ($T = 800K$, $F = 0.1Ml/s$) and ($T = 800K$, $F = 0.01Ml/s$) show a small amplitude of the Fourier modes with small and large values of $|k|$. Only for intermediate values of $|k|$ the amplitude of the Fourier modes is considerable. This indicates a preferred distance of the islands. Second, when comparing the spatial structure of the Fourier-spectra at the end of the deposition and after $50s$ a change from a more or less circular symmetry to a square symmetry can be found. This indicates the existence of preferred directions. The more regular arrangement of the islands can also be seen in the corresponding images of the surface structure. Islands which are aligned along rows and columns can be found but only in small parts on the surface.

All systems are still in the 2-dimensional growth mode, which can be seen in figure III.14b).

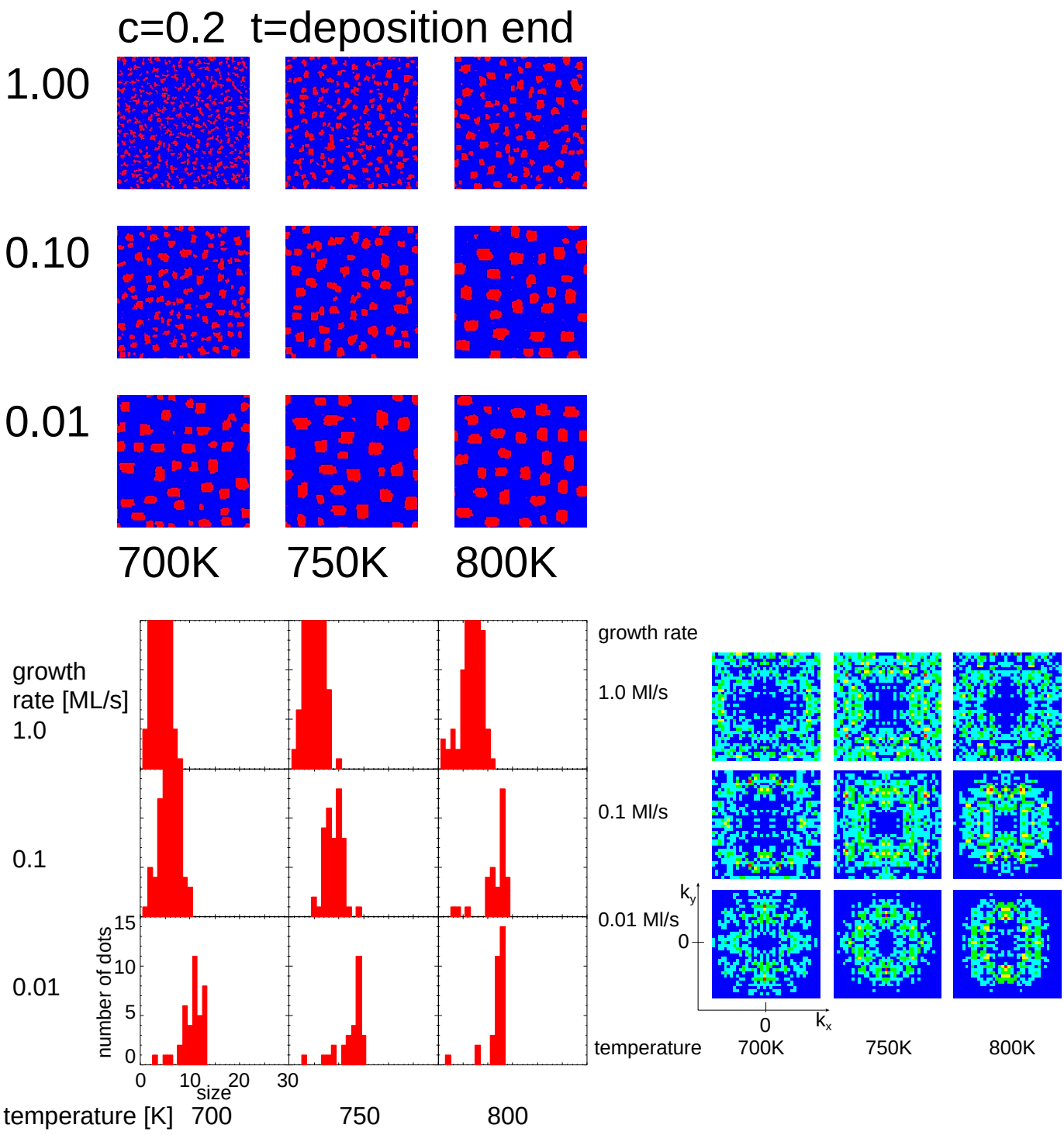

Figure III.12: Same as figure III.9 but with $c = 0.2$.

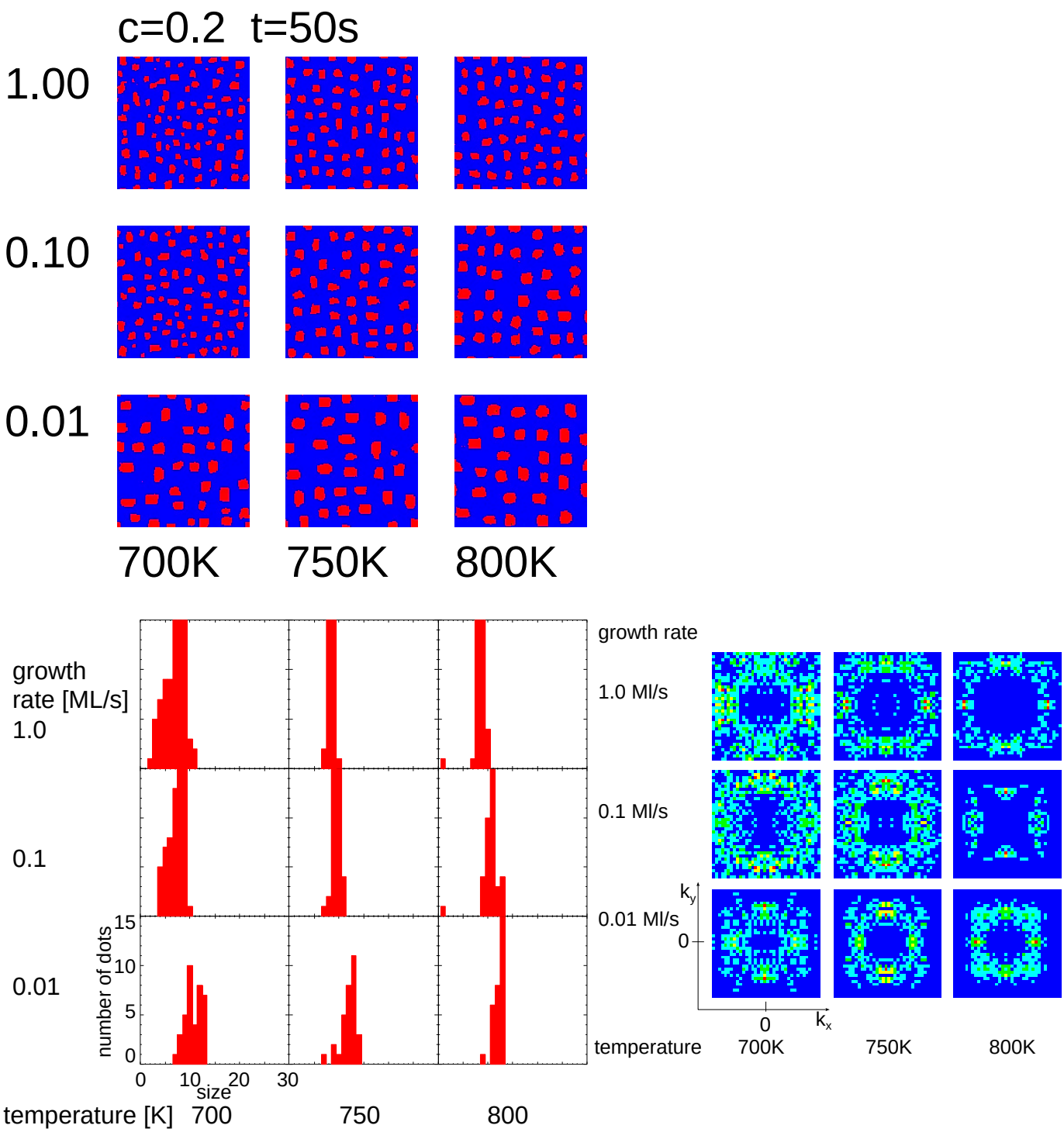

Figure III.13: Same as figure III.12 but at $t = 50s$.

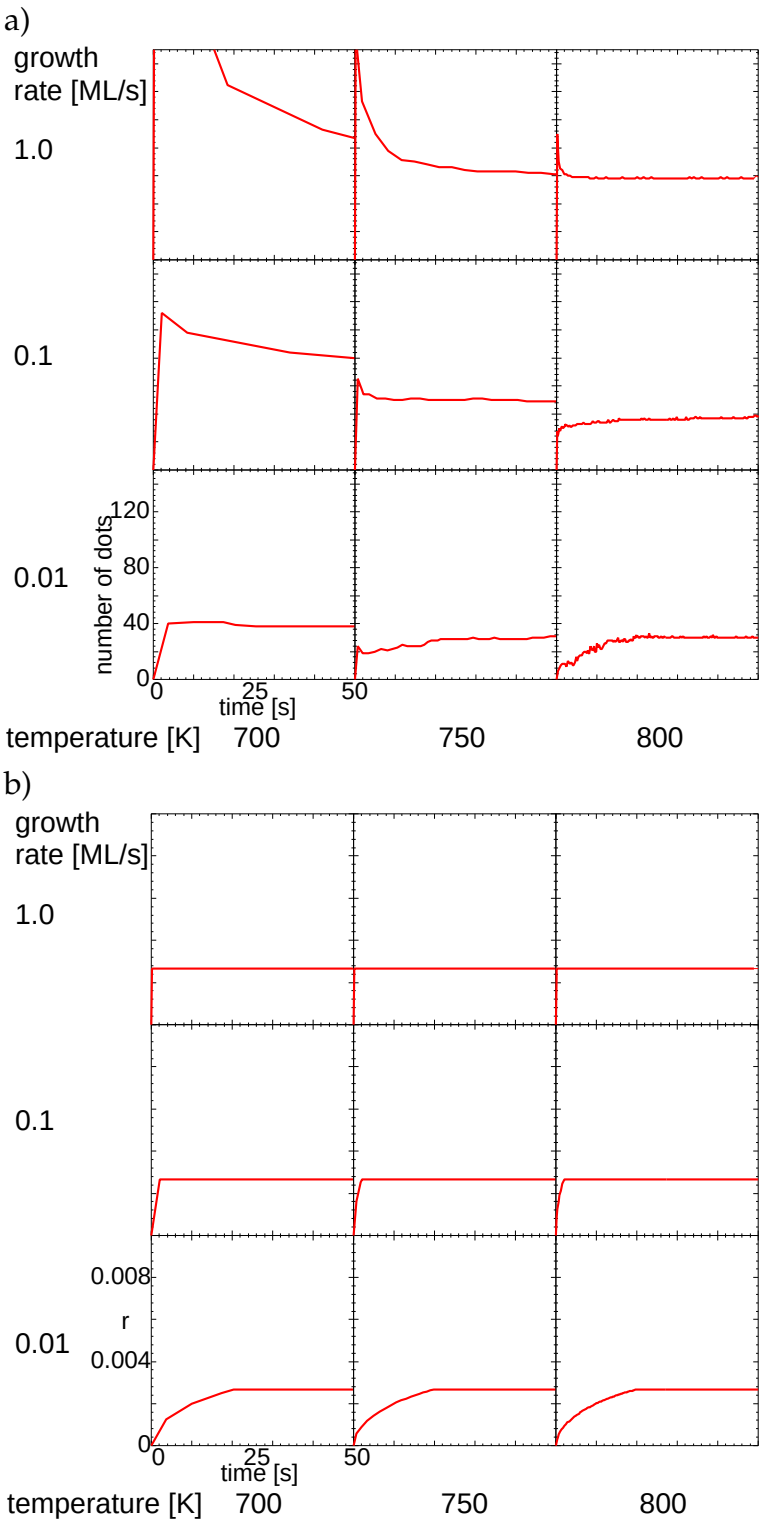

Figure III.14: Temporal evolution of the number of islands (a) and the surface roughness r (b) for the simulations of figure III.12 and III.13.

30% coverage

At a coverage of 30%, i.e. $c = 0.3$, the spatial ordering is already visible in some of the figures of the surface configuration in figure III.15 and in nearly all plots in figure III.16. The number of islands and their sizes are now both large enough to get a strong interaction between the islands and a pronounced ordering of the islands on the surface. The Fourier diagrams show this structure, too, by sharp peaks indicating a preferred wave-length, i.e. distance of the islands, in x and y direction. This wave-length is the same for both directions, because not only the diffusion of the atoms on the surface but also the strain is isotropic in our simulations.

The Fourier-spectra also indicate that sometimes the ordering is stronger in one direction than in the other. But this is purely random which can be seen in figure III.18 where we have performed 10 different simulations with the same parameters ($T = 750K$, $F = 0.01Ml/s$, $c = 30\%$) and different sequences of random numbers. Together with the structure of the surface the corresponding Fourier-spectra are shown and we can find alignment along x (peak in k_x), along y (peak in k_y) direction and along both directions (peak in both k_x and k_y). This is another indication that the arrangement on the surface is a local effect. In a much larger system than the one we used here we would locally find all types if alignment but here the system is so small that only one dominant type of alignment is visible at once.

The evolution of the size distribution is similar to the cases for $c = 0.1$ and $c = 0.2$ discussed above. For $T = 750K$ and $T = 800K$ we get sharp size distributions for all fluxes after $50s$, but for low temperatures (here $T = 700K$) an interesting tendency can be found. If we neglect the two large islands for $F = 1.0Ml/s$ the size distribution in figure III.16 for this large flux is much sharper than for lower fluxes. The reason can be found in the different growth modes mentioned above. While for high fluxes the islands all grow simultaneously they will grow one after the other for low fluxes. In the first case at an early stage of the growth the seeds of the islands are distributed uniformly over the surface and some of them grow while some of them decay. The small average size of the islands and the possibility to decay give a large flexibility to the system. In contrast in the second case we have large islands already in early stages of the growth. These islands will not decay and only move very slowly and as a result the system can equalise disturbances much less efficiently than in the first case. However, the loss of flexibility can be compensated by increasing the temperature which can be seen at $T = 750K$ and $T = 800K$.

Nearly all systems show a transition from the 2-dimensional to the 3-dimensional growth mode which can be seen by small jumps in the curves of figure III.17b). This is, e.g., clearly visible for the system with $F = 0.01Ml/s$ at $T = 800K$ at $t \approx 30s$ indicating a quite fast transition to the second layer. It has to be noted that the transition does not set in until the deposition has ended, because the probability to form a seed for a second layer increases with the number of atoms on the surface and with the passed time. The

reason why the system with a flux of $F = 1.0Ml/s$ at $T = 750$ does not show a second layer is due to the random nature of the Monte Carlo simulation. In a longer simulation or a simulation with a different sequence of random numbers a second layer might be found.

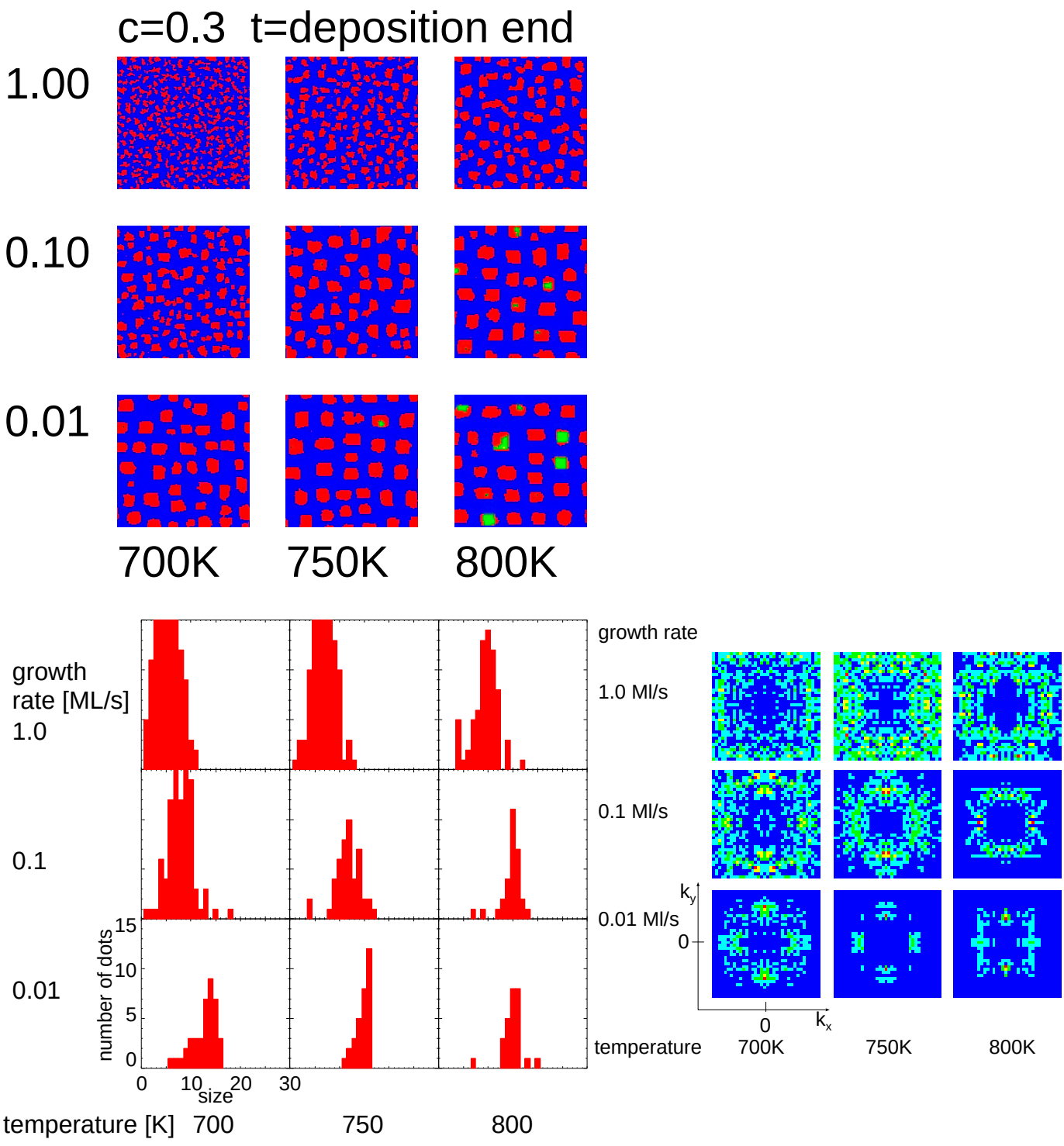

Figure III.15: Same as figure III.9 but with $c = 0.3$.

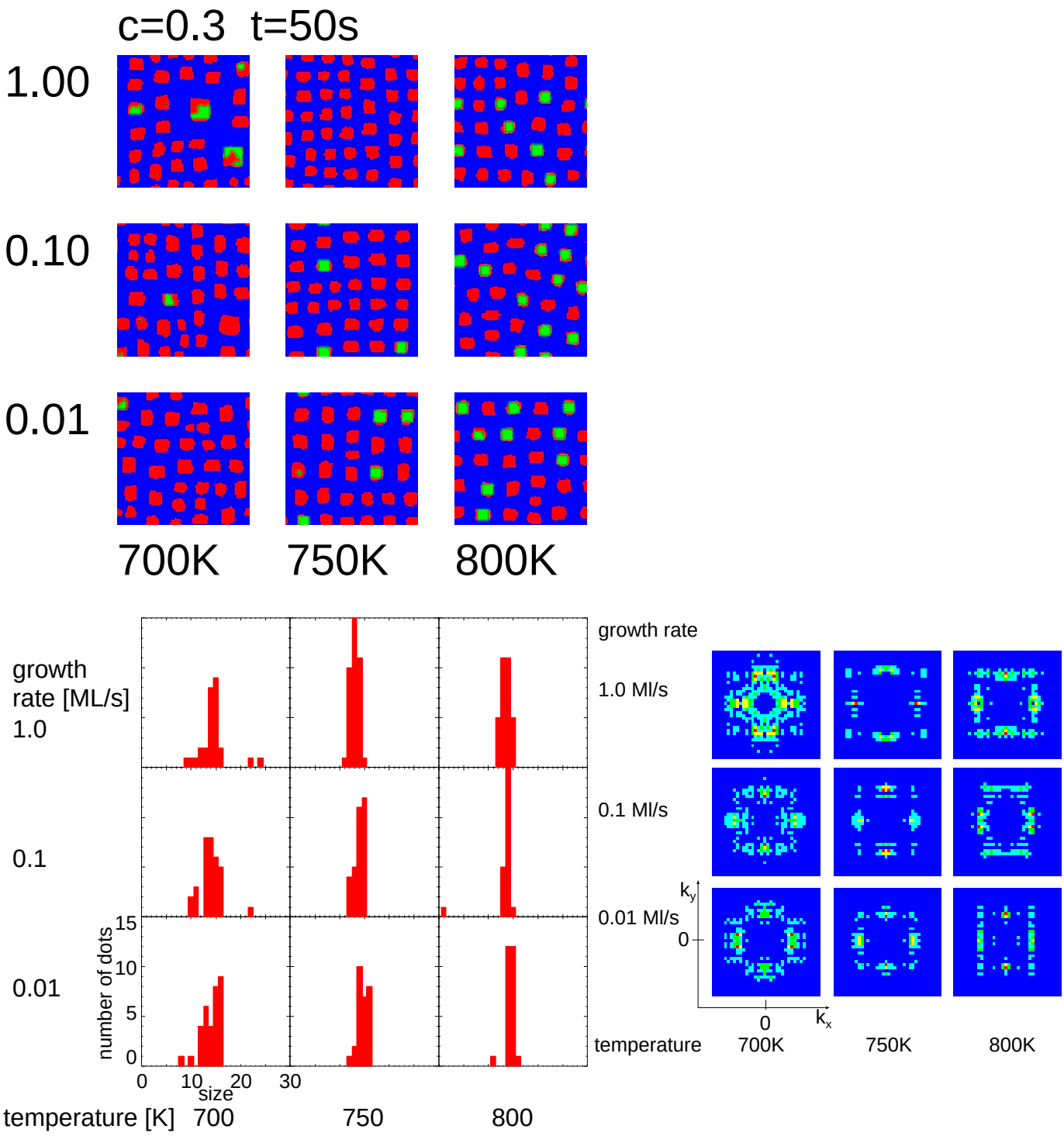

Figure III.16: Same as figure III.15 but at $t = 50s$.

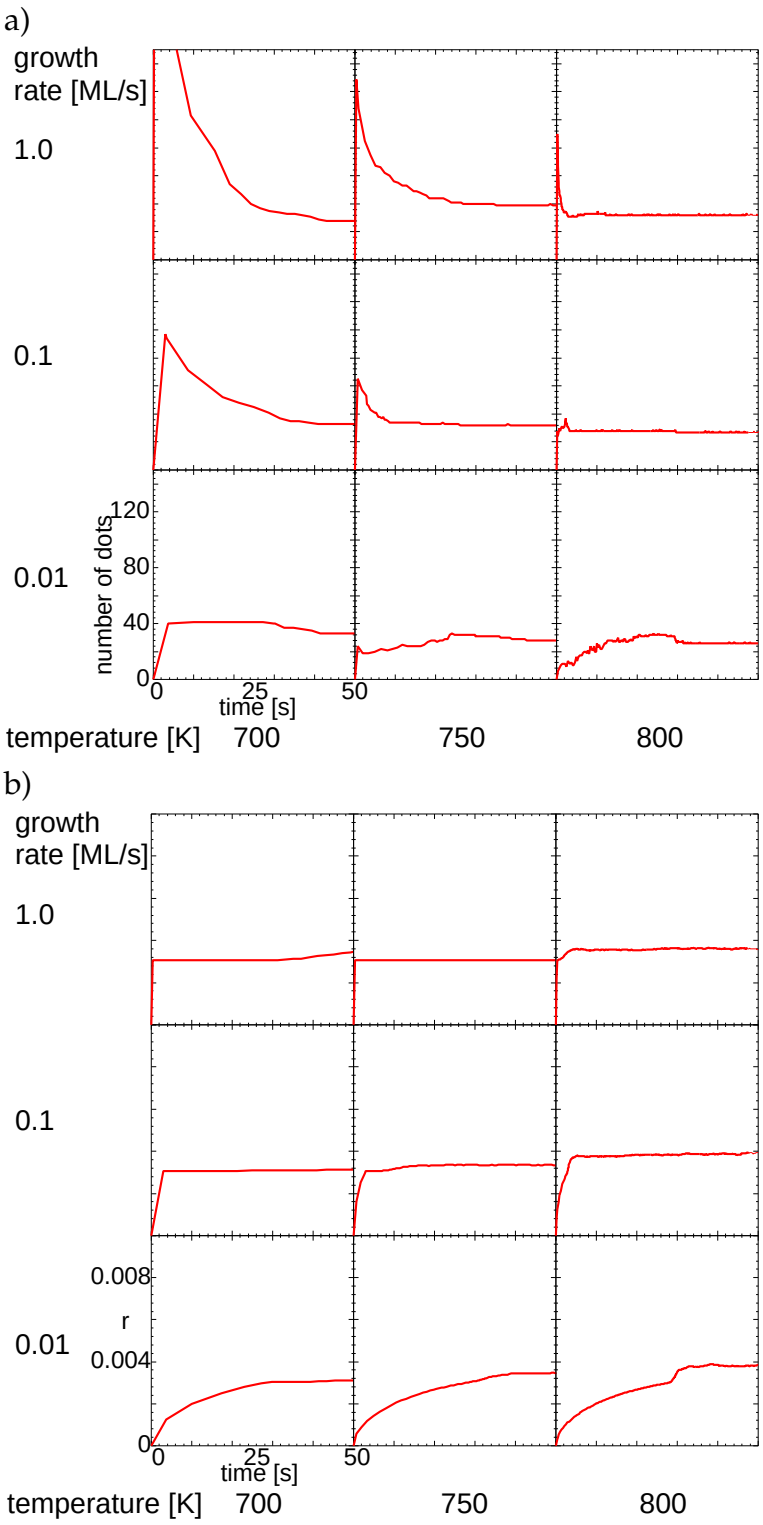

Figure III.17: Temporal evolution of the number of islands (a) and the surface roughness r (b) for the simulations of figure III.15 and III.16.

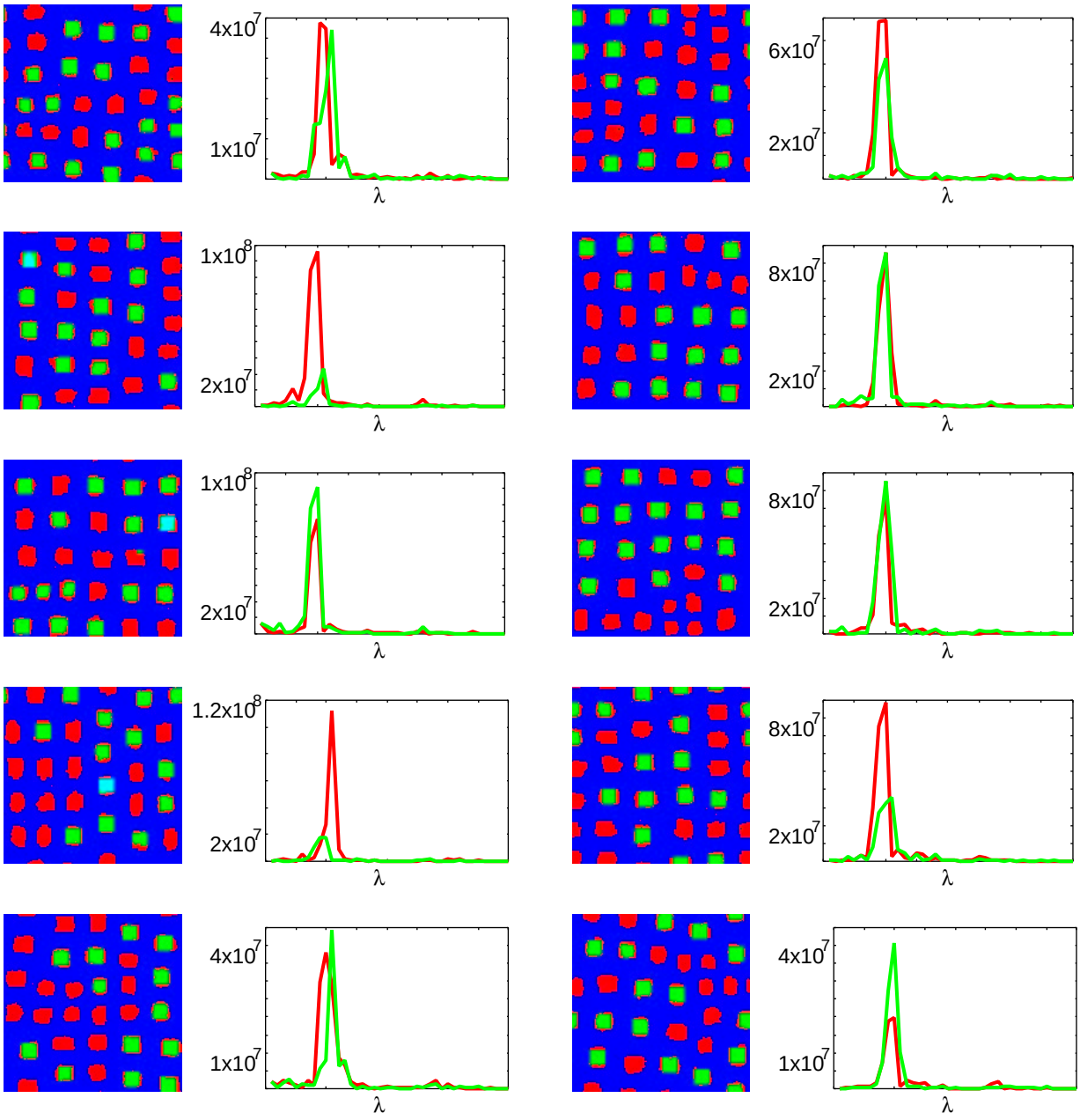

Figure III.18: The final structures of ten Monte Carlo simulations with the same parameters but different sequences of random numbers. Together with the structure of the surface two slices ($k_x = 0$ (red) and $k_y = 0$ (green)) of the corresponding 2D Fourier-spectra are shown. These plots demonstrate that the existence of a preferred direction in space is purely accidental.

35% coverage

If we increase the coverage by another 5% to $c = 0.35$ a dramatic change can be observed. The size distributions at the end of the deposition in figure III.19 look very similar compared to the corresponding distributions at a coverage of 30% in figure III.15. Only the width of the distribution-functions is a bit larger due to the larger number of atoms on the surface. But after $50s$ for low temperatures and high fluxes no peak in the size distribution can be found anymore. The plot of the configuration on the surface reveals that now the islands have clustered together to form a small number of larger islands or clusters. There are still some smaller islands but the surface is dominated by the clusters. Now the question arises why this is possible. We have seen earlier that the strain stops the growth of a large island and leads to a flux of atoms from a large island to a smaller one. Why does this not happen here? The answer is that the strain does not grow with the island size for all sizes but saturates so that at a certain size an increase in the island size will not produce a stronger strain field. The clusters are so large that the strain field around the island is not changed when an atom attaches or separates from the island. It is still more favourable for an atom to attach to a smaller island which has not reached the saturation point, but the large islands can catch diffusing atoms because of their large boundary. We have entered the regime of Ostwald ripening again. The desired behaviour that large islands shrink while small islands grow can still be found under certain conditions. At a temperature $T = 750K$ and a flux of $F = 0.01Ml/s$ a couple of large islands can be found at the end of the deposition ($t = 35s$) which have vanished at the end of the simulation $15s$ later.

For higher temperatures and lower growth rates we still get nicely ordered quantum dots with a sharp size distribution. Especially for $T = 800K$ the size distribution is much sharper compared to the systems with a coverage of 30%. Also the Fourier-spectra show a more pronounced structure. If we now compare the diagrams of the configuration on the surface the difference between the systems producing quantum dots and the ones generating clusters becomes clear. In the clustered systems most of the atoms are still in the first layer on top of the substrate, while in the systems forming quantum dot arrays a considerable amount of particles have moved up to the second or higher layers. With more atoms in the first layer the islands have to become larger and as a consequence they will form clusters.

The results indicate that the transport of atoms to the second layer depends on the growth conditions, i.e. the growth temperature and the growth rate. Many atoms move to higher layers at high temperatures and low fluxes and most of the atoms stay in the first layer for low temperatures and high fluxes which can be seen, e.g., by the flat curves in figure III.21b) for $T = 700K$ and $F = 1.0Ml/s$ and $F = 0.1Ml/s$. One can think of cluster formation and the transition to the 3-dimensional growth mode being two competing processes. This is another effect of the higher mobility of the atoms at higher temperature. Because a single atom moves much more often in a given interval of time when the temperature is high the probability to move to the second layer is also

higher. But when the probability to find atoms on the second layer rises the probability for the creation of new islands in the second layer, i.e. islands on top of other islands rises as well. Consequently when there are islands in the second layer atoms are more likely to stay in the second layer because they are attached to an island.

This might be the physical reason determining if a given system shows either clusters or quantum dots, but we have to be careful here. As mentioned earlier the hopping processes of the Monte Carlo simulation are only modelled for the first layer. Atoms are allowed to move on top of other atoms but under what conditions this can happen and what energies are involved is not clear. We are leaving the validity of the presented Monte Carlo model. It might be possible that the transport to higher layers is more efficient than it is in the model discussed here and the formation of clusters is delayed, but also the opposite might be true. Nevertheless the formation of clusters can be observed experimentally [139] and should also be found in the simulations but it is not obvious up to what degree the experimental and simulated conditions can be compared quantitatively.

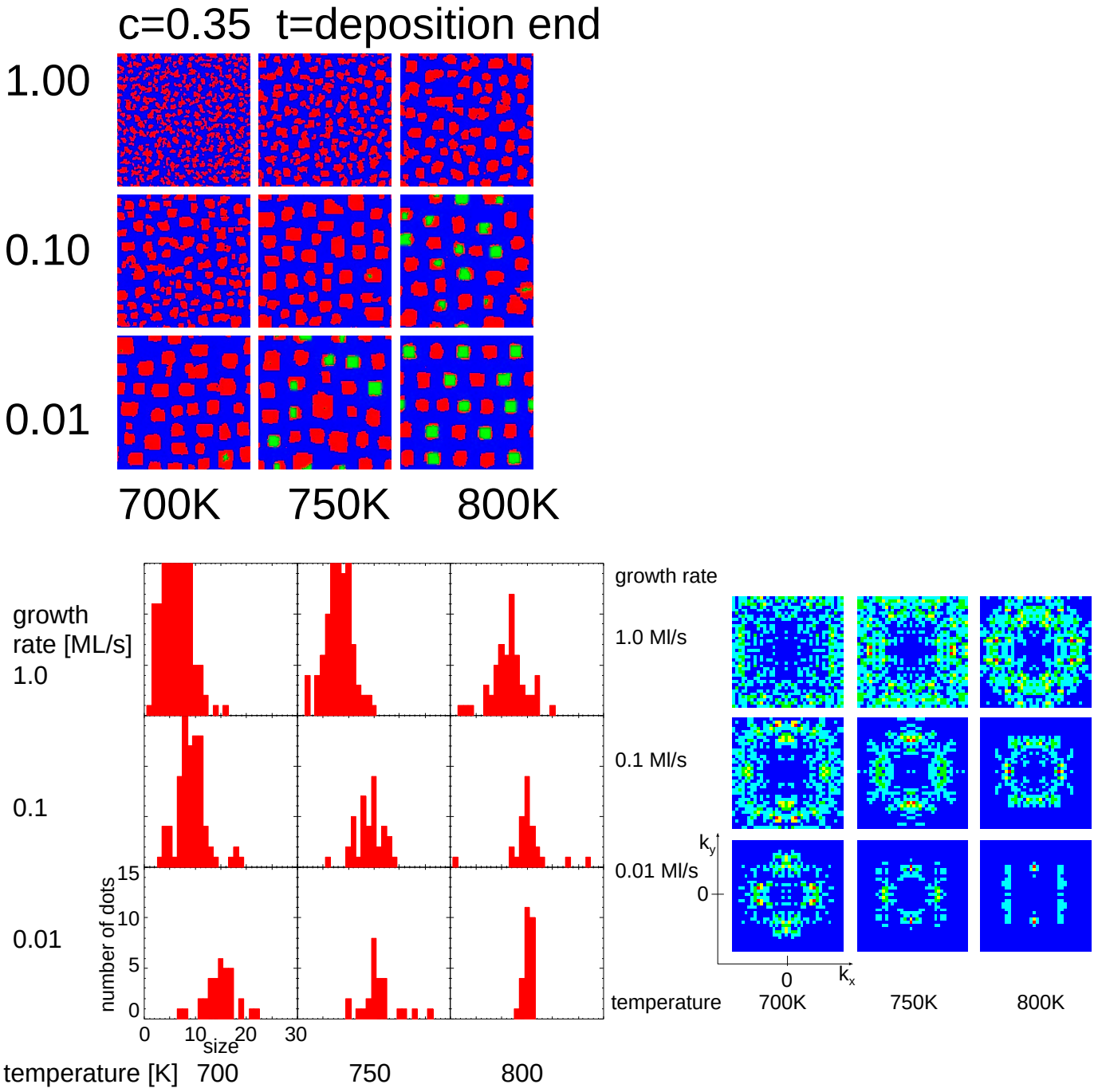

Figure III.19: Same as figure III.9 but with $c = 0.35$.

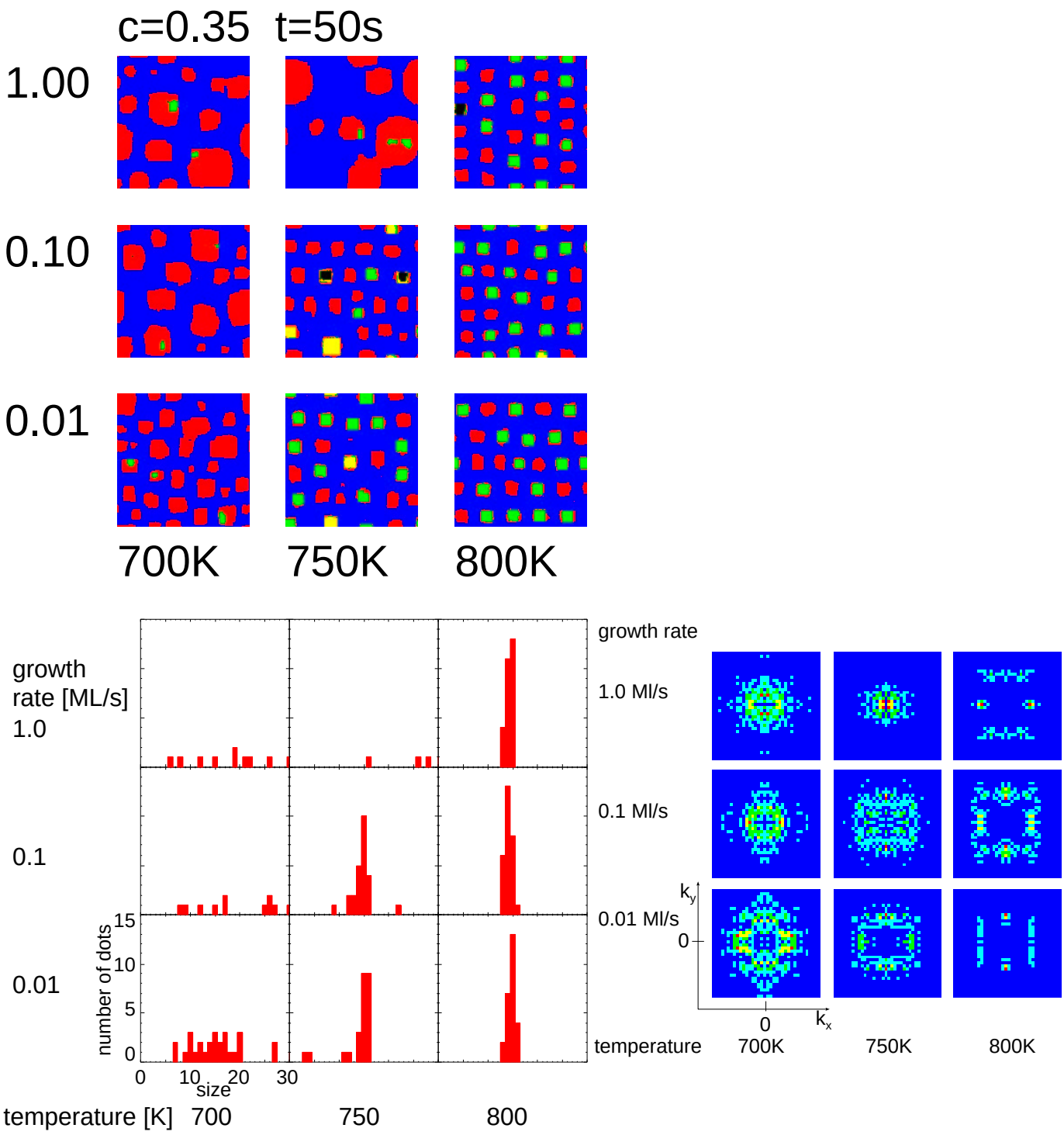

Figure III.20: Same as figure III.19 but at $t = 50s$.

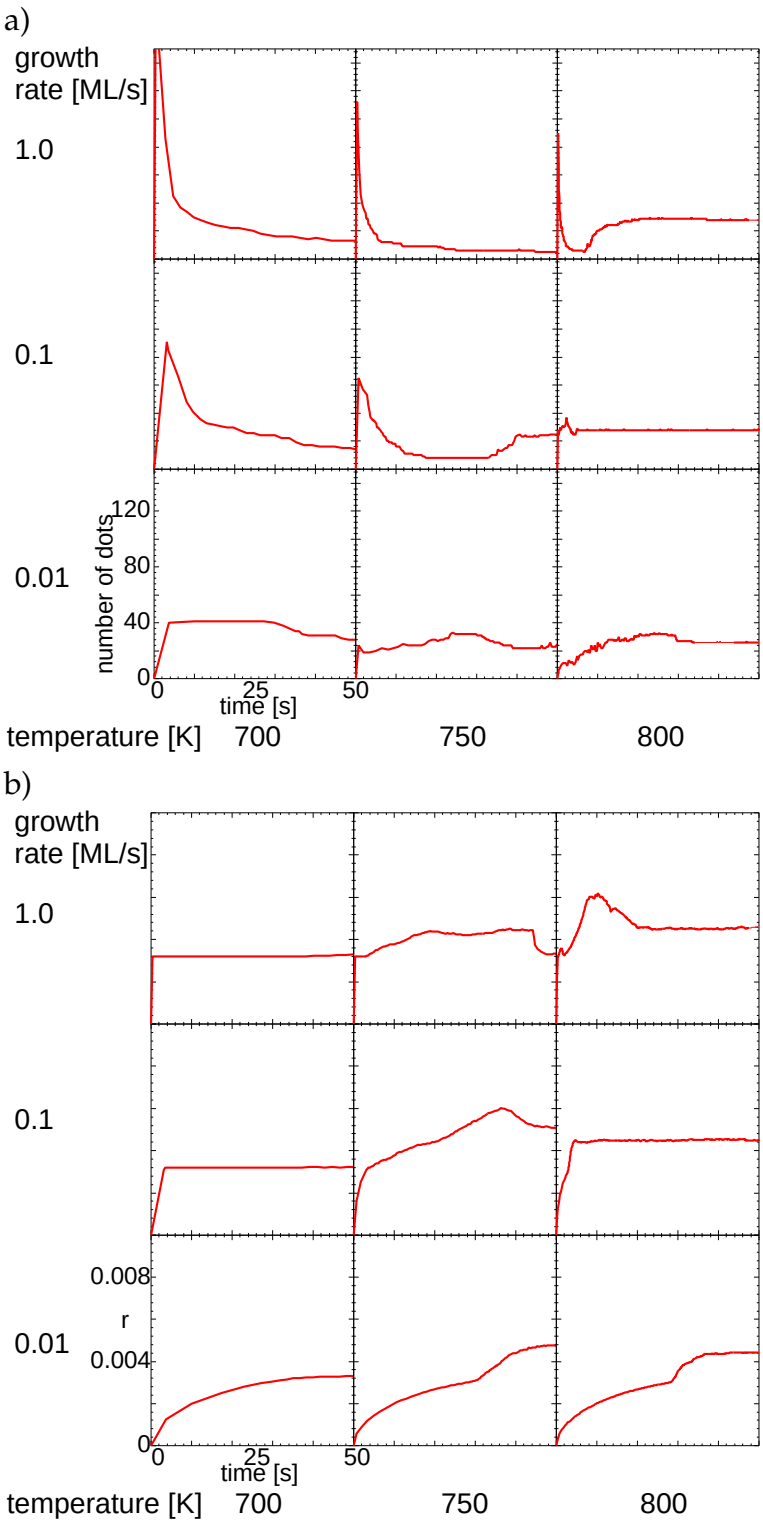

Figure III.21: Temporal evolution of the number of islands (a) and the surface roughness r (b) for the simulations of figure III.19 and III.20.

40% coverage

Finally we present the results for a coverage of 40% in figure III.22 and III.23. Although we have already reached the limits of the Monte Carlo model for certain parameters for a coverage of 35% we show the results for a coverage of 40% here to demonstrate that the tendencies which became visible in the earlier section continues.

The size distributions at the end of the deposition in figure III.22 still show a peaked structure like in figure III.19 and III.15. Only the width of the peaks is larger due to the higher number of atoms on the surface. In the following figure III.23 the structure of the surface $50s$ after the growth has started is plotted. Only the system with a flux of $F = 0.01Ml/s$ at a temperature of $800K$ has produced quantum dots. All other systems show large clusters. Even in the other systems at a temperature of $T = 800K$ larger cluster have formed. Their diameter is even larger than the range plotted in and which we keep fixed to facilitate the comparison of different systems. The size distribution of the system with a flux of $= 0.1Ml/s$ at $T = 800K$ still looks promising at the end of the deposition since only two large islands can be found in the lower right corner of the system, but these two islands finally dominate the system by merging together and absorbing all atoms on the surface.

The size distributions of the systems with $F = 0.01Ml/s$ and $T = 800K$ with a coverage for 35% in figure III.20 and 40% in figure III.23 are very similar. A comparison of the corresponding plots of the surface structure indicates that only the number of atoms in higher layers has increased, which can be seen in the corresponding plot of the surface roughness r in figure III.21b) and figure III.24b), but the principal structure is still the same. Evidently the transport of atoms into higher layers here is still quite effective and prevents the formation of clusters. It has to be noted that the preferred alignment in the y direction in both cases is completely accidental as shown earlier in figure III.18.

If look at the system with $F = 0.01Ml/s$ at $T = 800K$ and compare the time evolution of the surface roughness r for coverages $c = 30\%$, $c = 35\%$ and $c = 40\%$ we can identify two different stages. One fast stage which can be found in all three systems at $t \approx 30s$ followed by a slow stage which is slightly visible for $c = 35\%$ and good visible for $c = 40\%$. This indicates that if there are enough atoms on the surface after a fast nucleation of a second layer the atoms continue to move to the higher layer but much slower. Also here it has to be noted that we are near the limits of the model and that a more detailed description of the higher layers is necessary to make strong statements.

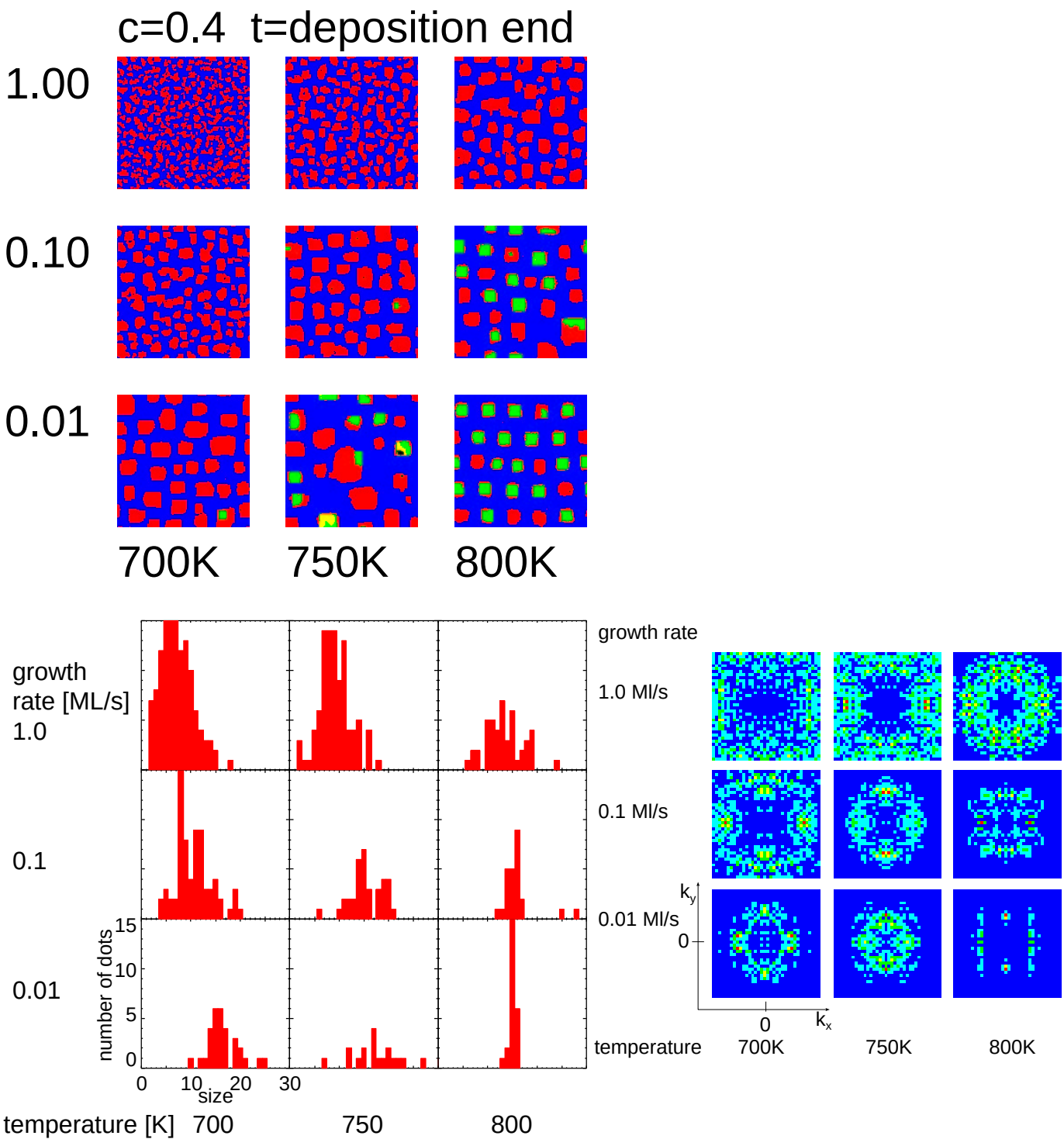

Figure III.22: Same as figure III.9 but with $c = 0.4$.

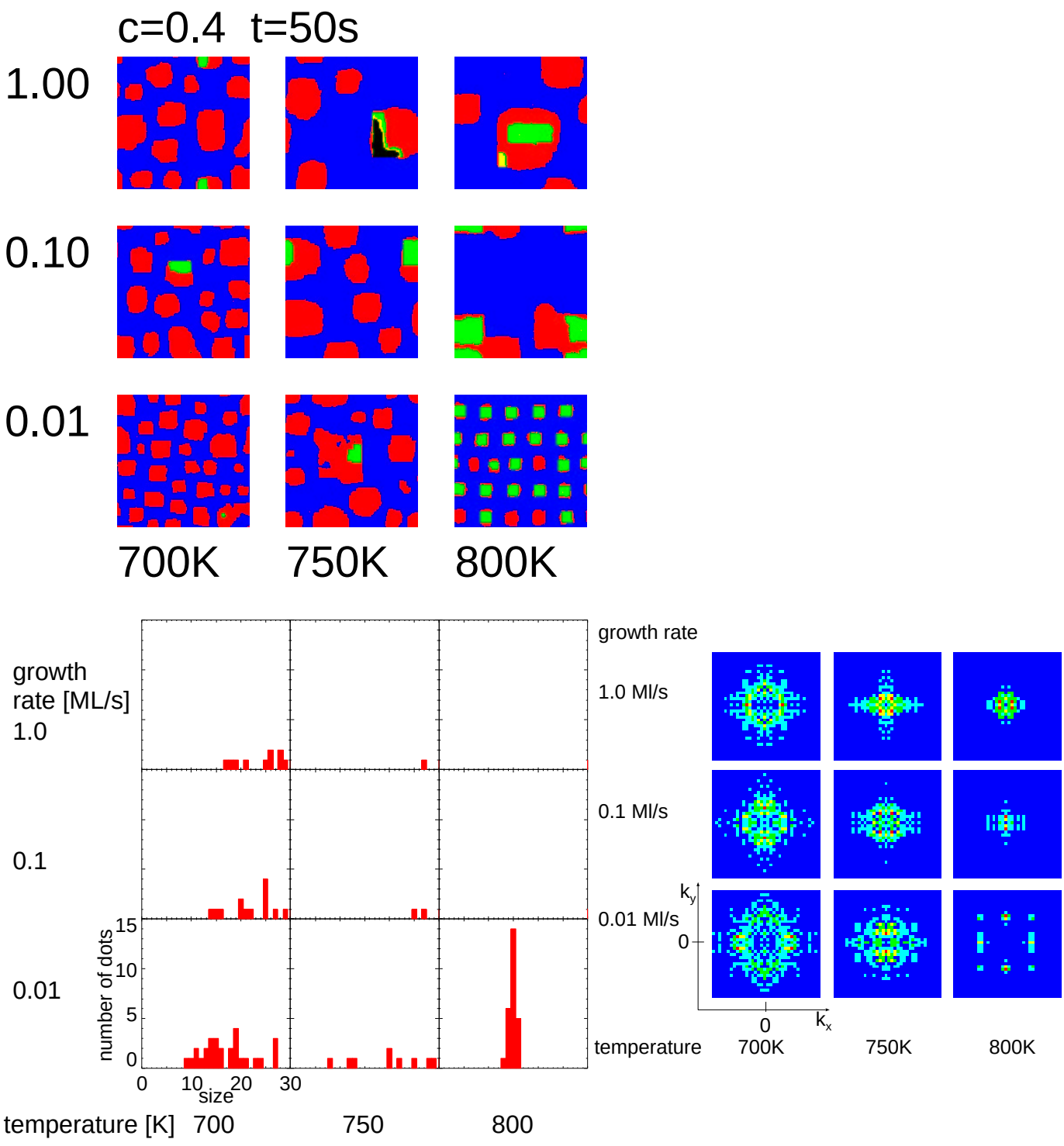

Figure III.23: Same as figure III.22 but at $t = 50s$.

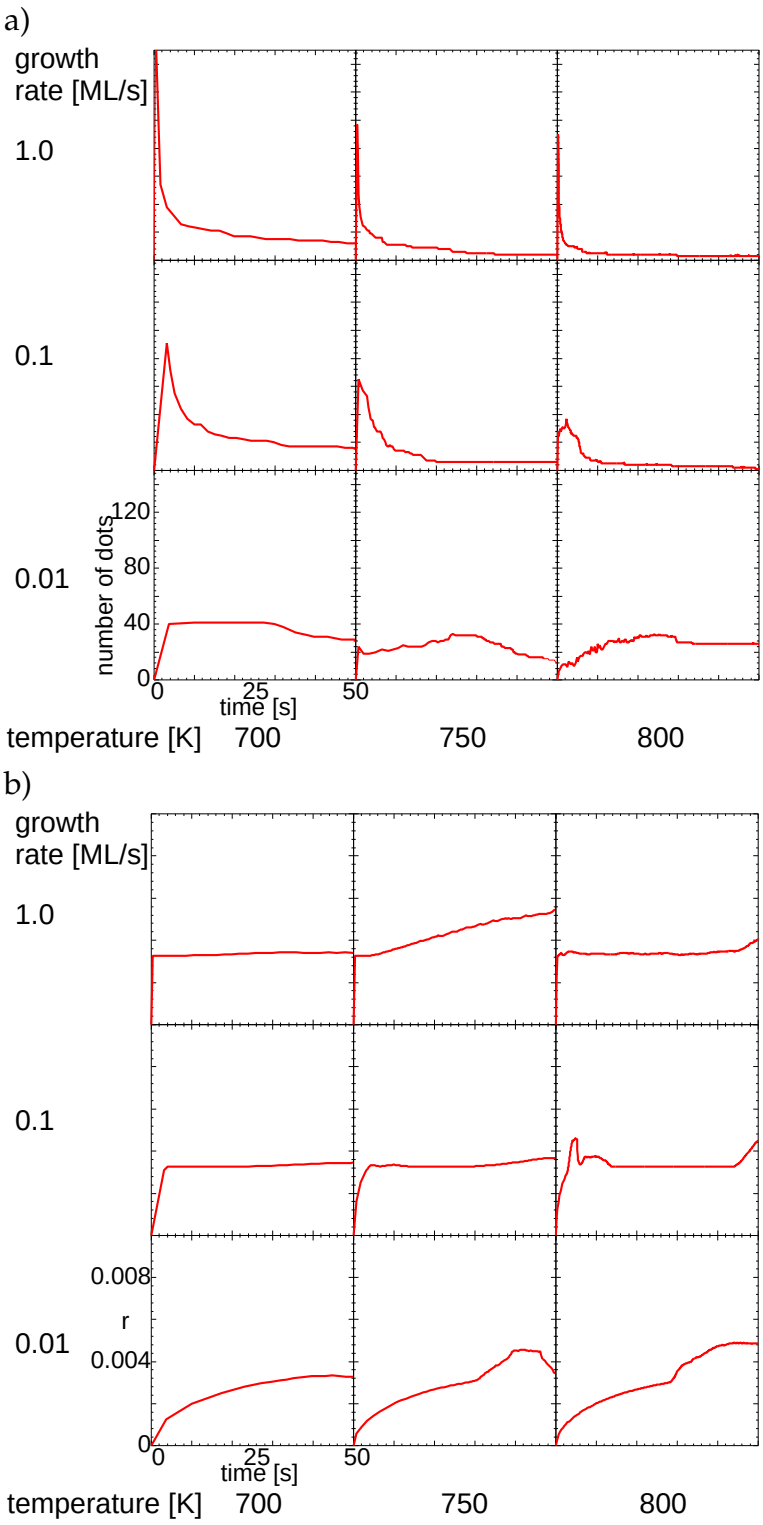

Figure III.24: Temporal evolution of the number of islands (a) and the surface roughness r (b) for the simulations of figure III.22 and III.23.

III.4.5 Summary

In summary we have found three main regimes in the growth of quantum dots in the kinetic Monte Carlo model. First a large number of small islands come into existence but under appropriate conditions and after some growth interruption during which the configuration relaxes the size distribution is very sharp due to strain effects which lead to a "cooperative" growth. This indicates that the size ordering is a long range non-local effect. Secondly at a certain coverage the islands size and density reaches the point where the strain fields of neighbouring islands start to overlap noticeably. The islands try to form regular arrays to minimise the extra energy of the overlapping strain fields. A perfect ordering is not always possible because it might be necessary to move a large number of atoms or even fully dissolve a complete island which is at an unfavourable position. As a consequence the arrangement of the islands is a local effect and on a large surface many areas with good but not perfectly matching ordering can be found. Finally with still higher coverage depending on the growth conditions two different evolutions can be found. Either most of the atoms stay in the first layer and the islands merge together and form clusters or many atoms move to higher layers to build three dimensional quantum dots.

III.5 Discussion

III.5.1 Comparison with experimental results

Because of the general type of the model the comparison with experimental results will be mostly qualitative. First we will have a look on the spatial arrangement of the quantum dots. In [27] the surface structure of the InAs/GaAs(100) system is presented in a couple of transmission electron microscopy (TEM) images which show areas where the quantum dots are nicely ordered in a square lattice oriented along the [100] and [010] directions as shown in figure I.1. The same authors show in [140] in a so-called nearest neighbour diagram that the preferred structure is a square lattice, although there are disturbances. All this agrees well with our Monte Carlo results.

In [141] the influence of the flux on the diameter of the quantum dots in a Ge/Si(100) system was studied. By a variation of the flux of Ge atom of about one order of magnitude (0.025Å$/s$–0.2Å$/s$) the diameter of the dots changed by about 30% ($275nm$–$180nm$). This tendency can be seen in figure III.13 where, e.g., for $T = 800K$ the maximum of the size distribution moves from 13 to 11 to 8.5 while the flux is increased from $0.01Ml/s$ to $0.1Ml/s$ to $1.0Ml/s$.

Most experimental papers demonstrate the sharp size distribution of the quantum dots with a sharp line in the photo-luminescence (PL) spectra see, e.g., [142, 143]. In [144] nevertheless size distributions for different coverages are shown for an InAs/GaAs(100)

system. They show a strong peak for low coverage ($1.6Ml$ including the wetting layer) which becomes broader and smaller with increasing coverage (up to $1.9Ml$). The same tendency can be seen if we compare the size distributions in figure III.10, III.13, III.16 and III.20. One has to keep in mind that our model assumes a passive wetting layer which is already present when comparing that coverages with experimental data. This means that at least one monolayer has to be added to our coverage values. Another result from [144] is the decreasing diameter of the quantum dots when the coverage is increased. In the Monte Carlo simulations we have found the opposite trend. The reason for this difference can be obtained by a comparison of the surface structures, or to be more precise, by the comparison of the island densities. In the experimental system only very few islands can be found while in the Monte Carlo simulation a large number of islands emerge even for low coverage. The critical size, i.e. the minimal size an island has to reach to survive on the surface is smaller in the Monte Carlo simulation than in the InAs/GaAs(100) system in [144]. As a result in the Monte Carlo simulation more islands can be found at an early stage of growth; given the total number of atoms on the surface, consequently they will be smaller than in the experiment. If we try to change the critical island size in the Monte Carlo simulation, e.g., by reducing the pair-binding energy a trend similar to [144] can be expected.

III.5.2 Limitations of the model

It has been shown in experiments that the size of the quantum dots increases with the temperature independently of the material system, see e.g., [141] for Ge/Si(100) or [145] for InGaAs/GaAs(001). For systems with no strain, e.g., in homo-epitaxy, this can also be found in Monte Carlo simulation [25], but in the simulation presented here no significant change of the islands size with temperature can be observed. Because the general trend of increasing island sizes without strain is completely compensated by the phenomenological strain correction term E_c which we have introduced in equation (III.3). This is another indication that the phenomenological strain correction term is only a qualitative description of the underlying physical system. In very recent work Meixner and Shchukin have substituted the phenomenological term by a solution of the elasticity problem based on a Green's function approach. In simulations of growth interruptions of some 1000 s they could confirm the analytic results of [146] with a Monte Carlo simulation. These results demonstrate that the missing temperature dependence of the islands size is not a general problem of the Monte Carlo approach but only due to simplified model of the strain.

III.6 Comparison with other approaches

III.6.1 Other stochastic Methods

Besides the Monte Carlo method, there are other methods based on the random selection of a certain event. One is the method of Cellular Automata [147, 148, 149]. The idea behind Cellular Automata is to reduce a continuous spatial domain to a simple discrete grid and allow only integer values of the variables on the grid points in addition to discrete timesteps. This would perfectly match our problem and show no difference to the assumptions made in the previous chapter. However, starting with an initial configuration the new configuration after a time step Δt is calculated by evaluating all grid points and calculating their new values. This is a very inefficient way for tackling our problem because the probabilities for moving or depositing ad-atoms are very small. This means that at each time step only very few grid points will change their values. When trying to optimise this situation one probably will end up with a similar event-based solution as described above.

Another stochastic method, quasi-particle Brownian motion, which is in principle very similar to the Monte Carlo method described above, was developed for a special class of coupled partial differential equations of reaction diffusion type, the so called Activator-Inhibitor equations as discussed in chapter II [150, 151]. These equations are used to describe complex chemical reaction as well as charge carrier transport and generation in semiconductors, like in the previous chapter, or to describe biological predator-prey scenarios. The idea behind this integration method is best described by a chemical example. To derive the partial differential equations for a chemical reaction like

$$A + B \leftrightarrows AB \tag{III.8}$$

concentrations $c_A(\vec{r})$, $c_B(\vec{r})$ and $c_{AB}(\vec{r})$ are introduced and their time-evolution is given by partial differential equations. The stochastic methods go back to the level of single particles. Depending on the number of particles of different species in a given area the new numbers of particles in this cell are calculated. Also the diffusion into neighbouring cells and back is taken into account. This may lead to very efficient and fast algorithms, but the drawback for the integration of partial differential equations is, that noise is always involved, which makes, e.g., the study of repelling objects much more difficult. Also the time steps are not equally spaced, which prevents the application of some standard techniques of time series analysis.

III.6.2 Other kinetic Monte Carlo growth simulation

As mentioned before there are a couple of different Monte Carlo schemes which address a similar topic. In this section we would like to discuss and compare these to the one

developed in this work.

Pioneering work in the field of Monte Carlo simulation of strained hetero-epitaxy was done by Ghaisas and Madhukar [152, 153]. They studied the influence of strain in general and found a tendency towards the occurrence of 3-dimensional surface morphologies under compressive in-plane strain [154]. In [155] the processes which are necessary for a lateral and also a vertical self-organization of islands where discussed in general but unfortunately no results of simulations were presented.

Ratsch et al. [156] have presented studies for the growth of metals, namely Al (aluminium) on Al(111). They show nicely ordered islands with about the same size and they do not use any strain effects at all, because they considered homo-epitaxy. The reason is the very short mean free path of the ad-atoms in this type of system, because they assumed a temperature (50-250 K) which is very low, compared to growth temperatures of semiconductor systems. Additionally they assumed that dimers will not dissociate, because of their high binding energy. Because of this very short mean free path every island has a certain "attraction" area around itself, i.e. every ad-atom in this area will move to the island in the centre. Assuming a homogeneous deposition it is easy to see that this will lead to a situation where islands of similar size are organised in hexagons.

In semiconductor systems which are the focus of this work the mean free path is much larger than the observed distances between the dots. This means that the explanation for the metal on metal growth will not hold for this system.

Ratsch et al. [130, 131] have included strain effects in their simulation of hetero-epitaxy. They introduced the strain as an extra energy at the boundary of each island. But, in contrast to our model they did not include strain-effects further away from the island. As a result they find a sharp size distribution but the spatial ordering is not too well reproduced. As another result they show that when the flux to the surface is shut off, after a very long time the islands cluster together and form one big island. For the sharp size distribution the same argument as for the system presented here is valid. The long time behaviour might have the following explanation. When there are large islands with only a small distance in between, two islands might eventually collide forming one island. In this bigger island the boundary strain is higher and consequently more atoms will separate from the island and move to some other islands. After a while all islands will have about the same size again but there will be one island less. Now this process might repeat again when two islands collide eventually. This is not likely to happen in our model because of the repulsive character of the strain induced island – island interaction. It is not easy to tell which long time scenario might be the right one, but the regular array of equally sized islands is at least a very strong local minimum of the free energy. A large flat island might have a lower energy but we think it might be only reached by passing several very high potential barriers taking a much longer time than seems to be relevant under experimental condition. Especially if one takes into account that the quantum dots are often overgrown with substrate material shortly after deposition.

An approach, similar to the one presented here, was adopted by Barabási [157]. He focused on the study of the size-distribution of the quantum dots in a one-dimensional Monte Carlo simulation. The effects of the strain field were included by a method proposed in [158] where the interaction potential of nearest neighbours is assumed to be harmonic. With this approach it was shown that a sharp size distribution can be achieved with a lattice mismatch larger than 5%. Although a different strain field was used we can compare the size of the energy term which is necessary to stop the growth of a single islands. In [157] and also in our studies this energy was found to be about 70% of the binding energy to a single atom. Also a two-dimensional study was presented by the authors [159], but on patterned surfaces, i.e. the seeds for the nucleation of islands were already on the surface. Because of the reduced dimension in [157] and the imposed structure in [159] no statements on the self-organised spatial organization of the quantum dots could be made.

Strain effects may also play an important role in surfactant-mediated epitaxial growth. In [160] a Monte Carlo based study was presented to explain the growth of Ge on Si(111) with lead (Pb) as a surfactant [161, 162]. The simulations could explain quite well the unusual fractal-to-compact island transition which was induced by lowering the temperature or by increasing the deposition flux. But the experiment also show a transition by varying the coverage which so far could not be explained by the simulations. Here the authors of [160] assume strain effects may become important [163].

In [164] the formation of quantum dots on misoriented surfaces was studied experimentally and a Monte Carlo simulation of the growth of the misoriented substrate was presented. Also here no strain effects were included because the simulation was only done for the growth of the substrate which is homo-epitaxy.

III.6.3 Other theoretical studies of quantum dots

Besides kinetic Monte Carlo Simulations we now want to discuss other theoretical approaches for the description of quantum dots. The first one will be the studies of Shchukin et al. [118, 165] which see the regular array of equally sized quantum dots as the thermodynamic equilibrium configuration in strained hetero-epitaxy. An extension to this method was presented by Wang et al. [166] where the wetting layer was covered in more detail. In the following section we will shortly discuss a model which is based on rate equations[167] and other dynamic approaches.

To find the minimum of the free energy Shchukin et al. considered the contribution to the free energy. The most important ones in this system are the surface energy E_{surf} and the energy due to strain effects E_{strain}. The larger the islands the larger is the area where the islands are nearly free of strain. On the other hand the surface energy is larger. This will lead to an optimal size of the island. In this calculation not only the surface of the islands must be taken into account, also the covered surface of the wetting layer has to be considered. In the context of these studies the properties of the wetting layer

were studied and as a result one can say that the wetting layer does not behave like an ordinary surface of an ad-atom crystal, but has to be considered as a separate material.

A regular square array of equally sized quantum dots is as these studies show the configuration with the lowest free energy. But there are certain questions which arise. No entropy effects are included, i.e. the studies assume zero temperature. Quantum dots are grown at several hundred Kelvin and it is highly expectable that these temperatures will have great influence on the growth process. In the framework of the thermodynamic studies, only regular configurations could be compared, i.e. only regular arrays of islands where all islands have the same size. How a broader size distribution, or randomly arranged dots will influence the free energy could not be answered. As a last point we want to address a dynamic aspect. Even if a regular array of equally sized dots is the minimum of the free energy it is not clear how a system under growth conditions can reach the thermodynamic equilibrium. There must be a dynamic process which can guide the system to the thermodynamic equilibrium, because it is highly improbable that a fully grown quantum dot can move its centre of mass considerably.

Recently Shchukin published a study on the growth of two-dimensional islands where also entropy effects were included [146]. As we have explained earlier these two-dimensional islands are the fundaments of the quantum dots. He found that the temperature dependence of the island size is different in a purely kinetic and in a purely thermodynamic theory. Meixner and Shchukin are currently trying to support this work with results of a kinetic Monte Carlo simulation similar to the one presented here.

Other thermodynamic equilibrium studies were done by Daruka and Barabási [119, 120] and by Wang et al. [166]. As an addition to the work of Shchukin et al. they included the contribution of the covered and uncovered parts of the wetting layer.

III.6.4 Rate equations and other dynamical approaches

Dobbs et al. [167] developed a method based on rate equations to explain the sharp size distribution of quantum dots. The main idea is that the strain destabilises the boundary of an island. They introduced densities of islands of a certain size and assigned a higher rate to decay for larger islands. As a result they obtained a size-distribution which compares well to experimental data. But this method only explains the size-distribution and gives no information on possible patterns on the surface.

The evolution of two dimensional islands and the influence of growth interruption was studied in [168] and [169], respectively. In this approach the time evolution of the concentration of ad-atoms on the crystal surface is described by differential equations. However, no strain effects were included and consequently Ostwald ripening was the dominating process leading to a smoothing of the surface during the growth interruption.

III.6.5 Thermodynamic versus kinetic effects

Over the last years there was much discussion about whether the self-organised growth of quantum dots is dominated by kinetic effects or by the thermodynamic equilibrium and consequently about a proper theoretical description. Some of the used models were presented and compared in the previous sections. We are of the opinion that both views are important and that only the external growth conditions can favour kinetic or thermodynamic processes, but the other cannot be neglected. The Monte Carlo simulations have shown that in the early stages, especially when the flux is still on and the system is far from the thermodynamic equilibrium, the kinetic processes dominate. But when the flux is shut off the system tries to find a way towards the equilibrium. Depending on the flux rate, the growth temperature and the duration of the growth interruptions each of the two phases can be more or less important. However the kinetic phase is always the first and during this phase the basis for the future structure is formed. During the thermodynamic phase the system tries to evolve towards the thermodynamic equilibrium, but as we can see in the Monte Carlo simulations presented here, the system can come close to the equilibrium only if the basis has a reasonable structure, i.e. is not too far away from the equilibrium. Recent thermodynamic studies by Shchukin [146] share this view and consider equilibrium growth conditions, i.e. at zero temperature, as well as kinetic ones, i.e. at finite temperatures. We think that a combination of the analytic results presented in [146] and corresponding Monte Carlo simulations may provide a deep insight in the early stages of quantum dot growth.

IV: Reflectance Anisotropy Spectroscopy

In the previous chapter we were led by the assumption that the surface of a semiconductor can be seen as a homogeneous flat surface. In this chapter we will see that this is not true but that semiconductor surfaces have a structure which can be analysed in experiments and can also be calculated. The same is true for interfaces of two different semiconductor materials [57].

To construct a surface we take an infinite semiconductor bulk and cut it along a plane into two pieces. Now we have a semi-infinite semiconductor with a surface. Depending on the cutting plane we get different kind of surfaces which are labelled with the vector perpendicular to the surface, i.e. the normal vector, like e.g. $[001]$ or $[111]$. This is also an experimental method to get a well defined surface. A semiconductor crystal is taken and cut at a lattice plane into two pieces.

But now the following problem arises. If we assume a simple Zinc-Blende structure which is the most common one for group IV semiconductors and also for III-V compounds, in the bulk every semiconductor atom has four next nearest neighbours and forms covalent bonds with them. The atoms on the surface in general have only two next nearest neighbours and two dangling bonds. To get rid of these the surface atoms have to look for other atoms with dangling bonds. The easiest way is to form a bond with a nearby surface atom. To do this the two atoms have to move closer to each other but cannot move too far because they have to keep their two other bonds intact. In diamond or zinc-blende lattice the binding orbitals of an atom are often sp^3 hybrid orbitals, i.e. a linear combination of an s- and 3 p-orbitals. The angle between two sp^3 hybrid orbitals is fixed and responsible for the typical tetrahedral structure of the bulk crystal. If two surface atoms move closer to each other it may turn out that the sp^3 hybridization is energetically unfavourable and three sp^2-orbitals and a single p-orbital, two sp- and two p-orbitals or even one s- and three p-orbitals are more favourable. This process is often called dehybridization. As a result the surface will consist of pairs of atoms, the so called dimers, which have a filled pair of orbitals forming the bond between the two atoms, a pair of unsaturated or dangling bonds and, of course, the filled binding

orbitals to the atomic layer below the surface. The surface is now called a reconstructed surface. Because a surface cell is two times larger than a bulk cell it is called a (2×1) reconstruction. The dimers in this example are called symmetric dimers if the two atoms are lying on a line parallel to the surface. It is also possible that the line connecting the atoms is not parallel to the surface and one atom is a bit higher than the other, these are called asymmetric dimers. Because there are two possible ways of orientation for an asymmetric dimer the surface cell might become larger for these dimers. What type of reconstruction a real crystal will show is not easy to tell. With the help of ab initio calculation one can try to find the surface which has the lowest free energy and should be the most favourable one from an energetic point of view. But in general more than one surface reconstruction can be observed for a specific material and a given direction of the surface depending on the preparation of the surface. For example in compounds the stoichiometry, i.e. the ratio of cations and anions, is important. To find out which reconstructions might be present and which one might be the dominating one, one can think of different experimental methods.

One may be the Scanning Tunnelling Microscopy (STM). With this method the structure of the filled or empty atomic orbitals of a surface can be measured directly, but because of the atomic scale only a very small part of the surface can be investigated.

Another way may be the study of the optical properties of the surface with the help of the Reflectance Anisotropy Spectroscopy (RAS). The technique is based on measuring the difference in normal-incidence reflectance for two different linear polarization directions as a function of the light's energy. With this method the surface is studied as a whole and all information about the surface is summed up in the measured spectrum. The shape of this structure, i.e. the position and the sign of peaks, is in general not known and has to be calculated. Another similar optical method is spectroscopic ellipsometry (SE), which, e.g., makes it possible to measure the thickness of layers and the composition of compound semiconductors [170], but here we will concentrate on RAS. A recent review about what is possible with RAS and SE can be found in [170]. Another important aspect of RAS and also of SE is the possibility to use them *in-situ*, i.e. during the grow process to monitor the progress and the quality of the grown sample [171]. For this reason both methods are used to monitor quantum-dot growth [172] as has been described in the previous chapter.

In the following we will give a short introduction into the theory of the optical response of a semiconductor surface. An comprehensive introduction can be found in [173]. Reports about recent progress in this field can be found in [174, 175, 176, 177]. It will turn out that it is necessary to calculate electron eigenstates and eigenvalues. For this we will use a tight-binding scheme. We will give a short summary on this technique, too. More general introductions can be found in [57, 178].

IV.1 Theory for RAS

Instead of reproducing the complete derivation of the relevant equations to describe the reflectivity of a polarised electro-magnetic wave at a semiconductor surface we will present here a historical survey to illustrate the steps that where necessary to find a description of the interface which respects all anisotropic and non-local properties.

In 1822 Fresnel developed a theory to describe the reflection of light leading to the so called Fresnel formulas [179] without knowing its electro-magnetic character. He considered an abrupt change in the optical thickness, i.e. the refractive index n jumps. The refractive index n is related to the dielectric constant ϵ, which connects the electric field $\vec{E}$ and the electric displacement $\vec{D}$ in Maxwell's equation, by $n = \sqrt{\epsilon}$. This is illustrated in figure IV.1a) where ϵ jumps form its vacuum value ϵ_v to the bulk value ϵ_b of the specific material. As a summary we can say that the Fresnel formulas are local, isotropic, homogeneous and do not include any surface effects.

To include surface effect the theory has to be non-local, because the component for the electric field $\vec{E}$ normal to the surface E_z undergoes a sudden variation at the interface. It has to be inhomogeneous, because the surface separates two different media. And an anisotropy may be present, e.g., as a consequence of a particular reconstruction. Putting all aspects together we have to use a constitutive relation which relates the components of the vector of the electric field E_i with the components of the electric displacement D_i given by

$$D_i(\vec{r},\omega) = \sum_{j=1}^{3} \int d^3\vec{r}' \epsilon_{ij}(\vec{r},\vec{r}',\omega) E_j(\vec{r}',\omega), \tag{IV.1}$$

where ω is given by the frequency of the electromagnetic plane-wave, i and j label the three spatial dimensions and the ϵ_{ij} are the components of the dielectric tensor.

A first step to a more complete theory was done by McIntyre and Aspnes in 1971 [180]. They introduced a surface layer with a depth d and a dielectric constant ϵ_s as shown in figure IV.1b). This model still neglects the nonlocality and the anisotropy but approximates the inhomogeneity by a two-step function. With an expansion up to the first order in $(\omega/c)d$ [1] they could show that their results reproduce Fresnel formulas in the zero-order term, which contains no surface contribution. The contribution of the surface can be found in the first order term which can be seen as a relative deviation from Fresnel formulas and is given by

$$\frac{\Delta R_s}{R_s} = 4(\omega/c)d\cos(\theta)\mathrm{Im}\left\{\left(\frac{\epsilon_s(\omega)-\epsilon_b(\omega)}{\epsilon_b(\omega)-1}\right)\right\} \tag{IV.2}$$

[1] $(\omega/c)d$ is of the order $1/100$ for visible and ultraviolet light when d is in the order of a few Angstroms

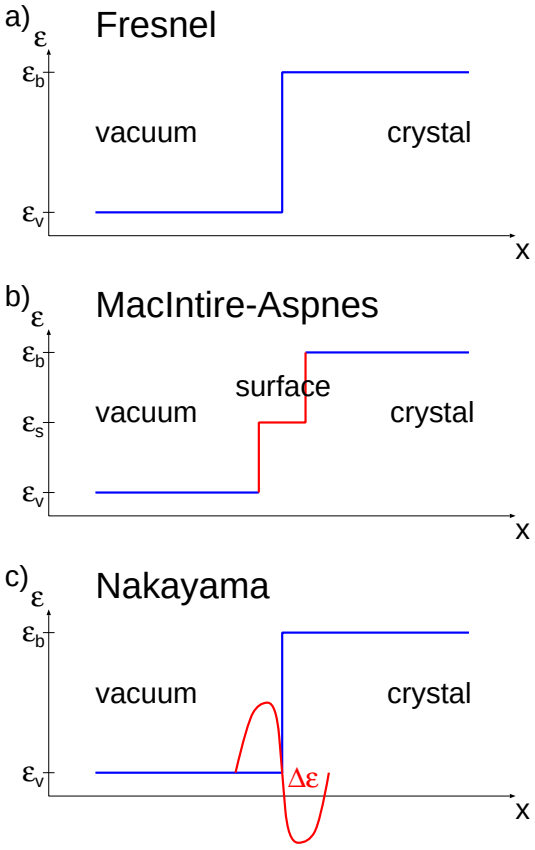

Figure IV.1: Different ways to model the dielectric constant ϵ at an interface. a) abrupt jump from the vacuum value ϵ_v to the bulk value ϵ_b. b) in [180] a surface layer of depth d and a dielectric constant ϵ_s was introduced. c) the surface is treated as perturbation $\Delta\epsilon$ in [181]

for s-light and

$$\frac{\Delta R_p}{R_p} = 4(\omega/c)d\cos(\theta)\times \times \mathrm{Im}\left\{\left(\frac{(\epsilon_b(\omega)-\sin^2(\theta))(\epsilon_s(\omega)-\epsilon_b(\omega))+\epsilon_b^2(\omega)\sin^2(\theta)(\epsilon_s^{-1}(\omega)-\epsilon_b^{-1}(\omega))}{(\epsilon_b(\omega)-1)(\epsilon_b\cos^2(\theta)-\sin^2(\theta))}\right)\right\} \quad \text{(IV.3)}$$

for p-light. The angle of incidence is denoted by θ. The difference between s-light and p-light is the direction of polarization. S-light is polarised perpendicular to the plane of incidence, i.e. parallel to the surface (in the following we will assume that it is polarised in the y direction), while p-light is polarised within the plane of incidence, i.e. the electric field has a component normal to the surface (in the following we will assume that it is polarised in the x-z plane). In RAS only s-light is present but for completeness we give here the formulas for p-light, too.

In 1975 Nakayama [181] tried a perturbative approach to model the dielectric tensor

$$\epsilon_{ij}(z,z',\omega) = \delta_{ij}\delta(z-z')\epsilon_0(z,\omega) + \Delta\epsilon_{ij}(z,z',\omega), \quad \text{(IV.4)}$$

with

$$\epsilon_0(z,\omega) \equiv \theta(-z) + \epsilon_b\theta(z) \quad \text{(IV.5)}$$

where the first term on the right hand side of equation (IV.4) describes the abrupt transition from bulk to vacuum of the Fresnel model while the surface effects can be found in the second term $\Delta\epsilon_{ij}(z, z', \omega)$. If this term can be seen as a small perturbation the light-propagation equations can be solved by using Green's function theory. As a result the following formulas for the surface contribution to the reflectance are given by

$$\left(\frac{\Delta R_s}{R_s}\right)^{\text{pert}} = 4(\omega/c)d\cos(\theta)\text{Im}\left\{\left(\frac{\Delta\epsilon_{yy}(\omega)}{\epsilon_b(\omega)-1}\right)\right\} \tag{IV.6}$$

for s-light and

$$\left(\frac{\Delta R_p}{R_p}\right)^{\text{pert}} = 4(\omega/c)d\cos(\theta)\text{Im}\left\{\left(\frac{(\epsilon_b(\omega)-\sin^2(\theta))\Delta\epsilon_{xx}(\omega)-\sin^2(\theta)\Delta\epsilon_{zz}(\omega)}{(\epsilon_b(\omega)-1)(\epsilon_b\cos^2(\theta)-\sin^2(\theta))}\right)\right\} \tag{IV.7}$$

for p-light with

$$\Delta\epsilon_{ii} = \int dz \int dz' \Delta\epsilon_{ii}(z, z'). \tag{IV.8}$$

It is questionable if $\Delta\epsilon_{ji}(z, z', \omega)$ can always be treated as a small perturbation, because near the surface it is as large as ϵ_b. However, the reliability of the perturbative formulas can be tested. If the microscopic dielectric tensor behaves as in the model of McIntyre and Aspnes equations (IV.2) and (IV.4) should be recovered from equations (IV.6) and (IV.7), respectively. In the case of s-light this is possible, but for p-light this is not the case. This difference can be explained, because the light-propagation equations contain the electric field $\vec{E}$. Classically the parallel components of the electric field (E_x and E_y in our notation) are continuous at a Fresnel-like interface while the normal component (E_z) is not continuous which is illustrated in figure IV.2. The perturbative approach does not hold for the normal component. This observation gave a hint for the development of a reliable theory for p-light, too.

Bagchi et. al [182] used a perturbative approach for quantities which are continuous at the abrupt interface, namely the parallel components of the electric field E_x and E_y and the normal component of the electric displacement D_z which substitutes E_z. They obtained a solution which is rigorously valid up to the first order in $(\omega/c)d$, where d is the thickness of the area where $\Delta\epsilon_{ij}(z, z', \omega)$ is considerably different from zero. Although this was done to calculate the optical properties of a semi-infinite electron gas, i.e. the surface of simple metals, the resulting formulas could be applied for real crystals if their greater anisotropy is included. This was done in 1981 by Del Sole [183] and the resulting reflection coefficients are

$$\left(\frac{\Delta R_s}{R_s}\right) = 4(\omega/c)d\cos(\theta)\text{Im}\left\{\left(\frac{\langle\Delta\epsilon_{yy}(\omega)\rangle}{\epsilon_b(\omega)-1}\right)\right\} \tag{IV.9}$$

for s-light and

$$\left(\frac{\Delta R_p}{R_p}\right) = 4(\omega/c)d\cos(\theta)\text{Im}\left\{\left(\frac{(\epsilon_b(\omega)-\sin^2(\theta))\langle\Delta\epsilon_{xx}(\omega)\rangle+\epsilon_b^2\sin^2(\theta)\langle\Delta\epsilon_{zz}^{-1}(\omega)\rangle}{(\epsilon_b(\omega)-1)(\epsilon_b\cos^2(\theta)-\sin^2(\theta))}\right)\right\}$$

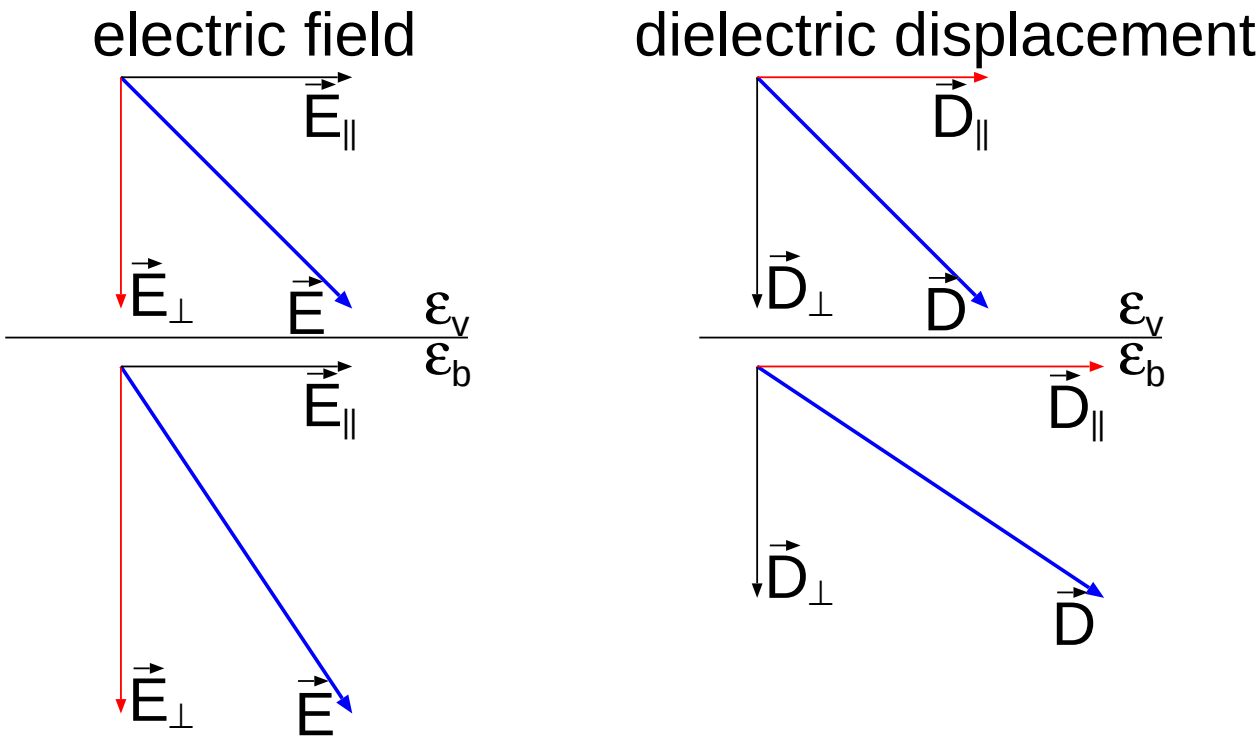

Figure IV.2: The electric field $\vec{E}$ and the dielectric displacement $\vec{D}$ at an interface where the dielectric constant jumps from ϵ_v to ϵ_b. The parallel component of the electric field $\vec{E}_{||}$ and the normal component of the dielectric displacement $\vec{D}_{\perp}$ are continuous while the normal component of the electric field $\vec{E}_{\perp}$ and the parallel component of the dielectric displacement $\vec{D}_{||}$ are not continuous.

(IV.10)

for p-light where

$$\langle \Delta\epsilon_{ii} \rangle = \int dz \int dz' \left(\Delta\epsilon_{ii}(z,z') - \int dz'' \int dz''' \Delta\epsilon_{iz}(z,z') \epsilon_{zz}^{-1}(z',z'' \Delta\epsilon_{zi}(z'',z''') \right) \quad \text{(IV.11)}$$

for $i = x, y$ and

$$\langle \Delta\epsilon_{zz}^{-1} \rangle = \int dz \int dz' \left(\Delta\epsilon_{zz}(z,z',\omega) - \delta(z-z')/\epsilon_0(z,\omega) \right) \quad \text{(IV.12)}$$

contain all surface features. The $\langle \Delta\epsilon_{zz}^{-1} \rangle$ terms are a result of the substitution of E_z by D_z.

Even if we are only interested in s-light it is now necessary to solve the four-fold integral in (IV.11). But luckily the off-diagonal elements in (IV.11) vanish because of the symmetry [173]. This is the case for most low-index surfaces even when reconstructions

are present. And even if the off-diagonal elements do not vanish they are often small so that the four-fold integral in (IV.11) can be neglected. Therefore also the inversion of $\epsilon_{zz}(z, z', \omega)$ is not necessary and the relevant quantities are given by

$$\langle \Delta\epsilon_{ii}(\omega) \rangle = \int dz \int dz' \left(\epsilon_{ii}(z, z', \omega) - \delta(z - z')\epsilon_0(z, \omega) \right) \tag{IV.13}$$

for $i = x, y$, where $\Delta\epsilon_{ii}$ is already substituted with the help of equation (IV.4).

These quantities can now be calculated in terms of electron eigenfunctions and eigenvalues of the semi-infinite crystal. However for optical calculations a slab-geometry is mostly used, because of a reduced numerical effort [173]. The thickness of the slab has to be chosen large enough to minimise the interaction of the two surfaces of the slab. In this geometry $\langle \Delta\epsilon_{ii} \rangle$ $(i = x, y)$ can be substituted by the half-slab polarization

$$4\pi\alpha_{ii}^{\mathrm{hs}}(\omega) = (1/2) \int dz \int dz' \left(\epsilon_{ii}^{\mathrm{slab}}(z, z', \omega) - \delta(z - z') \right). \tag{IV.14}$$

Within the single-particle scheme the imaginary part of the slab polarization is related to the transition probability induced by the radiation between slab eigenstates [184, 185]

$$\mathrm{Im}\left\{ \left(4\pi\alpha_{ii}^{\mathrm{hs}}(\omega) \right) \right\} = \frac{4\pi^2 e^2}{m^2\omega^2 A} \sum_{\vec{k}} \sum_{v,c} |\mathbf{p}_{v,c}^{i}(\vec{k})|^2 \delta(E_c(\vec{k}) - E_v(\vec{k}) - h\omega), \tag{IV.15}$$

where $\mathbf{p}_{v,c}^{i}(\vec{k})$ is the matrix element of the i-th component of the momentum operator between the initial state v (valence) and the final state c (conduction) at the point $\vec{k}$ in the two dimensional Brillouin zone and A is the area of the surface cell. e and m are the charge and the mass of an electron, respectively. The real part of $\alpha_{ii}^{\mathrm{hs}}(\omega)$ can be calculated via the Kramers-Kronig transform [185].

The imaginary part of the bulk dielectric function $\epsilon_b(\omega)$ can be calculated with equation (IV.15), too. Now eigenstates and eigenvalues of the infinite crystal must be used and the $\vec{k}$ vectors are three dimensional. Finally the surface contribution of the reflectivity can be calculated from

$$\left(\frac{\Delta R_s}{R_s} \right) = 4(\omega/c)d\cos(\theta)\mathrm{Im}\left\{ \left(\frac{4\pi\alpha_{ii}^{\mathrm{hs}}(\omega)}{\epsilon_b(\omega) - 1} \right) \right\}, \tag{IV.16}$$

with the eigenstates and eigenvalues of the slab and the infinite crystal as input to calculate $\alpha_{ii}^{\mathrm{hs}}(\omega)$ and $\epsilon_b(\omega)$ according to equation (IV.15). An often used method to find the eigenstates and eigenvalues is presented in the next section.

IV.2 Empirical Tight-Binding Method

All Tight-Binding Methods assume that the eigenfunctions of a polyatomic system $\psi(\vec{x})$ can be constructed by the linear combination of the eigenfunctions of the single atoms

$\phi_a(\vec{x})$. This method is called Linear Combination of Atomic Orbitals (LCAO) and is still a one-electron approach. This method was first used by Slater et al. [186]. We get for the polyatomic wave-function

$$\psi(\vec{x}) = \sum_{a,j} F_{aj}\phi_a(\vec{x} - \vec{R}_j), \tag{IV.17}$$

where F_{aj} are the expansion coefficients and R_j are the positions of the atoms. The $\phi_a(\vec{x})$ do not necessarily have to be atomic wave functions, but can also be hybrid or bonding and anti-bonding orbitals. By putting equation (IV.17) into the one-electron Schrödinger equation

$$H\psi = E\psi \tag{IV.18}$$

we get the following eigenvalue problem for the expansion coefficients F_{aj}

$$\sum_{b,i}[H_{ab}(\vec{R}_j, \vec{R}_i) - ES_{ab}(\vec{R}_j - \vec{R}_i)]F_{bi} = 0, \tag{IV.19}$$

where

$$H_{ab}(\vec{R}_j, \vec{R}_i) = \int d^3\vec{x}\phi_a^\star(\vec{x} - \vec{R}_j)H\phi_b(\vec{x} - \vec{R}_i) \tag{IV.20}$$

are the matrix elements of the one-electron Hamiltonian H of the system and

$$S_{ab}(\vec{R}_j - \vec{R}_i) = \int d^3\vec{x}\phi_a^\star(\vec{x} - \vec{R}_j)\phi_b(\vec{x} - \vec{R}_i) \tag{IV.21}$$

are the inter-atomic overlap integrals.

If one wants to do ab initio calculations the integrals in equation (IV.20) and (IV.21) have to be calculated explicitly for a given H and a given set of $\phi_a(\vec{x})$. This can only be done with large numerical efforts, because in general the matrix elements do not converge rapidly in real space. To overcome this problem Slater and Koster [186] suggested to treat the matrix elements $H_{ab}(\vec{R}_j, \vec{R}_i)$ as parameters to be fitted to reproduce the energy-bands at high-symmetry points. Because they recognised that only at this points accurate solutions were obtainable with other band-structure calculation techniques.

They also used the Löwdin theorem [187] which states that a set of non-orthogonal orbitals located at different atoms can be transformed into a new set of orbitals which are orthogonal to each other and preserve the atomic symmetry. With this new set of orbitals we get

$$S_{ab}(\vec{R}_j - \vec{R}_i) = \delta_{ab}\delta_{ji} \tag{IV.22}$$

With this we can start to set up the Hamiltonian for this system. The calculation of the matrix elements of the Hamiltonian H by fitting them to reproduce the bulk energy-bands were done by Vogl et al. [188] for the group IV and most of the III-V compound semiconductors. They have taken five orbitals for a single atom namely the s-, p_x-, p_y- and p_z-orbitals of the valence shell and an s-like orbital, called $s^\star$, to mimic the d-orbitals. This is necessary the get a good description of the conduction band. They also assumed nearest-neighbour interactions only. The result is the following two-particle Hamiltonian

$$
H(\vec{k}) = \begin{pmatrix}
\epsilon_s^A & 0 & 0 & 0 & 0 \\
0 & \epsilon_p^A & 0 & 0 & 0 \\
0 & 0 & \epsilon_p^A & 0 & 0 \\
0 & 0 & 0 & \epsilon_p^A & 0 \\
0 & 0 & 0 & 0 & \epsilon_{s^\star}^A \\
E_{ss} g_1^\star(\vec{k}) & -\hat{E}_{sp} g_2^\star(\vec{k}) & -\hat{E}_{sp} g_3^\star(\vec{k}) & -\hat{E}_{sp} g_4^\star(\vec{k}) & 0 \\
E_{sp} g_2^\star(\vec{k}) & E_{xx} g_1^\star(\vec{k}) & E_{xy} g_4^\star(\vec{k}) & E_{xy} g_3^\star(\vec{k}) & E_{s^\star p} g_2(\vec{k}) \\
E_{sp} g_3^\star(\vec{k}) & E_{xy} g_4^\star(\vec{k}) & E_{xx} g_1^\star(\vec{k}) & E_{xy} g_2^\star(\vec{k}) & E_{s^\star p} g_3(\vec{k}) \\
E_{sp} g_4^\star(\vec{k}) & E_{xy} g_3^\star(\vec{k}) & E_{xy} g_2^\star(\vec{k}) & E_{xx} g_1^\star(\vec{k}) & E_{s^\star p} g_4(\vec{k}) \\
0 & -\hat{E}_{ps^\star} g_2^\star(\vec{k}) & -\hat{E}_{ps^\star} g_3^\star(\vec{k}) & -\hat{E}_{ps^\star} g_4^\star(\vec{k}) & E_{s^\star s^\star} g_1^\star(\vec{k})
\end{pmatrix} \cdots
$$

$$
\cdots \begin{pmatrix}
E_{ss} g_1(\vec{k}) & E_{sp} g_2(\vec{k}) & E_{sp} g_3(\vec{k}) & E_{sp} g_4(\vec{k}) & 0 \\
-\hat{E}_{sp} g_2(\vec{k}) & E_{xx} g_1(\vec{k}) & E_{xy} g_4(\vec{k}) & E_{xy} g_3(\vec{k}) & -\hat{E}_{ps^\star} g_2(\vec{k}) \\
-\hat{E}_{sp} g_3(\vec{k}) & E_{xy} g_4(\vec{k}) & E_{xx} g_1(\vec{k}) & E_{xy} g_2(\vec{k}) & \hat{E}_{ps^\star} g_3(\vec{k}) \\
-\hat{E}_{sp} g_4(\vec{k}) & E_{xy} g_3(\vec{k}) & E_{xy} g_2(\vec{k}) & E_{xx} g_1(\vec{k}) & -\hat{E}_{ps^\star} g_4(\vec{k}) \\
0 & E_{s^\star p} g_2(\vec{k}) & E_{s^\star p} g_3(\vec{k}) & E_{s^\star p} g_4(\vec{k}) & E_{s^\star s^\star} g_1(\vec{k}) \\
\epsilon_s^B & 0 & 0 & 0 & 0 \\
0 & \epsilon_p^B & 0 & 0 & 0 \\
0 & 0 & \epsilon_p^B & 0 & 0 \\
0 & 0 & 0 & \epsilon_p^B & 0 \\
0 & 0 & 0 & 0 & \epsilon_{s^\star}^B
\end{pmatrix} \tag{IV.23}
$$

This will be all for the calculation of bulk systems because of the translation symmetry and the fact the most semiconductors crystals form a face-centred cubic (fcc) lattice. But in our slab geometry we only have the translation symmetry in the x- and y-direction. So we have to set up a larger slab Hamiltonian by labelling all n atoms in the slab. This will give us an $n \times n$ matrix where the diagonal elements ii represent the self-interaction of a single atom i and the off-diagonal elements ij will hold the interaction between atom i and atom j. We assume only nearest-neighbour interaction so most of the off- diagonals will be zero. In the remaining one we place the corresponding 5×5 matrix representing the interaction of the different orbitals like the sub-matrices in the two-particle Hamiltonian (IV.23).

One problem still remains. The fitted matrix elements are only valid if the atoms have their equilibrium distance in the fcc lattice. But at the surface and on the bottom of the slab the atoms are due to the reconstruction not in their equilibrium distance anymore. For these atoms we use the Harrison's d^2-rule [178] which states that if the distance between two atoms is r and their equilibrium distance is r_0 the matrix elements change with the factor $(r/r_0)^2$.

By finding the eigenvalues and eigenvectors of the Hamiltonian for a given point $\vec{k}$ in the two-dimensional surface Brillouin-Zone we get the energies and their corresponding wave-functions. By doing this for a couple of $\vec{k}$-points along certain high symmetry lines we get the energy bands for the surface Brillouin-zone. To distinguish between bulk-levels coming from the core of the slab and energy-levels due to the structure of the surface we introduce a surface zone, e.g. the first two or three layers of the top and of the bottom of the slab, and calculate the probability to find each state in this zone. If the probability is higher than a given number we call this a surface state.

For the diagonalization of the Hamiltonian we use two different implementation of a method using the QR-decomposition. One is the LAPACK [189] implementation which were used whenever optimised versions of BLAS [190] and LAPACK were available.

Coming back to our primary aim to calculate the optical anisotropy we now have the Hamiltonian and its eigenvalues and eigenfunctions. But we need the momentum operator $\mathbf{p}$ to calculate the sum in equation (IV.15). To calculate $\mathbf{p}$ we take the commutator of the Hamiltonian H and the position operator $\mathbf{r}$

$$\mathbf{p} = \mathrm{Im}\left\{[H, \mathbf{r}]\hbar\right\} \tag{IV.24}$$

getting

$$\langle n\vec{R}|\mathbf{p}|n'\vec{R}'\rangle = (i\, m\hbar)\sum_{n''}\Big(\langle n\vec{R}|H|n''\vec{R}'\rangle\langle n''\vec{R}'|\mathbf{r}|n'\vec{R}'\rangle - \langle n\vec{R}|\mathbf{r}|n''\vec{R}\rangle\langle n''\vec{R}|H|n'\vec{R}'\rangle\Big)\,, \tag{IV.25}$$

for the matrix elements of the momentum operator $\mathbf{p}$ where $\vec{R}$ and $\vec{R}'$ are position vectors of the atoms in the slab and n, n' and n'' are labelling the eigenstates. The interatomic matrix elements of the position operator r were neglected, taking into account the orthogonality of the orbitals. Because of the nearest neighbour interaction only a few terms in the sum in (IV.25) are non vanishing. Besides the parameters of the Hamiltonian we need only two more parameters, namely the intra-atomic sp and $s^\star p$ dipoles which were fitted to reproduce at best the bulk dielectric function of silicon: $\langle s_x p_x\rangle = 0.27$Å, and $\langle s_x^\star p_x\rangle = 1.08$Å.

Now we have all the ingredients for the calculation of the optical properties. The imaginary part the polarization $\alpha_{ii}^{\mathrm{hs}}$ has to be calculated for a number of points in the Brillouin-zone. The real part is computed via the Kramers-Kroning transform giving us the surface part of the reflectivity $\Delta R_s/R$. The k- points should be equally distributed

and should not be high symmetry points because the special structure at this points would spoil the averaging.

The calculation of the matrix elements of the momentum operator $\mathbf{p}^i_{v,c}(\vec{k})$ needs most of the computing time. One way to speed this up is to use the fact that most of them are zero. If the position of the non-zero elements is saved when setting up the momentum operator we can calculate the sum over the non-zero elements only and reduce the computational effort from an $O(N^2)$ to an $O(N)$ law.

The last step, because we want to have the anisotropy of the reflectivity, is to compute $\Delta R_s/R$ for the x- and the y- direction by using the x- ($\mathbf{p}^x_{v,c}(\vec{k})$) and the y-component ($\mathbf{p}^y_{v,c}(\vec{k})$) of the momentum operator and to take their difference. The result is the RAS spectrum of the slab.

In the past this method was used successfully for many different materials and surfaces, like the Si(111) (2×1) [191] and the Si(111) (7×7) [192], Ge(001) c(4×2) [193]. Also adsorbate-covered surfaces like GaAs(110)/Sb [194, 195] or InP(110)/Sb [196] and surfaces with one and two layers of Ge on Si(001) [197, 198] were studied with good results.

There are also some improvements to this method published during the last years. In [199, 200] the two most important d-states were used instead of the $s^\star$ to improve the results for energies above 4 eV in GaAs. Shen et al. [201] employed a self-consistent tight-binding method for Si(100)/As. Schmidt et al. [202] substituted the tight-binding method by density functional theory for InP(001). All these approaches yield to some special improvements with the cost of much more numerical effort. For this reason we stay with the "classical" method.

In the following we will have a look on the (001) surface of InP. Quite a number of different reconstructions where proposed for InP(001) and here the corresponding optical spectra according to the theory explained above will be presented. The results are compared with experimental data and finally we try to identify transitions of surface and bulk states which are responsible for some specific features in the spectra.

IV.2.1 Bulk Properties

To calculate the optical properties of a slab we need to know the dielectric function of the bulk. We can calculate it with the same algorithm except that the slab has to be substituted by the elementary cell of the bulk and the now full three dimensional periodicity has to be respected. To get a feeling of the accuracy of the Tight-Binding approach we also calculate the bulk band-structure and compare it with experimental data.

There is an important difference in choosing the k-points for the calculation of the optical properties and the band-structure. For the band-structure we choose some high-symmetry points and a number of points on the line connecting the high-symmetry

points. The optical properties are calculated at points equally distributed over the irreducible part of the Brillouin-zone where high symmetry points are avoided because they would spoil the averaging due to their special structure.

IV.2.2 Surface contributions

With equation (IV.15) the complete optical response of a surface can be calculated as a sum over all possible transitions between conductance and valence band state. To determine which part of the spectrum is dominated by surface transitions and which part is due to bulk transitions we split the spectrum in the following way. We choose a surface part of the slab, i.e., the two top layers. For each eigenstate of the Hamiltonian we calculate the probability to find the electron in this surface area. If this is higher than a given value we label this state as a surface state. This is illustrated in figure IV.3. When we now calculate matrix elements of the momentum operator we can collect all matrix elements where valence and conduction band states are surface states, where both are bulk states and where only the valence or the conduction band state are surface states. As a result we have split the total signal into 4 spectra where only surface-surface, bulk-bulk, surface-bulk or bulk-surface transitions are involved. The sum of these four spectra will again give the complete RA spectrum.

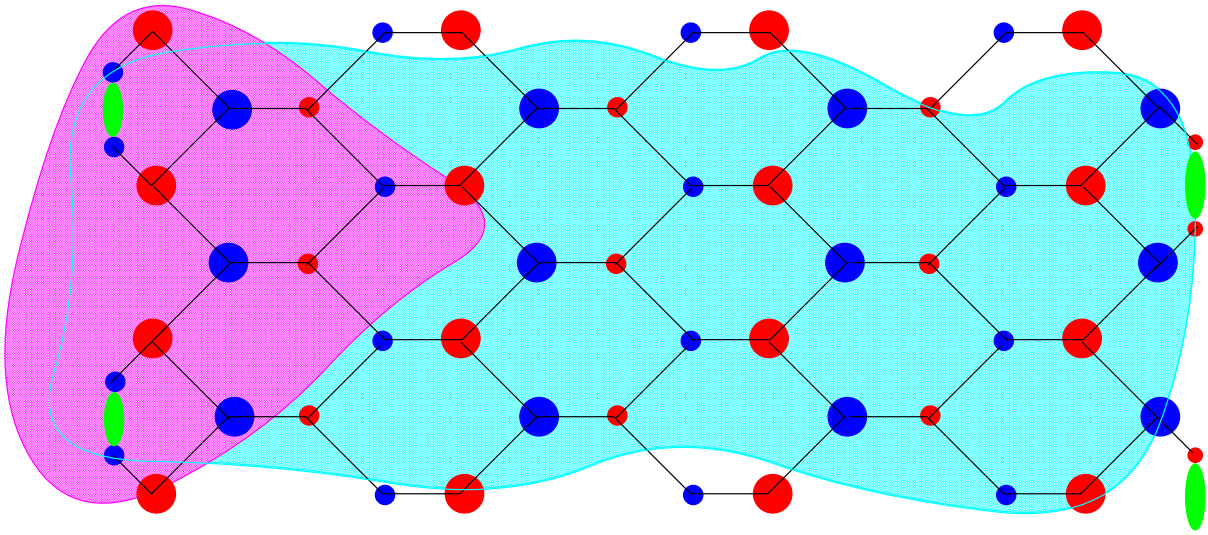

Figure IV.3: A schematic view of a slab and two different states is shown. The shaded areas represents the localization of the two different states. We call the reddish state a surface state, because it is localised mainly at the surface; the bluish one is spread over the whole slab and therefore we call it a bulk state.

By varying the surface area we can get detailed information about the origin of certain properties of the RAS spectrum. It is not necessary that the selected area has to be at the surface, it can be anywhere in the slab.

In this study we only look at the (001) surface. In the following figure IV.4 the unrelaxed surface is shown in a top view and a side view.

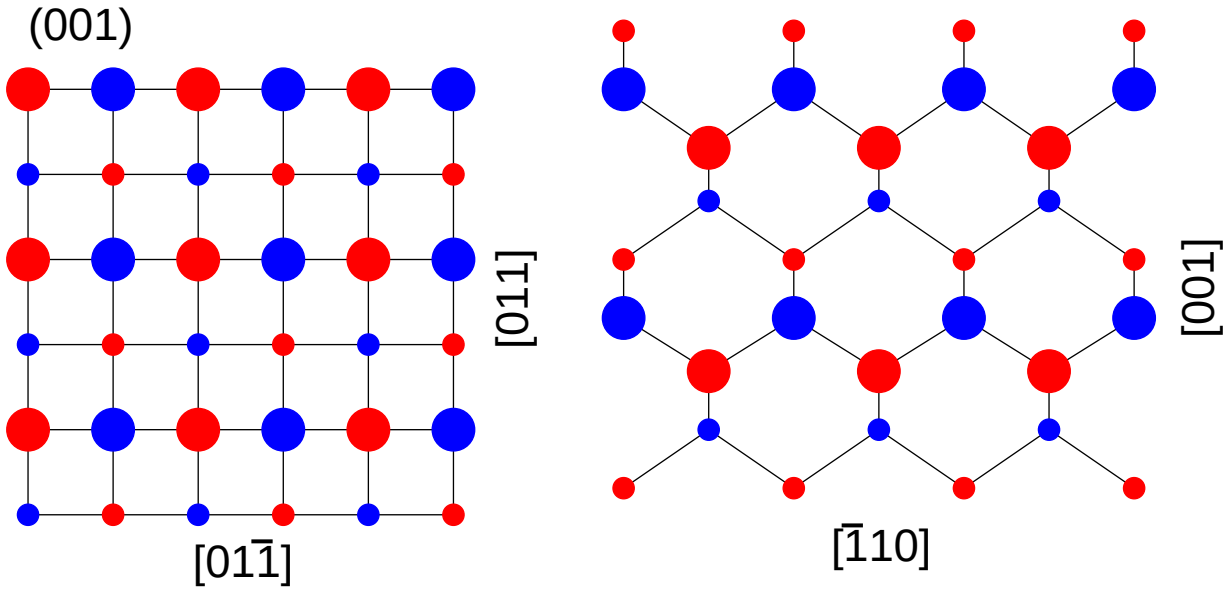

Figure IV.4: The (001) surface in two different views. a) top-view, b) side-view. The colour should distinguish between cations and anions. The large circle represents near atoms, the small ones atoms which are far.

IV.3 InP

The surface structure of InP(001) is under discussion for quite a while. But one point is already clear. In contrast to earlier assumptions the (001) surface of InP has nothing in common with the corresponding GaAs surface which is theoretically and experimentally well understood. A surface phase diagram under MBE condition of different measured reconstructions can be found in [203].

But first we want to look at the bulk properties. A calculated band structure is shown in figure IV.5 and in table IV.1 the calculated band gap at the Γ-point of Brillouin zone is compared to experimental data taken from [204]. Here and even more when we compare the results for surfaces with experimental data one has to keep in mind that the calculations are for $0K$ and most of the experimental data are taken at room temperature or above. For example a change of the energy gap at the Γ-point of nearly 0.1 eV can be observed in table IV.1 when going from 2 K to room temperature (300 K). But for InP also data for very low temperatures are available because of the direct band-gap and compare quite well to the theoretical findings. This is of no great surprise, because the tight-binding parameters were fitted in [188] to the band structure at high-symmetry points.

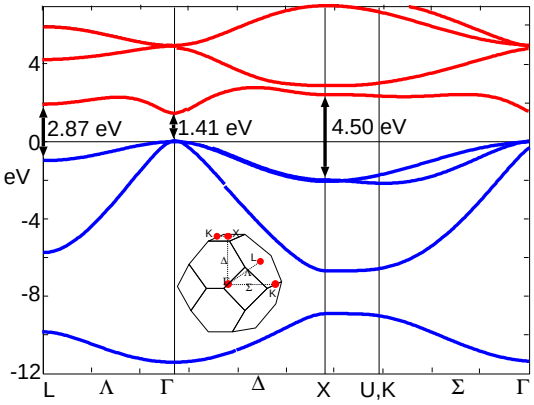

Figure IV.5: The calculated band structure in InP.

temperature [K]	2	4.2	6	77	298	300
energy gap [eV]	1.4236(1)	1.4230(5)	1.4205	1.4135	1.3511	1.34

Table IV.1: Band gaps of InP at the Γ-point measured at different temperatures taken from [204].

For the calculation of the RA spectrum given by equation (IV.16) we need the dielectric function of the bulk $\epsilon_b(\omega)$. This is plotted in the next figure IV.6 together with an experimental curve measured by ellipsometry [205] taken from [206] with kind permission of the authors. The calculated dielectric function is shifted slightly to higher energies, which can be explained by the finite temperature at which the experimental data were taken. In [206] a shift to higher energies with decreasing temperatures was reported. There is also an excitonic contribution near 3 eV [207, 208] which is out of scoop of the tight-binding scheme used here. Besides this the comparison is quite good.

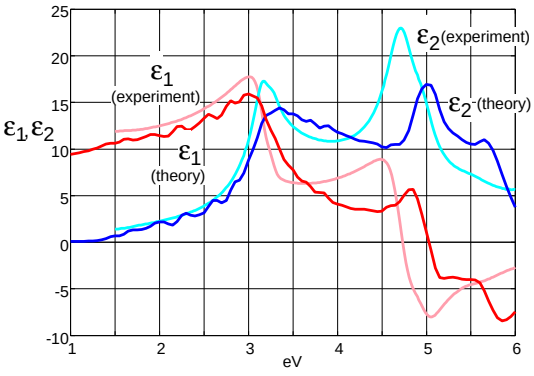

Figure IV.6: The dielectric function of InP. The experimental curves are taken from [206].

But now back to the surface. There is a whole bunch of different structures proposed for the InP(001)-(2×4) surface. Also (4×2) [209, 210] reconstructions were reported but could not be confirmed by more recent experiments [211, 212]. In the following we will discuss the proposed structures for the (2×4) reconstruction.

The first two structures in figure IV.7, the $\beta 2(2\times4)$ and the $\alpha(2\times4)$ are proposed by Ozanyan et al. [203] because they attribute the anisotropy to cation and anion dimers on the surface similar as on the As-rich GaAs(001) surface. Based on STM studies MacPher-

son et al. [211] suggested a reconstruction with an P-trimer (figure IV.7c)) in the topmost layer while In-trimers were found by Sung et al. [209] by time-of-flight scattering and recoiling spectrometry. A family of dimer structures were presented in [213]. In the top-layer a In dimer in [110] direction or single In or P dimer pointing in the $[\bar{1}10]$ direction which is in the centre of the surface cell were proposed. There is also a fourth member in this family where the dimer is an In-P pair. This structure was included to meet the anisotropy visible in the STM picture by MacPherson et al. [211].

Now we have the topologies of 8 different structures which are plotted in figure IV.7, but we need the exact positions of the surface atoms. These position can be found by minimising the total energy of the surface. It is possible to do this in the framework of Tight-Binding formalism, but here we will use data achieved by Density Functional Theory (DFT). Gero Schmidt has calculated the total energy of all the structures discussed above and provided us kindly with all the necessary position data [214, 215]. In this DFT scheme the positions of the atoms of the 4 topmost layers are variable and the positions of the atoms in the fifth layer are fixed to the bulk positions. To get a slab of 20 or more layers we now extend the surface data by adding bulk layers. We will take only slabs which have a number of layers which is a multiple of four, because this is the period in the [001] direction. The [001] direction is a polar direction, i.e. in one layer only cations can be found while in the neighbouring layers only anions can be found. If we now start to build our slab with, e.g., a cation layer it is easy to see that we run into trouble on the back surface, because this will always be an anion layer, because of the period of four. This means we will never get a back surface which is equivalent to the surface we want to study. To eliminate the effects of the back surface we use a linear cut-off function when we build the Hamiltonian. But to keep the slab neutral we have to use the same number of cation and anions. One of the simplest way to achieve this is to put the surface structure to the back surface and switch the type of the atoms. Then the back surface if unphysical but will do no harm, because of the cut-off function. If not mentioned otherwise a slab with 20 layers of atoms is used for the calculation of the RA spectra.

Besides the position data the DFT [214, 213] calculations reveal the total energy of all the different structures for different chemical potentials μ. These results can be summarised in the following way. The structures with the lowest energy are the $\beta 2$ for P-rich conditions and the mixed-dimer surface for an In-rich environment. The energy of the proposed (4×2) surface-reconstructions was calculated in [214] and [213], too, but their energy is under all conditions more than 0.2eV larger compared to the (2×4) reconstructions with the lowest energy.

Now we have all needed ingredients and in the following figure IV.8 for all 8 structures shown in figure IV.7 the calculated RA-spectrum is shown. In the next figure IV.9 two experimental results can be found. A spectrum taken a room temperature is shown in figure IV.9a). The data was published in [216] and was kindly contributed by the authors. Figure IV.9 was taken from [203] with kind permission of the authors.

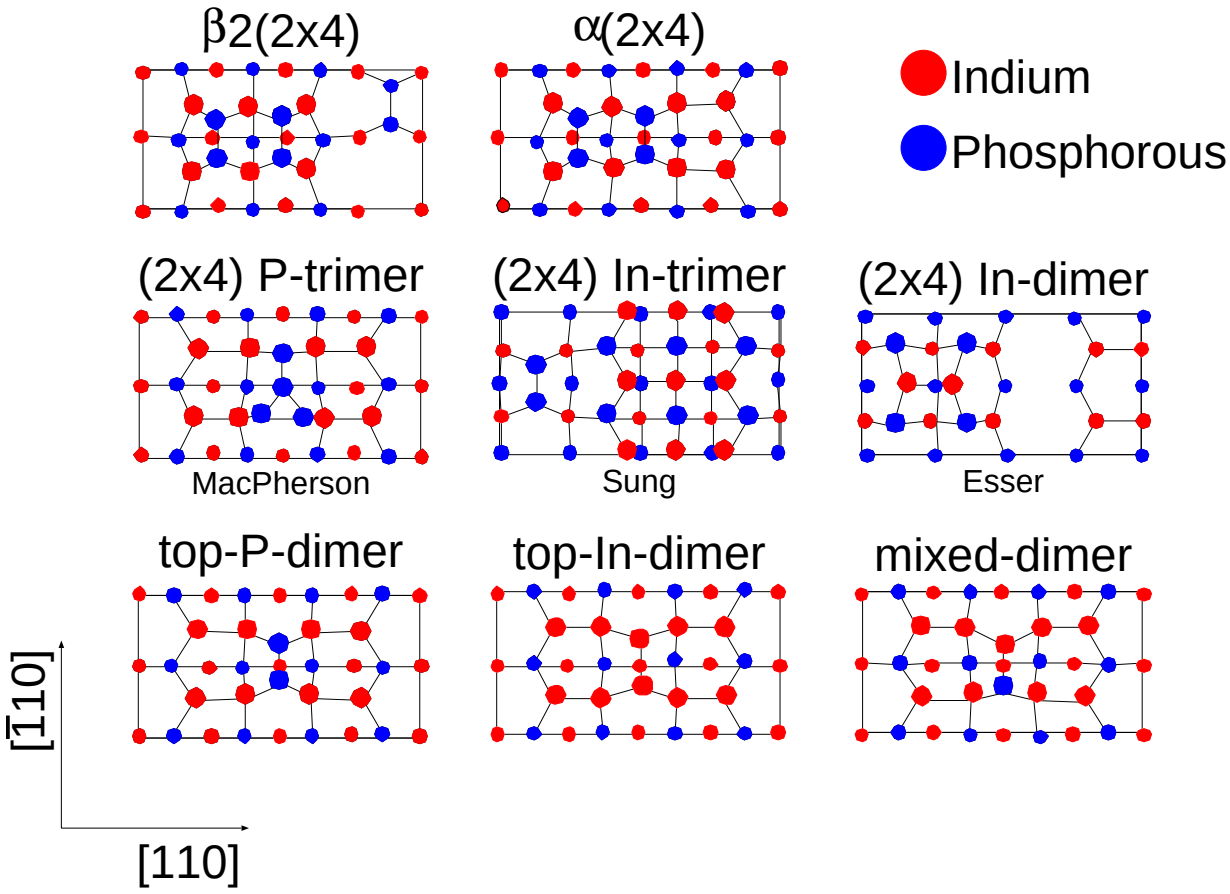

Figure IV.7: The 8 surface structures for which we calculate the optical response.

If we first compare the experimental results in figure IV.9 we can see that the curve given in figure IV.9a) corresponds quite well to the results for higher surface temperatures in figure IV.9b). Both have a strong negative peak slightly below 2 eV and a pronounced positive peak around 2.75 eV. Finally two minima at about 3 eV and 4 eV and two maxima at about 3.6 eV and 4.6 eV. All calculated spectra except the $\beta 2$ in figure IV.8 exhibit a negative peak between 1.5 and 2.0 eV but only the mixed-dimer structure also has a notable positive peak at about 2.5 eV. Also the high energy part of the mixed-dimer compares quite well. Although not very pronounced two minima and two maxima can be found between 3 and 5 eV. Besides the total energy calculation in [214, 213] mentioned earlier, this is another strong indication that the InP(001)-(2×4) surface has a mixed-dimer reconstruction under In-rich conditions as shown in figure IV.7.

For temperatures between $470°C$ and $490°C$ the strong negative peak slightly below 2 eV nearly vanishes as shown in figure IV.9b) indicating a change in the structure of the surface. Only one calculated spectrum displays no structure below 2 eV, namely the $\beta 2$ spectrum. In figure IV.9b) only two maxima at about 2.75 eV and 4 eV are present and

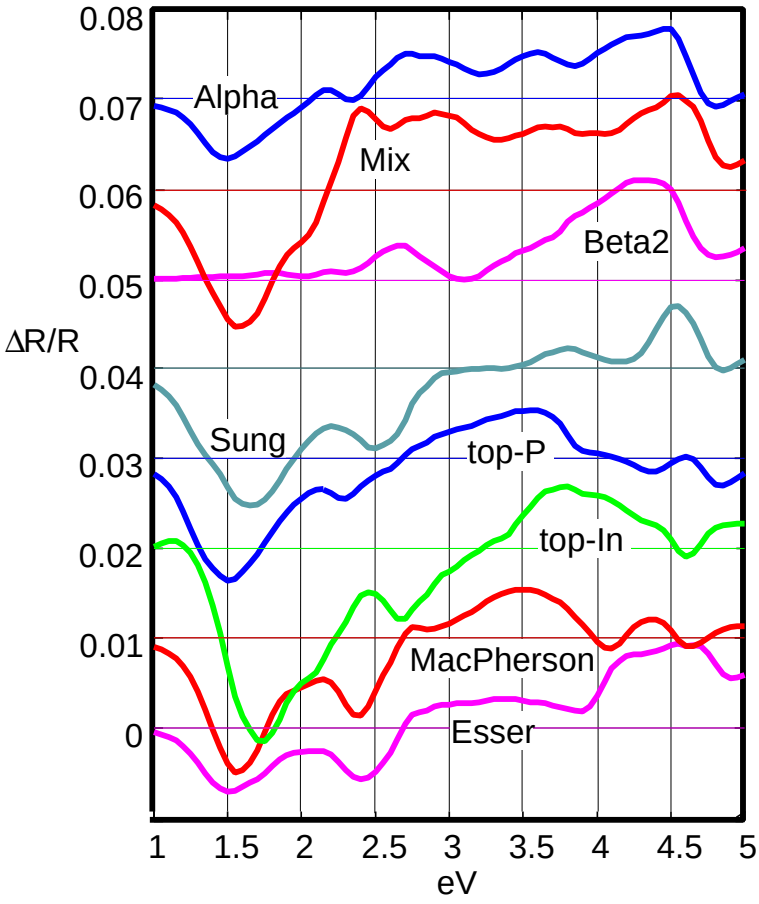

Figure IV.8: Calculated RA-spectra of the surface structures shown in figure IV.7.

the calculated spectrum in IV.8 shows two maxima at nearly the same positions, too. This leave us with the result that under P-rich conditions the surface reconstruction of InP(001)-(2×4) is a $\beta 2$ reconstruction as shown in figure IV.7.

IV.4 Decomposition of the RA-spectra

After the identification of the mixed-dimer reconstructions as the surface structure of InP(001)-(2×4) for In-rich conditions the question arises which transitions are responsible for the specific features of the spectrum. To answer this question we will decompose the spectrum as described above by defining a surface area and looking for transitions between states mainly localised in this area, mainly localised outside of this area in the bulk and transition between the surface and bulk states.

In figure IV.10 the results for three different surface areas are shown. First only the mixed top-dimer belongs to the surface area and it is clearly visible that no transitions inside of the dimer are involved in the spectrum. Only bulk-bulk transition are present. This changes drastically when the next layer filled with In atoms is included in the

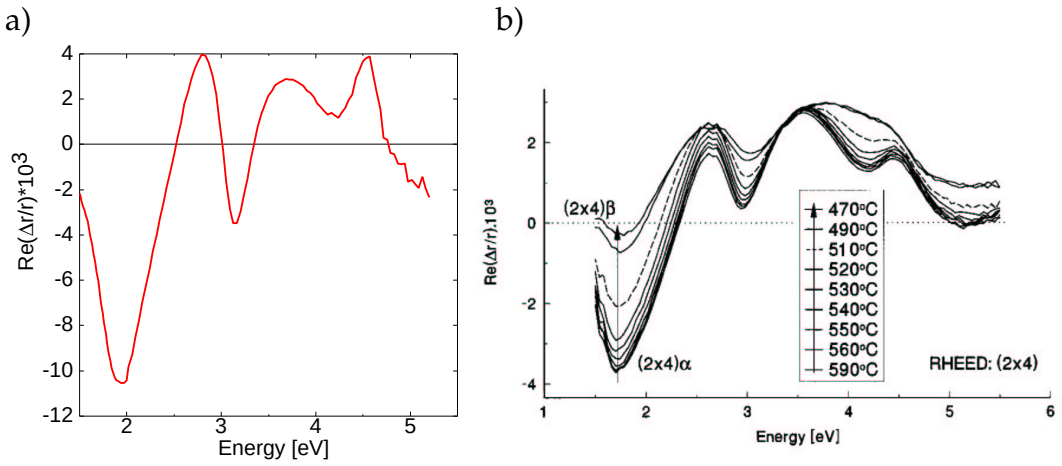

Figure IV.9: Result of RA measurements of the InP(001) surface. a) was taken at room temperature and published in [216], b) has been published in [203]. The results are shown here with kind permissions of the authors.

surface layer. Now in all possible transition pairs a spectrum with a distinct structure is visible. The bulk-bulk spectrum already looks quite similar to the bulk's dielectric function shown in figure IV.6 as it should be without any surface contributions. The strong negative peak below 2 eV is now given by negative structures in the surf-surf and in the surf-bulk transitions. If the next layer, now filled with P atoms is also included into the surface area the picture does not change much giving more or less the same spectra as the previous figure.

An inspection of the atomic structure of the mixed-dimer reconstruction can now give some hints about how the transitions may look in real space. Five three-fold bounded In atoms, i.e. In atoms with an empty dangling bond, can be found on the surface. While four of them are at the corners of the In rectangle in the second layer the fifth is the In atom in the top dimer. With the result of figure IV.10 that the main contribution to the negative peak below 2 eV originates from the second layer we can assume that transitions from the filled bond states of the In-In bonds in the second layer and of the bonds to the top dimer to the dangling bonds at the corner atoms are the reason for this strong negative peak. This also explains why this peak can be found in nearly all surface reconstructions we have taken in account. All except of the $\beta 2$ have three-fold bound In atoms and In-In bonds while the $\beta 2$ has also the three-fold bound In atoms, but no In-In bonds.

IV.5 Summary

In this chapter we have tried to find out how the surface of InP(001)-(2×4) is constructed. We have compared the calculated RA spectra of different proposed (2×4)

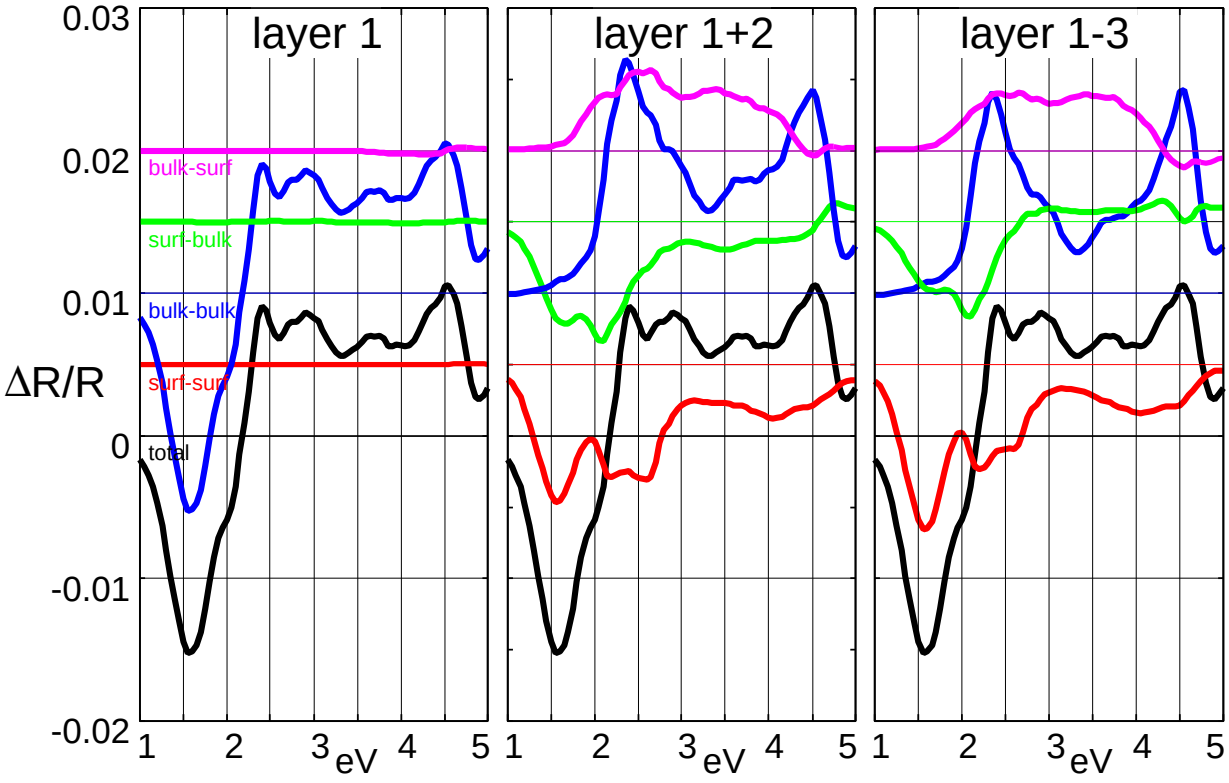

Figure IV.10: Decomposition of the mixed-dimer spectrum. In the plot for layer 1 only the top dimer is labelled as surface while in the plot of layer 1+2 the underlying In-layer is included and in the layer 1-3 plot the following P-layer is included, too.

reconstructions with experimental data. As a result it was found the for In-rich conditions a mixed-dimer reconstruction (see figure IV.7) can be found while in P-rich conditions a $\beta 2$ reconstruction is preferred. The main difference of the RA spectra of the two surfaces is a strong negative peak slightly below 2 eV which can be explained by transitions mainly from filled In-In bond to empty dangling bonds of three-fold bound In atoms. All these results are in good agreement with recent DFT based studies of the same surface [217, 202] and also with soft x-ray photoelectron spectroscopy (SXPS) [213] and STM [218] studies.

It is also noteworthy that tight-binding based calculations as presented here still lead to results which can compete with more advanced DFT based ab-initio calculations [202, 184, 219]. This gives the opportunity to use tight-binding based calculations which are from the numerical point of view connected with much less effort, e.g., they are suited for the study of many different proposed surfaces in a reasonable amount of time as has been shown here. But one has to be careful. The calculation of the RA spectrum of a GaP(001) surface with a tight-binding scheme gave only poor results [220] while the corresponding DFT based calculations [221] produced good results. The reason for this is probably that the $sp^3s^\star$-model is too simple to reveal good results for the GaP(001)

surface and that d-orbitals have to be included in the calculations. But still the tight-binding calculations in future might be useful, for example for other reconstructions than the (2×4) like the ones recently reported in [222, 223].

V: Summary and outlook

We have made the acquaintance of three different pattern forming semiconductor systems. The first one, the charge transport through a semiconductor interface was a non-equilibrium system driven away from thermodynamic equilibrium by a constant current of electrons. A system at thermodynamic equilibrium, the structure of a semiconductor surface, was discussed in the third example. In the second example we have studied the initial phase of the formation of self-organised quantum dots, a system which is first driven away from the equilibrium by a constant flux of atoms to a semiconductor surface and then can relax to the equilibrium after the flux of atoms is stopped.

Besides the three different types of systems we have also presented three different theoretical methods to describe them. Although there are quantum-mechanical descriptions for all three systems, only in the third example Schrödinger's equation was solved. In the other two examples we used more phenomenological approaches. In the quantum dots examples we treat atoms as small balls which can jump to nearest neighbour positions in a periodic lattice defined by the substrate. Although this may sound like playing with children's bricks this very simple model is supported by ab-initio calculations which solve the underlying quantum-mechanical problem (see e.g. [38]). For the first example we even moved a level higher and did not consider single electrons, but used an electron density. Although this approach is on top of a hierarchy of semiconductor transport models [48] there is always a clear path between the different levels of the hierarchy so that the higher levels can be justified by the lower ones.

There are two main reasons why we use simplified models. The first one is a practical one. It is at the time being not possible to simulate the evolution of quantum dots or the formation of current filaments at a semiconductor interface in an adequate amount of time. The reason can be found in the different time and length scales which are involved in the problems. The period of the oscillations of current filaments are orders of magnitudes larger than the fastest electronic processes in a quantum-mechanical description. Also domain sizes which are necessary for useful studies of quantum dot formation are at least three orders of magnitude larger compared to what is currently possible with ab-initio calculations. The second reason is a physical one. A microscopic theory in general implies material dependences which can be seen in chapter IV. Every

material has its own specific surface structure for a given surface direction and therefore specific properties. Layered semiconductor diodes on the other hand can show some common behaviour not only independent of the material (GaAs/AlGaAs, Si) but also independent of type of diode (HHED, p-i-n). Also the self-organised formation of quantum dots can be observed in different material systems (InAs/GaAs, Ge/Si) and in different experimental setup (molecular beam, gas-phase, liquid phase epitaxy). For these two examples it is desirable to use a theoretical model which concentrates on the common features and does not hide them by material specific effects. It would also be desirable for the comparison of the pattern forming processes in the systems to find a way to describe both systems with the same theoretical concept, e.g., with partial differential equations but we will discuss in the following why this is not easy to achieve.

We have seen in chapter II that the Turing or filamentary instabilities leads to three different types of two-dimensional stationary current density distributions in two slightly different models for charge transport in a layered semiconductor diode. The models are given by the partial differential equations (II.1) and (II.2). Unfortunately in only one of the models (II.1) complex oscillating structures could be found so far. A recently started analytic study by Just et al. will try to answer the question if there are regimes in parameter space, which have not been studied here, where also in the model (II.2) similar oscillating structures can be found. Although it is quite hard to observe the spatial and spatio-temporal structures directly we have shown that every type of structure found can be identified by studying the current-voltage diagrams of the specific device.

In chapter III kinetic Monte Carlo simulations where strain effect have been included were used to simulate the initial phase of the growth of self organised quantum dots. We have found two different growth modes which can produce the fundaments of quantum dots with a sharp size distribution and, under some conditions, in a nicely ordered array. In the first mode all the quantum dots grow simultaneously out of a large number of small seeds, in the second mode the quantum dots grow one after the other where a new quantum dot nucleates when all other quantum dots on the surface have reached a critical size. By varying external parameters like growth-rate, temperature or coverage a transition to a cluster forming growth mode could be found for both growth modes. It was also found that in both growth modes a sharp distribution of island sizes can be found even for low coverages where spatial ordering was only observed for higher coverages where the island density and the mean island size are large enough to allow an interaction of the strain field around an island with neighbouring islands. For the parameters used for simulations here it turned out that for a coverage of about 35 % an optimum in size and spatial ordering can be found. If only the size distribution is of importance a lower coverage will yield better results, i.e. a sharper size distribution. We would like to mention here again that we count the coverage without the wetting layer which we assume passive.

If we compare the temporal evolution of the different patterns of chapter II and III we find that the spot-like Turing pattern found in the system given by (II.2) and the growth

mode where all islands grow simultaneously show some common behaviour. In both cases a number of objects grow out of small seeds at the same time equally distributed over the domain but not necessarily ordered perfectly in space. Here we can see why it is difficult to find a description for the initial phase of quantum dot growth based on partial differential equations. The Turing instability, where a pattern with a specific wave-length will grow out of a small random perturbation, compares quite well to the simultaneous growth mode, but will in general never show a behaviour similar to the one-after-the-other growth mode. In terms of nonlinear dynamics this growth mode would more likely correspond to localised structures or solitons [6, 224]. Consequently a dynamical system based on partial differential equations which should describe the initial phase of the growth of quantum dots must have more than one spatial instability. Another problem arises from the fact that the variables in partial differential equations are in general densities, i.e.ãverages over many individual processes. But in sub-monolayer epitaxy, i.e.w̃ith coverages below one monolayer, the individual processes are still important. If we move to the order of ten and more monolayers partial differential equations like the Kardar-Parisi-Zhang equation [225] are very helpful to study the surface roughness. Models based on partial differential equation were also used to describe the temporal evolution of steps of monolayer height in the step-flow growth mode [226] but also with a deposition of ten monolayers or more. But nevertheless we hope that the results of the Monte Carlo simulations presented here will help to develop a suitable system of partial differential equation which may open a way to feed the knowledge about pattern formation in dynamical systems into the fabrication of quantum dots.

There are a couple of ways to extend the simple Monte Carlo scheme presented here. Most important is a more physical modelling of the strain field which was already started [122, 123]. This would also open the possibility to include the wetting layer into the simulation. There are also first studies of anisotropic diffusion [133]. All these extensions would help to make the simulations more realistic and also more material specific. And here the microscopic study of the surface structure of InP in chapter IV becomes important. Since for detailed simulations of a specific material system it is essential to know what are the important processes during the growth at the surface. To find them one has to know, e.g., the atomic structure of the clean surface which is different for every material system. We have seen in chapter IV that the InP-(001) surface has a number of different properties than, e.g., the corresponding surface of GaAs. Especially the mixed dimer reconstruction which has no parallel in GaAs. We also think that the comparison of measured and calculated optical spectra are an important tool to understand the growth of quantum dots. Although it is nowadays possible to compare images from a scanning tunnelling microscope nicely with first principle calculations [227] it is still easier and faster to take optical spectra in-situ, i.e. during the growth of the quantum dots [170, 172].

Bibliography

[1] A. M. Zhabotinskii,
Periodic processes of the oxidation of malonic acid in solution,
Biofizika **9**, 306 (1964).

[2] Hydrodynamic instabilities and the Transition to Turbulence,
Topics Appl. Phys., Vol. 45,
edited by H. Swinney and J. P. Gollub (Springer, Berlin, Heidelberg, New York, 1981).

[3] R. Lefever and G. Nicolis,
Chemical instabilities and sustained oscillations,
J. Theor. Biol. **30**, 267 (1971).

[4] R. J. Field and R. M. Noyes,
Oscillations in chemical systems, Part 4. Limit cycle behavior in a model of a real chemical reaction,
J. Chem. Phys **60**, 1877 (1974).

[5] J. Swift and P. C. Hohenberg,
Hydrodynamic fluctuations at the convective instability,
Phys. Rev. A **15**, 319 (1977).

[6] M. C. Cross and P. C. Hohenberg,
Pattern formation outside of equilibrium,
Rev. Mod. Phys. **65**, 851 (1993).

[7] J. Guckenheimer and P. Holmes,
Nonlinear Oscillations, Dynamical Systems, and Bifurcations of Vector Fields,
Applied mathematical sciences 42
(Springer-Verlag, Berlin, 1983).

[8] H. Haken,
Synergetics, An Introduction,
3 ed. (Springer, Berlin, 1983).

[9] J. D. Murray,
Mathematical Biology, Vol. 19 of
Biomathematics Texts,
1st ed. (Springer, Berlin Heidelberg, 1993).

[10] J. D. Murray,
How the leopard gets its spots,
Sci. Amer. **258**, 80 (1988).

[11] S. Kaufmann,
At Home in the Universe
(Oxford University Press, New York, 1995).

[12] A. M. Pertsov, F. M. Davidenko, R. Salomonsz, W. T. Baxter, and J. Jalife,
Spiral waves of exitation underlie reentrant activity in isolated cardiac muscle,
Criculation Research **72**, 631 (1993).

[13] C. F. Starmer and J. Starobin,
Spiral tip movement: The role of repolarizing currents in polymorphic cardiac arrhythmias,
Int. J. Bifur. Chaos **6**, 1909 (1996).

[14] L. Glass and M. C. Mackey,
From Clocks to Chaos
(Princeton University Press, Princton, New Jersey, 1988).

[15] E. Schöll,
Nonequilibrium Phase Transitions in Semiconductors
(Springer, Berlin, 1987).

[16] Theory of Transport Properties of Semiconductor Nanostructures, Vol. 4 of
Electronic Materials Series,
edited by E. Schöll (Chapman and Hall, London, 1998).

[17] M. P. Shaw, V. V. Mitin, E. Schöll, and H. L. Grubin,
The Physics of Instabilities in Solid State Electron Devices
(Plenum Press, New York, 1992).

[18] F.-J. Niedernostheide, B. S. Kerner, and H.-G. Purwins,
Spontaneous appearance of rocking localized current filaments in a nonequilibrium distributive system,
Phys. Rev. B **46**, 7559 (1992).

[19] F.-J. Niedernostheide, M. Ardes, M. Or-Guil, and H.-G. Purwins,
Spatio-Temporal behavior of localized current filaments in p-n-p-n diodes: Numerical calculations and comparison with experimental results,
Phys. Rev. B **49**, 7370 (1994).

[20] F.-J. Niedernostheide, M. Kreimer, B. Kukuk, H.-J. Schulze, and H.-G. Purwins,
Travelling current density filaments in multilayered silicon devices,
Phys. Lett. A **191**, 285 (1994).

[21] A. V. Gorbatyuk and P. B. Rodin,
Mechanism for spatially periodic stratification of current in a thyristor,
Soviet Technical Physics Letters **16**, 519 (1990).

[22] A. V. Gorbatyuk and P. B. Rodin,
Turing's instability and space periodic current filamentation in a thyristor,
Journal of communication technology and electronics **40**, 49 (1995).

[23] Kinetics of Ordering and Growth at Surfaces,
edited by M. G. Lagally (Plenum Press, New York, 1990).

[24] Surface Disordering: Growth, Roughening and Phase Transitions,
edited by R. Jullien, J. Kertész, P. Maekin, and D. E. Wolf (Nova Science, New York, 1992).

[25] A.-L. Barabási and H. E. Stanley,
Fractal concepts in surface growth
(Cambridge University Press, Cambridge, U.K., 1995).

[26] I. N. Stranski and L. Krastanow,
Sitzungsberichte der Akademie der Wissenschaften in Wien,
Akad. Wiss. Lit. Mainz Math.-Natur. Kl. IIb **146**, 797 (1939).

[27] N. N. Ledentsov, M. Grundmann, N. Kirstaedter, O. Schmidt, R. Heitz, J. Böhrer, D. Bimberg, V. Ustinov, V. Shchukin, A. Egorov, A. Zhukov, S. Zaitsev, Z. A. P.S. Kop'ev, S. Ruvimov, P. Werner, U. Gösele, and J. Heydenreich,
Ordered Arrays of Quantum Dots: Formation, Electronic Spectra, Relaxing Phenomena, Lasing,
Sol. State El. **40**, 785 (1996).

[28] Q. Xie, A. Madhukar, P. Chen, and N. P. Kobayashi,
Vertically self-Organized InAs Quantum Box Islands on GaAs(100),
Phys. Rev. Lett. **75**, 2542 (1995).

[29] M. Dilger, R. J. Haug, K. Eberl, and K. von Klitzing,
Single-electron transitors with a self-assembled quantum dot,
Semicond. Sci. Technol. **11**, 1493 (1996).

[30] L. Zhuang, L. Guo, and S. Y. Chou,
Silicon single-electron quantum-dot transistor switch operating at room temperature,
Appl. Phys. Lett. **72**, 1205 (1998).

[31] H. Schmid and H.-W. Fink,
Carbon Nanotubes are Coherent Electron Sources,
Appl. Phys. Lett. **70**, 2679 (1997).

[32] P. Carloni and W. Andreoni,
Self-Assembled Peptide Nanotubes from First Principles,
Phys. Rev. Lett. **79**, 761 (1997).

[33] D. Bimberg, M. Grundmann, and N. Ledentsov,
Quantum Dot Heterostructures
(John Wiley & Sons Ltd., New York, 1999).

[34] R. Kunert, Selbstorganisiertes Wachstum von Quantenpunkten in verschiedenen Materialsystemen,, Studienarbeit, TU Berlin, 1999.

[35] R. Schuster, H. Röder, K. Bromann, H. Brune, and K. Kern,
Stress relief via island formation of an isotropically strained bimetallic surface layer: The mesoscopic morphology of the Ag/Pt(111) surface alloy,
Phys. Rev. B **54**, 13476 (1996).

[36] G. Schmid, M. Bäumle, and N. Beyer,
Geordnete zweidimensionale Monolagen von Au_{55}-Clustern,
Angewandte Chemie **112**, 187 (2000).

[37] A. Kley and M. Scheffler,
Diffusivity of Ga and Al adatoms on GaAs(001),
in Proc. 23rd Int. Conf. Phys. Semicond., Berlin 1996, edited by M. Scheffler and R. Zimmermann (World Scientific, Singapore, 1996), pp. 1031–1034.

[38] A. Kley, P. Ruggerone, and M. Scheffler,
Novel diffusion mechanism on the GaAs(001) surface: the role of adatom-dimer interaction,
Phys. Rev. Lett. **79**, 5278 (1997).

[39] M. Gaa, R. E. Kunz, E. Schöll, W. Eberle, J. Hirschinger, and W. Prettl,
Spatial structure of impact-ionization induced current filaments in n-GaAs films,
Semicond. Sci. Technol. **11**, 1646 (1996).

[40] A. Wacker,
Nichtlineare Dynamik bei senkrechtem Ladungstransport in einer Halbleiter–Heterostruktur,
Ph.D. thesis, Technische Universität Berlin, 1993.

[41] A. Wacker and E. Schöll,
Spiking in an Activator-Inhibitor Model for Elements with S-shaped Negative Differential Conductivity,
Z. Phys. B **93**, 431 (1994).

[42] S. Bose, A. Wacker, and E. Schöll,
Bifurcation scenarios of spatio-temporal spiking in semiconductor devices,
Phys. Lett. A **195**, 144 (1994).

[43] A. Wacker, S. Bose, and E. Schöll,
Transient spatio-temporal chaos in a reaction-diffusion model,
Europhys. Lett. **31**, 257 (1995).

[44] M. Meixner, A. De Wit, S. Bose, and E. Schöll,
Generic spatio-temporal dynamics near Turing-Hopf codimension-two bifurcations,
Phys. Rev. E **55**, 6690 (1997).

[45] M. Meixner, S. Bose, and E. Schöll,
Analysis of chaotic patterns near a codimension-2 Turing-Hopf point in a reaction-diffusion model,
Physica D **109**, 128 (1997).

[46] M. Meixner, S. Zoldi, S. Bose, and E. Schöll,
Karhunen-Loève local characterization of spatio-temporal chaos in a reaction-diffusion system,
Phys. Rev. E **61**, 1382 (2000).

[47] A. F. Volkov and S. M. Kogan,
Nonuniform current distribution in semiconductors with negative differential conductivity,
Sov. Phys. JETP **25**, 1095 (1967).

[48] E. Schöll,
Nonlinear spatio-temporal dynamics and chaos in semiconductors
(Cambridge University Press, Cambridge, 2000), in print.

[49] P. Gray and S. K. Scott,
Chemical Oscillations and Instabilities
(Clarendon Press, Oxford, 1990).

[50] A. Wacker and E. Schöll,
Spatio-temporal dynamics of vertical charge transport in a semiconductor heterostructure,
Semicond. Sci. Technol. **7**, 1456 (1992).

[51] R. Stasch, R. Hey, M. Asche, A. Wacker, and E. Schöll,
Temperature persistent bistability and threshold switching in a single barrier heterostructure hot-electron diode,
J. Appl. Phys. **80**, 3376 (1996).

[52] F.-J. Niedernostheide, H. Schulze, S. Bose, A. Wacker, and E. Schöll,
Spiking in a semiconductor device: Experiments and comparison with a model,
Phys. Rev. E **54**, 1253 (1996).

[53] C. Radehaus, K. Kardell, H. Baumann, D. Jäger, and H.-G. Purwins,
Pattern Formation in S-Shaped Negative Differential Conductivity Material,
Z. Phys. B **65**, 515 (1987).

[54] R. Symanczyk, S. Gaelings, and D. Jäger,
Observation of spatio-temporal structures due to current filaments in Si pin diodes,
Phys. Lett. A **160**, 397 (1991).

[55] C. Kittel,
Introduction to Solid State Physics,
7 ed. (Wiley, New York, 1995).

[56] H. Ibach and H. Lüth,
Einführung in die Grundlagen der Festkörperphysik
(Springer, Heidelberg, 1988).

[57] F. Bechstedt and R. Enderlein,
Semiconductor Surfaces and interfaces. Their Atomic and Electronic Structure
(Akademie-Verlag, Berlin, 1988).

[58] K. Hess, T. K. Higman, M. A. Emanuel, and J. J. Coleman,
New ultrafast switching mechanism in semiconductor heterostructures,
J. Appl. Phys. **60**, 3775 (1986).

[59] A. S. Mikhailov,
Foundations of Synergetics Vol. I,
2 ed. (Springer, Berlin, 1994).

[60] Self-Organization in Activator-Inhibitor-Systems: Semiconductors, Gas Discharge, and Chemical Active Media,
edited by H. Engel, F.-J. Niedernostheide, H. G. Purwins, and E. Schöll (Wissenschaft und Technik Verlag, Berlin, 1996).

[61] F.-J. Niedernostheide, M. Or-Guil, M. Kleinkes, and H.-G. Purwins,
Dynamical behavior of spots in a nonequilibrium distributive active medium,
Phys. Rev. E **55**, 4107 (1997).

[62] A. M. Turing,
The chemical basis of morphogenesis,
Phil. Trans. Roy. Soc. **237**, 37 (1952).

[63] S. Bose,
Filamentdynamik in einem generischen Halbleitertransportmodell,
Master's thesis, TU Berlin, 1994.

[64] M. Löschau,
Musterbildung in Reaktions-Diffusions-Systemen vom Aktivator-Inhibitor-Typ in zwei Di-

mensionen,
Diplomarbeit, TU Berlin, 1998.

[65] J. D. Crawford,
Introduction to bifurcation theory,
Rev. Mod. Phys. **63**, 991 (1991).

[66] M. Meixner, P. Rodin, and E. Schöll,
Accelerated, decelerated and oscillating fronts in a globally coupled bistable semiconductor system,
Phys. Rev. E **58**, 2796 (1998).

[67] W. H. Vandevender and K. H. Haskell,
The SLATEC mathematical subroutine library,
SIGNUM Newsletter **17**, 16 (1982).

[68] J. L. Kaplan and J. A. Yorke,
Chaotic behavior of multidimensional difference equations,
in Functional differential equations and approximations of fixed points. Lecture notes in mathematics Vol. 730, edited by H. O. Peitgen and H. O. Walter (Springer, Berlin, 1979).

[69] G. Franceschini, S. Bose, and E. Schöll,
Control of chaotic spatiotemporal spiking by time-delay autosynchronisation,
Phys. Rev. E **60**, 5426 (1999).

[70] K. J. Luo, H. T. Grahn, and K. H. Ploog,
Relocation time of the domain boundary in weakly coupled GaAs/AlAs superlattices,
Phys. Rev. B **57**, 6838 (1998).

[71] F. Prengel, A. Wacker, and E. Schöll,
Simple model for multistability and domain formation in semiconductor superlattices,
Phys. Rev. B **50**, 1705 (1994).

[72] S. Bose, P. Rodin, and E. Schöll,
Competing spatial and temporal instabilities in a globally coupled bistable semiconductor system near a codimension-two bifurcation,
Phys. Rev. E **62**, 1778 (2000).

[73] A. Alekseev, S. Bose, P. Rodin, and E. Schöll,
Stability of current filaments in a bistable semiconductor system with global coupling,
Phys. Rev. E **57**, 2640 (1998).

[74] F.-J. Niedernostheide, M. Or-Guil, and M. Kleinkes,
Investigation on Two-Dimensional Patterns in a Multilayered Semiconductor Device,
in Self-Organisation in Activator-Inhibitor-Systems: Semiconductors, Gas-Discharge and Chemical Active Media, edited by H. Engel, F.-J. Niedernostheide, H.-G. Purwins, and E. Schöll (Wissenschaft und Technik Verlag, Berlin, 1996), p. 16.

[75] E. Schöll and D. Drasdo,
Nonlinear dynamics of breathing current filaments in n-GaAs and p-Ge,
Z. Phys. B **81**, 183 (1990).

[76] L. Schimansky-Geier, C. Zülicke, and E. Schöll,
Growth of domains under global constraints,
Physica A **188**, 436 (1992).

[77] T. Tél,
Transient Chaos,
in Directions in Chaos, edited by H. Bai-lin (World Scientific, Singapore, 1990), Vol. 3, p. 149 and 211.

[78] G. Benettin, L. Galgani, A. Giorgilli, and J. Strelcyn,
Lyapunov Characteristic Exponents for Smooth Dynamical Systems; A Method for Computing them all,
Meccanica **15**, 9&21 (1980).

[79] I. Shimada and T. Nagashima,
A Numerical Approach to Ergodic Problem of Dissipative Dynamical Systems,
Prog. Theor. Phys **61**, 1605 (1979).

[80] S. Zoldi and H. Greenside,
Karhunen-Loève Decomposition of Extensive Chaos,
Phys. Rev. Lett. **78**, 1687 (1997).

[81] L. Sirovich,
Chaotic dynamic of coherent structures,
Physica D **37**, 126 (1989).

[82] M. Caponeri and S. Ciliberto,
Thermodynamic aspects of the transition to spatiotemporal chaos,
Physica D **58**, 365 (1992).

[83] A. De Wit, D. Lima, G. Dewel, and P. Borckmans,
Spatiotemporal Dynamics near a Codimension-Two Point,
Phys. Rev. E **54**, 261 (1996).

[84] A. Maier,
Kodimension-2-Turing-Hopf-Bifurkation im Oregonatormodell,
Studienarbeit, TU Berlin, 1997.

[85] Y. Kuramoto,
Chemical Oscillations, Waves and Turbulence
(Springer-Verlag, Berlin, 1988).

[86] M. Bär, N. Gottschalk, M. Hildebrand, and M. Eiswirth,
Sprials and chemical trubulence in an exitable surface reaction,
Physica A **213**, 173 (1995).

[87] M. Bär and M. Or-Guil,
Alternative Scenarios of Spiral Breakup in a Reaction-Diffusion Model with Excitable on Oscillatory Dynamics,
Phys. Rev. Lett. **82**, 1160 (1999).

[88] H. Xi, J. D. Gunton, and J. Viñals,
Spiral Defect Chaos in a Model of Rayleigh-Bénard Convection,
Phys. Rev. Lett. **71**, 2030 (1993).

[89] D. Battogtokh, A. Preusser, and A. Mikhailov,
Controlling turbulence in the complex Ginzburg-Landau equation II. Two-dimensional systems,
Physica D **106**, 327 (1997).

[90] S. Zoldi, J. Liu, K. M. S. Bajaj, H. S. Greenside, and G. Ahlers,
Extensive scaling and nonuniformity of the Karhunen-Loeve decomposition for the spiral-defect chaos state,
Phys. Rev. E **58**, R6903 (1998).

[91] E. Ammelt, Y. Astrov, and H.-G. Purwins,
Pattern Formation in Gas Discharge Systems,
in Self-Organisation in Activator-Inhibitor-Systems: Semiconductors, Gas-Discharge and Chemical Active Media, edited by H. Engel, F.-J. Niedernostheide, H.-G. Purwins, and E. S. höll (Wissenschaft und Technik Verlag, Berlin, 1996), p. 22.

[92] I. Brauer, C. Punset, H.-G. Purwins, and J. P. Boeuf,
Simulations of self-organized filaments in a dielectric barrier glow discharge plasma,
J. Appl. Phys. **85**, 7569 (1999).

[93] E. Ammelt, Y. A. Astrov, and H.-G. Purwins,
Stripe Turing structures in a two-dimensional gas discharge system,
Phys. Rev. E **55**, 6731 (1997).

[94] E. Ammelt, Y. A. Astrov, and H.-G. Purwins,
Hexagon structures in a two-dimensional dc-driven gas discharge system,
Phys. Rev. E **58**, 7109 (1998).

[95] A. Rovinsky and M. Menzinger,
Interaction of Turing and Hopf bifurcations in chemical systems,
Phys. Rev. A **46**, 6315 (1992).

[96] H. Haken,
Advanced Synergetics,
2 ed. (Springer, Berlin, 1987).

[97] M. F. Hilali, S. Métens, P. Borckmans, and G. Dewel,
Pattern selection in the generalized Swift-Hohenberg model,
Phys. Rev. E **51**, 2046 (1995).

[98] M. F. Hilali, S. Métens, G. Dewel, and P. Borckmans,
Pattern Selection and diffusive Instability,
in Instabilities and Nonequilibrium Structures V, edited by E. Tirapegui and W. Zeller (Kluwer Academic Publisher, Dordrecht, 1996), p. 99.

[99] G. Dewel, P. Borckmans, A. De Wit, B. Rudovics, J.-J. Perraud, E. Dulos, J. Boissonade, and P. D. Kepper,
Pattern selection and localized structures in reaction-diffusion systems,
Physica A **213**, 181 (1995).

[100] B. S. Kerner and V. V. Osipov,
Autosolitons
(Kluwer Academic Publishers, Dordrecht, 1994).

[101] A. V. Gorbatyuk and P. B. Rodin,
Effect of distributed-gate control on current filamentation in thyristors,
Sol. State El. **35**, 1359 (1992).

[102] A. V. Gorbatyuk and P. B. Rodin,
Current filamentation in a bistable semiconductor system with two global constraints,
Z. Phys. B **104**, 45 (1997).

[103] F. C. Frank and J. H. van der Merwe,
One-dimensional dislocations. I. Static theory,
Proc. R. Soc. London, Ser. A **198**, 205 (1949).

[104] M. Volmer and A. Weber,
Z. Phys. Chem. **119**, 277 (1926).

[105] V. Shchukin and D. Bimberg,
Spontaneous ordering of nanostructures on crystal surfaces,
Rev. Mod. Phys. **71**, 1125 (1999).

[106] Y. Arakawa and H. Sakaki,
Multidimensional quantum well laser and temperature dependence of its threshold current,
Appl. Phys. Lett. **40**, 939 (1982).

[107] Y. Arakawa and A. Yariv,
Quantum Well Lasers – Gain, Spectra, Dynamics,
IEEE J. Quantum. Electron. **QE22**, 1887 (1986).

[108] D. Bimberg, N. N. Ledentsov, M. Grundmann, N. Kirstaedter, O. G. Schmidt, M. H. Mao, V. Ustinov, A. Egorov, A. Zhukov, P. Kop'ev, Z. Alferov, S. Ruvimov, U. Gösele, and J. Heydenreich,
InAs-GaAs quantum pyramid lasers: in situ growth, radiative lifetimes and polarization properties,
Jpn. J. Appl. Phys. **35**, 1311 (1996).

[109] V. A. Shchukin, N. N. Ledentsov, M. Grundmann, and D. Bimberg,
in Optical Spectroscopy of Low Dimensional Semiconductors,
NATO ASI,
edited by G. Abstreiter (Kluwer, Amsterdam, 1997).

[110] N. Moll, A. Kley, E. Pehlke, and M. Scheffler,
GaAs equilibrium crystal shape from first-principles,
Phys. Rev. B **54**, 8844 (1996).

[111] E. Pehlke, N. Moll, and M. Scheffler,
The equilibrium shape of quantum dots,
in Proc. VI Italian-Swiss Workshop on Advances in Computational Materials Science, edited by V. Fiorentini and F. Meloni (Editrice Compositori, Bologna, 1997), pp. 43–52.

[112] H. Eisele, O. Flebbe, T. Kalka, C. Preinesberger, F. Heinrichsdorff, and A. Krost,
Cross-sectional scanning-tunneling microscopy of stacked InAs quantum dots,
Appl. Phys. Lett. **75**, 106 (1999).

[113] C. Priester and M. Lannoo,
Origin of Self-Assembled Quantum Dots in Highly Mismatched Heteroepitaxy,
Phys. Rev. Lett. **75**, 93 (1995).

[114] S. Clarke, M. R. Wilby, and D. D. Vvedensky,
Theory of homoepitaxy on Si(001),
Surf. Sci. **255**, 91 (1991).

[115] C. Heyn, T. Franke, R. Anton, and M. Harsdorff,
Correlation between island-formation kinetics, surface roughening, and RHEED oscilla-

tion damping during GaAs homoepitaxy,
Phys. Rev. B **56**, 13483 (1997).

[116] F. Große,
Simulation des Wachstums und Berechnung optischer Eigenschaften von Halbleiterquantenstrukturen,
Ph.D. thesis, Humboldt-Universität zu Berlin, 1996.

[117] A. S. Saada,
Elasticity - Theory and applications
(Pergamon, New York, 1974).

[118] V. A. Shchukin, N. N. Ledentsov, P. S. Kop'ev, and D. Bimberg,
Spontaneous ordering of arrays of coherent strained islands,
Phys. Rev. Lett. **75**, 2968 (1995).

[119] I. Daruka and A.-L. Barabási,
Dislocation-Free Island Formation in Heteroepitaxial Growth: A Study at Equilibrium,
Phys. Rev. Lett. **79**, 3708 (1997).

[120] I. Daruka and A.-L. Barabási,
Equilibrium phase diagrams for dislocation free self-assembled quantum dots,
Appl. Phys. Lett. **72**, 2102 (1998).

[121] J. R. Downes, D. A. Faux, and E. P. O'Reilly,
A simple method for calculating strain distributions in quantum dot structures,
J. Appl. Phys. **81**, 6700 (1997).

[122] M. Meixner,
Ph.D. thesis, TU Berlin, in preparation.

[123] M. Meixner, R. Kunert, S. Bose, E. Schöll, V. A. Shchukin, D. Bimberg, E. Penev, and P. Kratzer,
Monte Carlo simulation of the self-organized growth of quantum dots with anisotropic surface diffusion,
in Proc. 25th International Conference on the Physics of Semiconductors (ICPS-25), Osaka 2000, edited by N. Miura (Springer, Berlin, 2001).

[124] M. Grundmann, O. Stier, and D. Bimberg,
InAs/GaAs quantum pyramids: strain distribution, optical phonons and electronic structure,
Phys. Rev. B **52**, 11969 (1995).

[125] M. J. P. Musgrave and J. A. Pople,
A general valence force field for diamond,
Proc. R. Soc. A **268**, 474 (1962).

[126] P. N. Keating,
Effect of invariance requirements on the elastic strain energy of crystals with application to the diamond structure,
Phys. Rev. **145**, 637 (1966).

[127] O. Stier, M. Grundmann, and D. Bimberg,
Electronic and optical properties of strained quantum dots modeled by 8-band k·p theory,
Phys. Rev. B **59**, 5688 (1999).

[128] M. Schroeder and D. E. Wolf,
Diffusion on strained surfaces,
Surf. Sci. **375**, 129 (1997).

[129] M. Schroeder,
Diffusion und Wachstum auf Kristalloberflächen,
Ph.D. thesis, Gerhard-Mercator-Universität Gesamthochschule Duisburg, 1997.

[130] C. Ratsch,
Effects of Strain on Heteroepitaxial Growth Dynamics,
Ph.D. thesis, Georgia Institute of Technology, 1994.

[131] C. Ratsch, P. Šmilauer, A. Zangwill, and D. Vvedensky,
Mechanism for coherent island formation during heteroepitaxy,
J. Phys. I **6**, 575 (1996).

[132] J. Frenkel and T. Kontorova,
On the theory of Plastic Demotation and Twinning,
J. Phys. (Moscow) **8**, 1 (1939).

[133] R. Kunert,
Monte-Carlo-Simulation der Wachstumskinetik von Quantenpunkten im Nukleationsstadium,
Master's thesis, TU Berlin, 2000.

[134] R. L. Schwoebel and E. J. Shipsey,
Step motion on crystal surfaces,
J. Appl. Phys. **37**, 3682 (1966).

[135] R. L. Schwoebel,
Step motion on crystal surfaces II,
J. Appl. Phys. **40**, 614 (1968).

[136] Schöll and S. Bose,
Kinetic Monte Carlo Simulation of the Nucleation Stage of the Self-organized Growth of Quantum Dots,
Sol. State El. **42**, 1587 (1998).

[137] W. H. Press, B. P. Flannery, S. A. Teukolsky, and W. T. Vettering,
Numerical Recipes in C (2nd ed.)
(Cambridge University Press, Cambridge, 1992).

[138] M. Schmidbauer, T. Wiebach, H. Raid, M. Hanke, R. Köhler, and H. Wawra,
Ordering of self-assembled $Si_{1-x}Ge_x$ islands studied by grazing incidence small-angle x-ray scattering and atomic force microscopy,
Phys. Rev. B **58**, 10523 (1998).

[139] E. Steimetz, F. Schienle, J.-T. Zettler, and W. Richter,
Stranski-Krastanov formation of InAs quantum dots monitored during growth by reflectance anisotropy spectroscopy and spectroscopic ellipsometry,
Journal of Crystal Growth **170**, 208 (1997).

[140] M. Grundmann, N. N. Ledentsov, R. Heitz, L. Eckey, J. Christen, J. Böhrer, D. Bimberg, S. Ruvimov, P. Werner, U. Richter, J. Heydenreich, V. Ustinov, A. Egorov, A. Zhukov, P. S. Kop'ev, and Z. Alferov,

InAs/GaAs quantum dots: Radiative recombination from zero-dimensional states, phys. status solidi (b) **188**, 249 (1995).

[141] G. Abstreiter, P. Schittenhelm, C. Engel, E. Silveria, A. Zrenner, D. Meertens, and W. Jäger, Growth and characterization of self-assembled Ge-rich islands on Si, Semicond. Sci. Technol. **11**, 1521 (1996).

[142] K. H. Schmidt, G. Medeiros-Ribeiro, J. Garcia, and P. M. Petroff, Size quantisation effects in InAs self-assembled quantum dots, Appl. Phys. Lett. **70**, 1727 (1997).

[143] R. Nötzel, Self-organized growth of quantum-dot structures, Semicond. Sci. Technol. **11**, 1365 (1996).

[144] D. Leonard, K. Pond, and P. M. Petroff, Critical layer thickness for self-assembled InAs islands on GaAs, Phys. Rev. B **50**, 11687 (1994).

[145] F. Heinrichsdorff, MOCVD growth and laser applications of In(Ga)As/GaAs Quantum Dots, Ph.D. thesis, TU Berlin, 1998.

[146] V. Shchukin, Spontaneous formation of arrays of strained islands: Thermodynamics versus kinetics, in Proc. Fall Meeting Mat. Res. Soc., Boston, USA (MRS, Warrendale, PA, 1999).

[147] J. von Neumann, Theory of Self-reproducing Automata (University of Illinois, Chicago, YEAR).

[148] S. Wolfram, Universality and complexity in cellular automata, Physica D **10**, 1 (1984).

[149] P. Vogl, G. Zandler, A. Rein, and M. Saraniti, in Theory of Transport Properties of Semiconductor Nanostructures, Vol. 4 of *Electronic Materials Series*, edited by E. Schöll (Chapman and Hall, London, 1998).

[150] T. Fricke and L. Schimansky-Geier, Moving Spots in Three Dimensions, in Self-Organisation in Activator-Inhibitor-Systems: Semiconductors, Gas-Discharge and Chemical Active Media, edited by H. Engel, F.-J. Niedernostheide, H.-G. Purwins, and E. Schöll (Wissenschaft und Technik Verlag, Berlin, 1996), p. 184.

[151] J. A. Freund and L. Simansky-Geier, Diffusion in discret ratchets, Phys. Rev. E **60**, 1304 (1999).

[152] S. V. Ghaisas and A. Madhukar, Computer simulations of the role of surface reconstruction, stoichiometry and strain in molecular beam epitaxical growth and defect formation, in Proceedings of the SPIE Symposium on Growth of Compound Semiconductor Structures II, edited by A. Madhukar (SPIE Press, Bellingham, WA, 1988), Vol. 944, p. 16.

[153] S. V. Ghaisas and A. Madhukar,
Kinetic aspects of growth front surface morphology and defect formation during molecular-beam epitaxy growth of strained thin films,
J. Vac. Sci. Technol. B **7**, 264 (1989).

[154] S. V. Ghaisas and A. Madhukar,
Influence of compressive and tensile strain on growth mode during epitaxical growth: A computer simulation study,
Appl. Phys. Lett. **53**, 1599 (1988).

[155] A. Madhukar,
A unified atomistic and kinetic framework growth front morphology evolution and defect initiation in strained epitaxy,
Journal of Crystal Growth **163**, 149 (1996).

[156] C. Ratsch, P. Ruggerone, and M. Scheffler,
in Surface Diffusion: Atomistic and Collective Processes,
NATO ASI Series B: Physics Vol. 360,
edited by M. Tringides (Plenum Press, New York, 1997), p. 83.

[157] A.-L. Barabási,
Self-assembled island formation in heteroepitaxial growth,
Appl. Phys. Lett. **70**, 2565 (1997).

[158] B. G. Orr, D. Kessler, C. W. Snyder, and L. Sander,
A Model for Strain-Induced Roughening and Coherent Island Growth,
Europhys. Lett. **19**, 33 (1992).

[159] C. Lee and A.-L. Barabási,
Spatial ordering of islands grown on patterned surfaces,
Appl. Phys. Lett. **73**, 2652 (1998).

[160] B.-G. Liu, J. Wu, E. G. Wang, and Z. Zhang,
Two-dimensional pattern formation in surfactant-mediated epitaxial growth,
Phys. Rev. Lett. **83**, 1195 (1999).

[161] I.-S. Hwang, T.-C. Chang, and T. T. Tsong,
Exchange-Barrier Effects on Nucleation and Growth of Surfactant-Mediated Epitaxy,
Phys. Rev. Lett. **80**, 4229 (1998).

[162] T.-C. Zhang, I.-S. Hwang, and T. T. Tsong,
Direct Observation of Reaction-Limited Aggregation on Semiconductor Surfaces,
Phys. Rev. Lett. **83**, 1191 (1999).

[163] B.-G. Liu and E. Schöll,
Strained growth in surfactant mediated heteroepitaxy,
Vacuum (2000).

[164] V. P. Evtikhiev, V. E. Tokranov, A. K. Kryganovskii, A. M. Boiko, R. A. Suris, and A. N. Titkov,
Characteristics of the InAs quantum dots MBE grown of the vincinal GaAs(001) surface misoriented to the [010] direction,
Journal of Crystal Growth **201/202**, 1154 (1999).

[165] V. A. Shchukin, A. J. Borovkov, N. N. Ledentsov, and D. Bimberg,
Tuning and breakdown of faceting under externally applied stress,
Phys. Rev. B **51**, 10104 (1995).

[166] L. G. Wang, P. Kratzer, M. Scheffler, and N. Moll,
Formation and stability of self-assembled coherent islands in highly mismatched heteroepitaxy,
Phys. Rev. Lett. **82**, 4042 (1999).

[167] H. T. Dobbs, D. D. Vedensky, A. Zangwill, J. Johansson, N. Carlsson, and W. Seifert,
Mean-Field Theory of Quantum Dot Formation,
Phys. Rev. Lett. **79**, 897 (1997).

[168] A. Y. Kaminskii and R. A. Suris,
2D nuclei evolution during epitaxial growth,
Sol. Stat. Comm. **89**, 697 (1994).

[169] A. Y. Kaminskii and R. A. Suris,
Smoothing of crystal surfaces during growth interruption,
Appl. Surf. Sci. **104/105**, 312 (1996).

[170] J.-T. Zettler,
Characterization of epitaxial semiconductor growth by reflectance anisotropy spectroscopy and ellipsometry,
Prog. Crystal Growth and Charact. **35**, 27 (1997).

[171] W. Richter,
Optical in-situ control during MOVPE and MBE growth,
Philos. Trans. R. Soc (London) A **344**, 453 (1993).

[172] E. Steimetz, J.-T. Zettler, F. Schienle, T. Trepk, T. Wethkamp, W. Richter, and I. Sieber,
In-situ Monitoring of InAs-on-GaAs Quantum Dot Formation in MOVPE by Reflectance-Anisotropy-Spectroscopy and Ellipsometry,
Appl. Surf. Science **107**, 203 (1996).

[173] R. Del Sole,
in Photonic Probes of Surfaces,
edited by P. Halevi (Elsevier Science B.V., Amsterdam, 1995), Chap. 4, pp. 133–174.

[174] F. Bechstedt, O. Pulci, and W. G. Schmidt,
Theoretical Aspects of the Optical Response of Semiconductor Surfaces,
phys. status solidi (a) **175**, 5 (1999).

[175] R. Del Sole,
Present status and capabilities for the theoretical calculation of surface optical properties,
Thin Solid Films **313-314**, 527 (1998).

[176] J. E. Sipe, A. I. Shkrebtii, and O. Pulci,
Issues Concerning the Calculation of hte Optical Response of Semiconductors,
phys. status solidi (a) **170**, 431 (1998).

[177] R. Del Sole,
Present Status of the Theory of Surface Optical Properties,
phys. status solidi (a) **170**, 183 (1998).

[178] W. A. Harrison,
Electronic Structure and the Properties of Solids
(Freeman, San Francisco, 1980).

[179] W. Jackson,
Classical Electrodynamics
(John Wiley, New York, 1975).

[180] J. D. E. McIntyre and D. E. Aspnes,
Surf. Sci. **24**, 417 (1971).

[181] M. Nakayama,
Theory of Electromagnetic Respone of Solid Surface,
J. Phys. Soc. Jpn. **39**, 265 (1975).

[182] A. Bagchi, R. G. Barrera, and A. K. Rajagopal,
Perturbative approach to the calculation of the electric field near a metal surface,
Phys. Rev. B **20**, 4824 (1979).

[183] R. Del Sole,
Microscopic theory of optical properties of crystal surfaces,
Sol. Stat. Comm. **37**, 537 (1981).

[184] F. Manghi, R. Del Sole, A. Selloni, and E. Molinari,
Anisotropy of surface optical properties from first-principles calculations,
Phys. Rev. B **41**, 9935 (1990).

[185] F. Wooten,
Optical properties of solids
(Academic Press, New York and London, 1972).

[186] J. C. Slater and G. F. Koster,
Simplified LCAO Method for the Periodic Potential Problem,
Phys. Rev. **94**, 1498 (1954).

[187] P.-O. Löwdin,
On the Non-Orthogonality problem Connected with the Use of Atomic Wave Functions in the Theory of Molecules and Crystals,
J. Chem. Phys. **18**, 365 (1950).

[188] P. Vogl, H. P. Hjalmarson, and J. D. Dow,
A Semi-Empirical Thight-Binding Theory of the Electronic Structure of Semiconductors,
J. Phys. Chem. Solids **44**, 365 (1983).

[189] E. Anderson, Z. Bai, C. Bischof, S. Blackford, J. Demmel, J. Dongarra, J. Du Croz, A. Greenbaum, D. Hammarling, A. McKenney, and D. Sorensen,
LAPACK Users' Guide,
3rd ed. (Society for Industrial and Applied Mathematics, Philadelphia, PA, 1999).

[190] C. L. Lawson, R. J. Hanson, D. Kincaid, and F. T. Krogh,
Basic Linear Algebra Subprograms for FORTRAN usage,
ACM Trans. Math. Soft. **5**, 308 (1979).

[191] A. Selloni, P. Marsella, and R. Del Sole,
Microscopic calculation of the surface contribution to optical reflectivity: Application to Si,
Phys. Rev. B **33**, 8885 (1986).

[192] C. M. Noguez, A. I. Shkrebtii, and R. Del Sole,
Microscopic theory of electron transitions at Si(111)-7×7: Optical properties and energy-loss spectra,
Surf. Sci. **331-333**, 1349 (1995).

[193] A. I. Shkrebtii and R. Del Sole,
Microscopic calculations on structure and optical properties of Ge(001)c(4x2),
Surface Science **331-333**, 1288 (1995).

[194] P. Chiaradia, A. I. Shkrebtii, C. Goletti, J. Wang, and R. Del Sole,
Polarization-dependent surface transitions at Sb/GaAs(110),
Sol. Stat. Comm. **85**, 497 (1993).

[195] P. Chiaradia, A. I. Shkrebtii, C. Goletti, J. Wang, and R. Del Sole,
Corrigendum,
Sol. Stat. Comm. **89**, 87 (1994).

[196] N. Esser, R. Hunger, J. Rumberg, W. Richter, R. Del Sole, and A. I. Shkrebtii,
Reflectance anisotropy spectroscopy od ordered Sb overlayers on GaAs(110) and InP(110),
Surf. Sci. **307-309**, 1045 (1994).

[197] J. R. Power, P. Weightman, S. Bose, A. I. Shkrebtii, and R. Del Sole,
Sensitivity of Relectancs Anisotropy Spectroscopy to the Orientation of Ge Dimers on Vincinal Si(001),
Phys. Rev. Lett. **80**, 3133 (1998).

[198] J. R. Power, P. Weightman, S. Bose, A. I. Shkrebtii, and R. D. Sole,
Initial stages of Ge growth on vicinal Si(001) studied by reflectance anisotropy spectroscopy,
Surf. Sci. **433**, 373 (1999).

[199] Y.-C. Chang and D. E. Aspnes,
Theory of dielectric-function anisotropies of (001) GaAs (2 x 1) surfaces,
Phys. Rev. B **41**, 12002 (1990).

[200] S.-F. Ren and Y.-C. Chang,
Electronic and optical properties of GaAs(001) (2 x 4) and (4 x 2) surfaces,
Phys. Rev. B **44**, 13573 (1991).

[201] T. H. Shen and C. M. J. Matthai,
Calculation of the optical properties of As molecules on Si Substrates,
Surf. Sci. **287-288**, 672 (1993).

[202] W. G. Schmidt, E. L. Briggs, J. Bernholc, and F. Bechstedt,
Structural fingerprints in the reflectance anisotropy spectra of InP(001)(2x4) surfaces,
Phys. Rev. B **59**, 2234 (1999).

[203] K. B. Ozanyan, P. J. Parbrook, M. Hopkinson, C. R. Whitehouse, Z. Sobiesierski, and D. I. Westwood,
In-situ monitoring of the surface reconstructions on InP(001), prepared by molecular beam epitaxy,
J. Appl. Phys. **82**, 474 (1997).

[204] Landolt-Börnstein: Numerical Data and Functional Relationships in Science and Technology,

edited by K. Hellwege and O. Madelung (Springer, Berlin, Heidelberg, New York, 1982), Vol. III/17a.

[205] R. M. A. Azzam and N. M. Bashara,
Ellipsometry and Polazied Light
(North Holland, Amsterdam, 1977).

[206] M. Zorn, T. Trepk, J.-T. Zettler, C. Meyne, K. Knorr, T. Wethkamp, M. Klein, W. Richter, B. Junno, and M. Miller,
Temperature dependence of the InP(001) bulk and surface dielectric function,
Appl. Phys. A **65**, 333 (1997).

[207] S. Albrecht, L. Reining, R. Del Sole, and G. Onida,
Ab Initio Calculation of Excitonic Effects in the Optical Spectra of Semiconductors,
Phys. Rev. Lett. **80**, 4510 (1998).

[208] M. Rohlfind and S. G. Louie,
Electron-Hole Excitations in Semiconductors and Insulators,
Phys. Rev. Lett. **81**, 2312 (1998).

[209] M. M. Sung, C. Kim, H. Bu, D. S. Karpuzov, and J. W. Rabalais,
Composition and stucture of the InP(100)-(1x1) and -(4x2) surfaces,
Surf. Sci. **322**, 116 (1995).

[210] X. Hou, G. Dong, X. Ding, and X. Wang,
A missing-row dimer model of Inp(100)(4x2) reconstruction as proposed by LEED, UPS and HREELS studies,
J. Phys. C: Solid State Phys. **20**, L121 (1987).

[211] C. D. MacPherson, R. A. Wolkow, C. E. J. Mitchell, and A. B. McLean,
Scanning Tunneling Microscopy Study of InP(100)-(2x4): An Exception to the Dimer Model,
Phys. Rev. Lett. **77**, 691 (1996).

[212] D. Pahlke, J. Kinsky, C. Schultz, M. Pristovsek, M. Zorn, N. Esser, and W. Richter,
Sturcture of InP(001) surfaces prepared by decapping and by ion bombardment and annealing,
Phys. Rev. B **56**, R1661 (1997).

[213] W. G. Schmidt, F. Bechstedt, N. Esser, M. Pristovsek, C. Schultz, and W. Richter,
Atomic structure of InP(001)-(2x4): A dimer reconstruction,
Phys. Rev. B **57**, 14596 (1998).

[214] W. G. Schmidt and F. Bechstedt,
Geometry and electronic structure of InP(001)(2x4) reconstructions,
Surf. Sci. **409**, 474 (1998).

[215] W. G. Schmidt,
Zum Einfluß dünner Metall- und Passivierungsschichten auf Oberflächen von III-V-Verbindungshalbleitern,
Ph.D. thesis, Friedrich-Schiller-Universität Jena, 1997.

[216] N. Esser, W. G. Schmidt, J. Bernholc, A. M. Frisch, P. Vogt, M. Zorn, M. Pristovsek, W. Richter, F. Bechstedt, T. Hannappel, and S. Visbeck,
GaP(001) and Inp(001): Reflectance anisotropy and surface geometry,
J. Vac. Sci. Technol. B **17**, 1691 (1999).

[217] W. G. Schmidt, N. Esser, A. M. Frisch, P. Vogt, J. Bernholc, F. Bechstedt, M. Zorn, T. Hannappel, S. Visbeck, F. Willig, and W. Richter,
Understanding reflectance anisotropy: Surface-state signature and bulk-related features in the optical spectrum of InP(001)(2x4),
Phys. Rev. B **61**, R16335 (2000).

[218] N. Esser, U. Resch-Esser, M. Pristovsek, and W. Richter,
Scanning-tunneling-microscopy study of InP(001) surfaces prepared by UHV decapping of metal-organic vapour-phase-epitaxy-grown samples,
Phys. Rev. B **53**, R13257 (1996).

[219] G. Onida, R. Del Sole, M. Palummo, O. Pulci, and L. Reining,
Ab-initio Calculation of the Optical Properties of Surfaces,
phys. status solidi (a) **170**, 365 (1998).

[220] M. Zorn, B. Junno, T. Trepk, S. Bose, L. Samuelson, J.-T. Zettler, and W. Richter,
Optical response of reconstructed GaP(001) surfaces,
Phys. Rev. B **60**, 11557 (1999).

[221] A. M. Frisch, W. G. Schmidt, J. Bernholc, M. Pristovsek, N. Esser, and W. Richter,
(2×4) GaP(001) surface: Atomic structrure and optical anisotropy,
Phys. Rev. B **60**, 2488 (1999).

[222] P. Vogt, T. Hannappel, S. Visbeck, K. Knorr, N. Esser, and W. Richter,
Atomic surface structure of the phosphorous-terminated InP(001) grown by MOVPE,
Phys. Rev. B **60**, R5117 (1999).

[223] P. Vogt, A. M. Frisch, T. Hannappel, S. Visbeck, F. Willig, C. Jung, N. Esser, W. Braun, and W. Richter,
Atomic Surface Structure of MOVPE-Grown InP(001),
phys. status solidi (b) **215**, 737 (1999).

[224] K. Staliunas and V. J. Sánchez-Morcillo,
Spatial-localized structures in degenerate optical parametric oscillators,
Phys. Rev. A **57**, 1454 (1998).

[225] M. Kardar, G. Parisi, and Y.-C. Zhang,
Dynamic scaling of growing interfaces,
Phys. Rev. Lett. **56**, 889 (1986).

[226] H. Emmerich, C. Misbah, K. Kassner, and T. Ihle,
Vicinal surfaces: growth structures close to the instability threshold and far beyond,
J. Phys.: Condens. Matter **11**, 9985 (1999).

[227] V. LaBella, H. Yang, D. Bullock, P. Thibado, P. Kratzer, and M. Scheffler,
Atomic structure of the GaAs(001)-(2x4) surface resolved using scanning tunneling microscopy and first-principles theory,
Phys. Rev. Lett. **83**, 2989 (1999).

Curriculum vitae

- **Persönliche Daten**

  Geboren am 4.2.69

  in Berlin

  Famlienstand verheiratet seit dem 22.9.2000 mit Miriam Bose, geb. Löschau

  Staatsangehörigkeit deutsch

- **Schulbildung**

  August 1975 - Juli 1979 Herman-Schulz-Grundschule in Berlin-Reinickendorf

  August 1979 - Juli 1981 Grundschule der Evangelischen Schule in Berlin-Frohnau

  August 1981 - Juni 1988 Gymnasium der Evangelischen Schule in Berlin-Frohnau

- **Studium**

  Oktober 1988 - August 1994 Physikstudium an der Technischen Universität Berlin

  Oktober 1992 - September 1994 Beschäftigt als studentische Hilfskraft mit Lehraufgaben am Institut für Theoretische Physik der TU-Berlin

  November 1992 - März 1993 Studienarbeit mit dem Thema ″Vertikaler Transport durch eine Halbleiter Doppelschichtstruktur″

  April 1993 - Mai 1994: Diplomarbeit mit dem Thema ″Dynamik von Stromfilamenten in einem generischen Modell für den Stromtransport in Halbleitern″

  August 1994 Diplom für Physik mit dem Gesamturteil ″sehr gut″

  Oktober 1994 - August 1998 Beschäftigt als wissenschaftlicher Mitarbeiter bei Herrn Prof. Dr. Schöll im DFG Schwerpunktprogramm ″Strukturbildung in dissipativen kontinuierlichen Systemen″

  Mai-Juni 1997 Gastaufenthalt an der Universität Roma II ″Tor Vergata″ in der Arbeitsgruppe von Prof. R. DelSole

  seit September 1998 Beschäftigt als wissenschaftlicher Mitarbeiter im Teilprojekt B1 (″Nichtlineare raumzeitliche Strukturen in bistabilen Halbleitern″) des Sonderforschungsbereichs 555 ″Komplexe Nichtlineare Prozesse″